Proper motion studies in the nuclear stellar disk

UNIVERSIDAD
DE GRANADA

Álvaro Martínez Arranz

Supervisor: Dr. Rainer Schödel

Radioastronomy and Galactic structure department
Instituto de Astrofísica de Andalucía
Universidad de Granada
Programa de Doctorado en Física y Ciencias del Espacio

This dissertation is submitted for the degree of
Doctor of Philosophy

IAA June 2024

to R.
for the help, the trust and the beers.

Abstract

At a distance of just 8.25 kpc from Earth lies the center of the Milky Way (GRAVITY Collaboration et al., 2020), a region of exceptional importance for astrophysical research. It harbors the closest supermassive black hole, some of the most massive star clusters, and the largest concentration of gas and dust in the Galaxy. This region is remarkable for astrophysical research because of its unique and extreme conditions. The stellar density here is between 10^4 and 10^7 times higher than the average stellar density in the Galactic disk (Schödel et al., 2007, 2018). Despite making up only 0.1% of the total surface area of the Galaxy, its central region emits about 10% of its total Lyman continuum flux (Launhardt et al., 2002; Nishiyama et al., 2008). The densities of star-forming molecular clouds in the Galactic Center (GC) are, on average, about two orders of magnitude higher than in the Galactic disk.

Within the GC we can find the Central Molecular Zone (CMZ), a dense concentration of gas and dust. The CMZ, with an approximate mass of 10^7 $M_\odot$ (Dahmen et al., 1998), constitutes 5% of the entire Galaxy's gas reservoir, concentrated in a zone smaller than 1% of its volume. Thus, it is not very surprising that this area stands out for its high star formation rate. However, this rate is still about one order of magnitude lower than expected considering the elevated densities of the gas present in the CMZ (Kennicutt et al., 2005; Longmore et al., 2013a; Henshaw et al., 2023).

The Nuclear Stellar Disk (NSD) is flat rotating structure about 150 pc across and 45 pc in scale height (Knapen, 2005; Nishiyama et al., 2013; Sormani et al., 2022) that lies inside the CMZ. Recent studies have shown that the star formation rate in this area reached levels of about [0.2 - 0.8] $M_\odot$/yr in the last 30 Myr (Matsunaga et al., 2011; Nogueras-Lara et al., 2020), meaning that $\sim 10^6$ $M_\odot$ of young stars were formed in this period. In spite of this large number, surprisingly, there are only only three clusters documented today in the GC: the central stellar cluster, in the central parsec of the GC and with a mass of $\sim 10^4 M_\odot$ (Bartko et al., 2010; Lu et al., 2013); and the Arches and the Quintuplet clusters, 2 and 4.5 Myr old respectively, with masses of a few 10^4 $M_\odot$ each (Figer et al., 1999b; Espinoza et al., 2009; Harfst et al., 2010; Morales et al., 2013) located at the NSD. The combined masses of

the three clusters account for less than for 10% of the expected mass of newly born stars in the NSD. One of the question we will try to address is, Where are the missing clusters?

Discovering other young clusters would allow us to investigate the cluster formation mechanisms in the GC. The initial mass function (IMF) of the Arches and Quintuplet clusters appears to differ from that of clusters found in the Galactic disk, showing an overrepresentation of massive stars (Hosek et al., 2019; Gallego-Calvente et al., 2022). Analyzing the mass distribution of other young clusters in the NSD would help us determine the origin of this discrepancy.

The NSD and CMZ are likely related. Bars in spiral galaxies channel vast amounts of gas and dust into the central region, leading to the formation of CMZs (Elmegreen et al., 2009; Shimizu et al., 2019; Sormani and Barnes, 2019). The high pressure and densities of this material eventually trigger bursts of star formation, resulting in the creation of nuclear disks (Sormani et al., 2018a; Seo et al., 2019).

The CMZ is sprinkled with dense molecular clouds, some as massive as 10^5 $M_\odot$, which surprisingly show hardly any star formation, challenging empirically established relations between molecular gas properties and star formation rate (Mills et al., 2015; Longmore et al., 2017). This strange behavior could be related to the position of these clouds in the gravitational potential field of the GC (Kruijssen et al., 2015). However this is not clear. These dense molecular clouds are not homogeneously distributed along the NSD, but show a dominant presence at positive longitudes (Longmore et al., 2013b). Although numerical simulations have shown that these asymmetries can appear naturally in the central molecular zones of spiral galaxies (Kim et al., 2012; Sormani et al., 2018b), the physical mechanisms driving the asymmetric distribution of these clouds remain unclear. Therefore, knowing the position of these clouds is of crucial importance to find out their distribution in the CMZ and to understand the processes by which this asymmetric distribution occurs.

The objective of this dissertation is to demonstrate the relevance of studying proper motions in the center of our Galaxy, illustrating how the analysis of these data allows us to constrain distances and identify new structures, such as young clusters. We will present new analysis techniques developed for data obtained in this challenging environment and the novel results obtained by applying them. We also present the first results of a new catalog of proper motions in the GC. When completed, this catalog, based on the study of GALACTICNUCLEUS survey (GNS, Nogueras-Lara et al., 2019a) will cover a significant part of the NSD with an unprecedented accuracy in ground-based observations.

The main results of this thesis have been published in three refereed articles in Astronomy & Astrophysics (Martínez-Arranz et al., 2022, 2024a,b). In the following we summaries the most relevant findings.

We have constrained the distance to the dense molecular cloud G0.253+0.016, a.k.a. the Brick (Martínez-Arranz et al., 2022). The line-of-sight distance of this feature has been under discussion recently, with a publication placing it $\sim$ 2 kpc closer to Earth than previously assumed (Zoccali et al., 2021), and therefore outside of the GC. The location along the line-of-sight of the Brick, whether in or out of the GC and the CMZ, is crucial to understand the peculiar characteristics of this supermassive ($\sim 10^5$ $M_\odot$) cloud, that hardly shows any traces of star formation (Mills et al., 2015; Longmore et al., 2017). We constructed a proper motion dataset for the stars in front of and around the Brick using images from the High Acuity Wide field K-band Imager (HAWK-I) mounted on the Very Large Telescope (VLT), using specialized observing and image reduction techniques that allowed us to reach a homogeneous angular resolution of 0.2" (Schödel et al., 2013; Nogueras-Lara et al., 2019a). Analysis of this data showed that the Brick is located inside the NSD, and thus the GC. As part of the analysis of the same dataset, we also found evidence of the rotation of the NSD, corroborating previously determined values for this structure (Schonrich et al., 2015; Sormani et al., 2022; Shahzamanian et al., 2022). These results show how proper motion analysis is a valid tool for the estimation of distances and the identification of structures in the complex environment of the GC.

In spite of its high star formation activity in the past 30 Myr, there are only two massive young clusters known in the NSD, the Arches and the Quintuplet. Their combined mass is on the order of a few 10^4 $M_\odot$ (Harfst et al., 2010; Gallego-Calvente et al., 2022), which is only $<$10% of what it should be according to theoretical considerations for the formed mass of young stars in this period (Matsunaga et al., 2011; Barnes et al., 2017; Nogueras-Lara et al., 2020). This discrepancy has come to be known as the 'missing clusters problem'. This observational conundrum can be explained, in part, by the extreme crowding of stars, which makes cluster identification impossible by visual inspection except maybe for the most massive clusters. Moreover, even the most massive young clusters will dissolve beyond recognition in less than $\sim$10 Myr due to the conditions at the GC (Kim et al., 1999; Portegies Zwart et al., 2001; Kruijssen et al., 2014). We tried to find additional young star clusters at the GC by looking in the data for comoving groups of stars which could indicate the presence of clusters or stellar associations. We analyzed the proper motion catalog by Libralato et al. (2021b) in combination with the photometry catalogs of the

GNS (Nogueras-Lara et al., 2018, 2019a, 2021a). We developed an unsupervised machine learning technique based on the Density-Based Spatial Clustering of Applications with Noise (DBSCAN) algorithm (Ester et al., 1996) to scrutinize these catalogs . We found three comoving groups that showed dense spatial packaging and similar velocities, making them solid candidates to be part of a cluster or stellar association (Martínez-Arranz et al., 2024a).

In order to confirm the cluster nature of these comoving groups, it is necessary to perform further analysis of the individual stars that form them. If these comoving groups are indeed a cluster or stellar association (or part of a bigger one), their members have to be younger than the time these structures take to dissolve. We reduced and analyzed spectroscopic data from an area that partially overlaps with one of the comoving groups presented in Martínez-Arranz et al. (2024a). This data was acquired with the K-band Multi Object Spectrograph (KMOS) mounted on the VLT. We combined the spectroscopic information of the stars in the KMOS field with proper motions and photometry catalogs (Nogueras-Lara et al., 2018; Libralato et al., 2021b). We found a group of stars, all of them only a few megayears old, that share velocities and positions (Martínez-Arranz et al., 2024b). The evidence is strong enough to talk of a newly found young stellar cluster or association in the GC. We named this group Candela 1.

We applied this new methodology to just the area covered by the catalog of Libralato et al. (2021b), $\sim$ 160 square arcminutes, which represents just a fraction of the NSD. In this relatively small area we found three solid clusters or stellar association candidates and spectroscopically confirmed one of them. According to the predicted star formation rate in the recent history of the NSD, we expect that more clusters or associations like these can be detected with this method. To follow up this research, we are currently working on a proper motion catalog covering approximately $0.3\,deg^2$ of the GC with a precision of around 0.5 mas/yr. The extensive area covered by this catalog in the NSD will allow us to analyze proper motions in areas of recent star formation (Nogueras-Lara et al., 2022a,b) where young clusters are likely to be present. In addition, its high precision will allow us to identify more members of these clusters. Identifying young clusters in the NSD will allow us to study them in detail and investigate whether the initial mass function in the GC is fundamentally different from that in the Galactic disk, as some studies seem to suggest (Morris, 1993; Bartko et al., 2010; Hußmann et al., 2012; Hosek et al., 2019).

Resumen

A una distancia de sólo 8.25 kpc de la Tierra se encuentra el centro de la Vía Láctea (GRAVITY Collaboration et al., 2020), una región de excepcional importancia para la investigación astrofísica. Alberga el agujero negro supermasivo más cercano, algunos de los cúmulos estelares más masivos y la mayor concentración de gas y polvo de la Galaxia. Sus condiciones únicas y extremas hacen esta región única para la investigación. La densidad estelar aquí es entre 10^4 y 10^7 veces mayor que la densidad estelar media en el disco galáctico (Schödel et al., 2007, 2018). A pesar de constituir solo el 0.1% de la superficie total de la Galaxia, su región central emite alrededor del 10% de su flujo total de Lyman continuo (Launhardt et al., 2002; Nishiyama et al., 2008). Las nubes moleculares progenitoras de estrellas en el Centro Galáctico (CG) tienen densidades, en promedio, aproximadamente dos órdenes de magnitud mayores que en el disco galáctico.

Dentro del CG podemos encontrar la Zona Molecular Central (ZMC), una densa concentración de gas y polvo. La ZMC, con una masa aproximada de 10^7 $M_\odot$ (Dahmen et al., 1998), constituye el 5% de la reserva de gas de toda la Galaxia, concentrada en una zona más pequeña que el 1% de su volumen. Por lo tanto, no es muy sorprendente que esta área se destaque por su alta tasa de formación estelar. Sin embargo, esta tasa es aún aproximadamente un orden de magnitud menor de lo esperado considerando las elevadas densidades del gas presente en la ZMC (Kennicutt et al., 2005; Longmore et al., 2013a; Henshaw et al., 2023).

El Disco Estelar Nuclear (DSN) es una estructura plana y giratoría de unos 150 pc de diámetro y 45 pc de altura de escala (Knapen, 2005; Nishiyama et al., 2013; Sormani et al., 2022) que se encuentra dentro de la ZMC. Estudios recientes han mostrado que la tasa de formación estelar en este área alcanzó niveles de aproximadamente [0.2 - 0.8] M$\odot$/año en los últimos 30 Myr (Matsunaga et al., 2011; Nogueras-Lara et al., 2020), lo que significa que $\sim 10^6$ M$\odot$ de estrellas jóvenes se formaron en este período. A pesar de este gran número, sorprendentemente, hoy en día solo hay tres cúmulos documentados en el CG: el cúmulo estelar central, en el pársec central del CG, con una masa de $\sim 10^4 M_\odot$ (Bartko et al., 2010; Lu et al., 2013); y los cúmulos Arches y Quintuplet, de 2 y 4.5 Myr de edad respectivamente, con masas de unos pocos 10^4 $M_\odot$ cada uno (Figer et al., 1999b; Espinoza et al., 2009; Harfst

et al., 2010; Morales et al., 2013) ubicados en el DSN. Las masas combinadas de los tres cúmulos representan menos del 10% de la masa esperada de estrellas recién nacidas en el DSN. Una de las preguntas que intentaremos abordar es, ¿dónde están los cúmulos que faltan?

Descubrir otros cúmulos jóvenes nos permitiría investigar los mecanismos de formación de estelar en el CG. La función de masa inicial (FMI) de los cúmulos Arches y Quintuplet parece diferir de la de los cúmulos encontrados en el disco galáctico, mostrando una sobrerrepresentación de estrellas masivas (Hosek et al., 2019; Gallego-Calvente et al., 2022). Analizar la distribución de masa de otros cúmulos jóvenes en el DSN nos ayudaría a determinar el origen de esta discrepancia.

Es probable que el DSN y la ZMC estén relacionados. Las barras en las galaxias espirales canalizan grandes cantidades de gas y polvo hacia la región central, lo que lleva a la formación de ZZMMCC (Elmegreen et al., 2009; Shimizu et al., 2019; Sormani and Barnes, 2019). La alta presión y densidades de este material eventualmente desencadenan explosiones de formación estelar, resultando en la creación de discos nucleares (Sormani et al., 2018a; Seo et al., 2019). La ZMC está salpicada de nubes moleculares densas, algunas tan masivas como 10^5 $M_\odot$, que, sorprendentemente, apenas muestran formación estelar, desafiando las relaciones empíricamente establecidas entre las propiedades del gas molecular y la tasa de formación estelar (Mills et al., 2015; Longmore et al., 2017). Este extraño comportamiento podría estar relacionado con la posición de estas nubes en el campo de potencial gravitacional del CG (Kruijssen et al., 2015). Sin embargo, esto no está claro. Estas nubes moleculares densas no están distribuidas homogéneamente a lo largo del DSN, sino que muestran una presencia dominante en las longitudes positivas (Longmore et al., 2013b). Aunque las simulaciones numéricas han mostrado que estas asimetrías pueden aparecer naturalmente en las zonas moleculares centrales de las galaxias espirales (Kim et al., 2012; Sormani et al., 2018b), los mecanismos físicos responsables de la distribución asimétrica de estas nubes siguen sin estar claros. Por lo tanto, conocer la posición de estas nubes es de crucial importancia para descubrir su distribución en la ZMC y entender los procesos por los cuales ocurre esta distribución asimétrica.

El objetivo de esta disertación es demostrar la relevancia de estudiar los movimientos propios en el centro de nuestra Galaxia, ilustrando cómo el análisis de estos datos nos permite restringir distancias e identificar nuevas estructuras, como cúmulos jóvenes. Presentaremos nuevas técnicas de análisis desarrolladas para los datos obtenidos en este desafiante entorno y los resultados novedosos obtenidos al aplicarlas. También presentamos los primeros resultados de un nuevo catálogo de movimientos propios en el CG. Cuando se complete, este

catálogo, basado en el análisis del estudio GALACTICNUCLEUS (GNS, Nogueras-Lara et al., 2019a), cubrirá una parte significativa del DSN con una precisión sin precedentes en observaciones desde el suelo.

Los resultados principales de esta tesis se han publicado en tres artículos con revisión por pares en la revísta Astronomy & Astrophysics (Martínez-Arranz et al., 2022, 2024a,b). A continuación, resumimos los hallazgos más relevantes.

Hemos restringido la distancia a la nube molecular densa G0.253+0.016, también conocida como el Ladrillo (Martínez-Arranz et al., 2022). La distancia en la línea de visión de esta nube ha sido objeto de discusión recientemente, con una publicación que la sitúa ~ 2 kpc más cerca de la Tierra de lo que se asumía anteriormente (Zoccali et al., 2021), y por lo tanto fuera del CG. La ubicación a lo largo de la línea de visión del Ladrillo, dentro o fuera del CG y la ZMC, es crucial para entender las características peculiares de esta nube supermasiva ($\sim 10^5$ $M_\odot$), que apenas muestra rastros de formación estelar (Mills et al., 2015; Longmore et al., 2017).

Construimos un conjunto de datos de movimientos propios para las estrellas en frente y alrededor del Ladrillo usando imágenes del High Acuity Wide field K-band Imager (HAWK-I), montado en el Very Large Telescope (VLT), utilizando técnicas especializadas de observación y reducción de imágenes que nos permitieron alcanzar una resolución angular homogénea de 0.2" (Schödel et al., 2013; Nogueras-Lara et al., 2019a). El análisis de estos datos mostró que el Ladrillo se encuentra dentro del DSN, y por lo tanto del CG. Como parte del análisis del mismo conjunto de datos, también encontramos evidencia de la rotación del DSN, corroborando valores previamente determinados para esta estructura (Schonrich et al., 2015; Sormani et al., 2022; Shahzamanian et al., 2022). Estos resultados muestran cómo el análisis de movimientos propios es una herramienta válida para la estimación de distancias y la identificación de estructuras en el complejo entorno del CG.

A pesar de su alta actividad de formación estelar en los últimos 30 Myr, solo hay dos cúmulos jóvenes masivos conocidos en el DSN, Arches y Quintuplet. Su masa combinada es del orden de unos pocos 10^4 $M_\odot$ (Harfst et al., 2010; Gallego-Calvente et al., 2022), que es $<10\%$ de lo que debería ser según las consideraciones teóricas para la masa formada de estrellas jóvenes en este período (Matsunaga et al., 2011; Barnes et al., 2017; Nogueras-Lara et al., 2020; **?**). Esta discrepancia ha llegado a ser conocida como el 'problema de los cúmulos faltantes'.

Este enigma observacional puede explicarse, en parte, por la extrema aglomeración de estrellas, lo que hace que la identificación de cúmulos sea imposible mediante inspección

visual, excepto quizás para los cúmulos más masivos. Además, incluso los cúmulos jóvenes más masivos se disolverán en menos de ∼10 Myr debido a las condiciones en el CG (Kim et al., 1999; Portegies Zwart et al., 2001; Kruijssen et al., 2014).

Intentamos encontrar cúmulos estelares jóvenes adicionales en el CG buscando en los datos grupos de estrellas con movimientos comunes que podrían indicar la presencia de cúmulos o asociaciones estelares. Analizamos el catálogo de movimientos propios por Libralato et al. (2021b) en combinación con los catálogos de fotometría del GNS (Nogueras-Lara et al., 2018, 2019a, 2021a). Desarrollamos una técnica de aprendizaje automático no supervisado basada en el algoritmo de Agrupación Espacial Basada en la Densidad de Aplicaciones con Ruido (DBSCAN, por sus siglas en inglés) (Ester et al., 1996) para examinar estos catálogos. Encontramos tres grupos con movimientos comunes que mostraron un empaquetamiento espacial denso y velocidades similares, lo que los convierte en sólidos candidatos para ser parte de un cúmulo o una asociación estelar (Martínez-Arranz et al., 2024a).

Para confirmar la naturaleza de cúmulo de estos grupos con movimientos comunes, es necesario realizar un análisis adicional de las estrellas individuales que los componen. Si estos grupos con movimientos comunes son realmente un cúmulo o una asociación estelar (o parte de uno más grande), sus miembros deben ser más jóvenes que el tiempo que tardan estas estructuras en disolverse.

Redujimos y analizamos datos espectroscópicos de un área que se superpone parcialmente con uno de los grupos con movimientos comunes presentados en Martínez-Arranz et al. (2024a). Estos datos fueron adquiridos con el Espectrógrafo Multiobjeto en Banda K (K-band Multi Object Spectrograph, KMOS) montado en el VLT. Combinamos la información espectroscópica de las estrellas en el campo de KMOS con catálogos de movimientos propios y fotometría (Libralato et al., 2021b; Nogueras-Lara et al., 2018). Encontramos un grupo de estrellas, todas ellas de sólo unos pocos millones de años, que comparten velocidades y posiciones (Martínez-Arranz et al., 2024b). La evidencia es lo suficientemente fuerte como para hablar de un cúmulo estelar joven recién encontrado en el CG. Nombramos a este grupo Candela 1.

Aplicamos esta nueva metodología sólo al área cubierta por el catálogo de Libralato et al. (2021b), ∼ 160 minutos de arco cuadrados, que representa sólo una fracción del DSN. En esta área relativamente pequeña encontramos tres sólidos candidatos a cúmulos o asociaciones estelares y confirmamos espectroscópicamente uno de ellos. Según la tasa de formación estelar predicha en la historia reciente del DSN, esperamos que se puedan detectar más cúmulos o asociaciones como estos con este método.

Para seguir con esta investigación, estamos trabajando actualmente en un catálogo de movimientos propios que cubre aproximadamente $0.3\,deg^2$ del CG con una precisión de alrededor de 0.5 msa/año. El área extensa cubierta por este catálogo en el DSN nos permitirá analizar movimientos propios en áreas de formación estelar reciente (Nogueras-Lara et al., 2022a,b) donde es probable que haya cúmulos jóvenes. Además, su alta precisión nos permitirá identificar más miembros de estos cúmulos. Identificar cúmulos jóvenes en el DSN nos permitirá estudiarlos en detalle e investigar si la función de masa inicial en el CG es fundamentalmente diferente a la del disco galáctico, como algunos estudios parecen sugerir (Morris, 1993; Bartko et al., 2010; Hußmann et al., 2012; Hosek et al., 2019).

Table of contents

List of figures

List of tables

Chapter 1

Introduction

Our understanding of the structure and dynamics of spiral galaxies has undergone substantial development in recent years thanks to the leap in the quality of observational techniques and instruments, coupled with the substantial increase in computational power. Of particular interest are the cores of these types of galaxies. The central few hundred parsecs of spiral galaxies exhibit remarkable complexity, showcasing a diverse array of structures such as nuclear clusters, nuclear rings, and vast amounts of gas and dust. These structures are closely related to the evolution of the galaxies as a whole and are thus crucial for understanding the processes that drive their formation and development. The extreme conditions in the centers of these galaxies, fundamentally different from those in their disks, serve as the perfect laboratory to investigate phenomena such as supermassive black holes, nuclear star clusters, star formation under extreme conditions, the interrelation of these components and feedback on the galaxies though outflows driven by star formation and black hole accretion. Thus, studying the central regions of spiral galaxies is a very active research field, involving several astrophysical disciplines and actively contributing to the development of new instruments.

There is, however, a fundamental setback in studying the central regions of external galaxies: they are far away. The closest spiral galaxy, Andromeda, is approximately 800 kpc from Earth. Fortunately, we have another galactic core right in our backyard.

The GC, in the constellation of Sagittarius, is located at a distance of only at 8.25 ± 0.01 kpc from Earth (GRAVITY Collaboration et al., 2020), 100 times closer than the center of the Andromeda galaxy. The GC has been found to contain the major building blocks of a typical spiral galaxy nucleus like the supermassive black hole in its center, the nuclear cluster around it or the nuclear disk.

In the course of this dissertation, I will present novel techniques and new results derived from the study of this complex environment. I have centered my research on one massive structure in the GC, the Nuclear Stellar Disk.

1.1 The Nuclear Stellar Disk

The presence of a bar shows a clear increase in frequency as a function of age in disk galaxies and dominates among the most evolved ones at z $\sim$ 0 (Simmons et al., 2014; Melvin et al., 2014; Pérez et al., 2017). The development of a bar in a disk galaxy is a major event because it will lead to significant gas transport towards the central regions and, through subsequent star formation, to the generation and growth of nuclear disks and rings[1].

Due to their non-axisymmetric gravitational potential, bars funnel vast amounts of gas, a few $M_{\odot}$/yr, from the outer regions of galaxies toward their centers (Elmegreen et al., 2009; Ridley et al., 2017; Sormani et al., 2018b; Shimizu et al., 2019; Sormani and Barnes, 2019; Sormani et al., 2023). The accumulation of material in the central region triggers bursts of star formation (Hawarden et al., 1986; Knapen et al., 1995; Sheth et al., 2005), resulting in the formation of nuclear disks or rings (Sormani et al., 2018a; Seo et al., 2019; Gadotti et al., 2019).

The observational study of nuclear disks is a relatively recent field, because it needs to rely strongly on the high angular resolution provided by space-based telescopes or ground-based infrared instruments supported by adaptive-optics. Over the past few decades, observations have revealed that nuclear disks are not uncommon in the cores of spiral galaxies (van den Bosch et al., 1994; Comerón et al., 2010; Ledo et al., 2010; Gadotti et al., 2019, 2020). The properties and growth of nuclear disks is also investigated via numerical simulations (see e.g. Sormani et al., 2018a; Seo et al., 2019). They are characterized by high star and gas densities and intense star formation (Kennicutt et al., 2005), concentrated in a relatively small volume, which can range from radii as small as 10 pc (Comerón et al., 2010) to $\gtrsim$3 kpc (Knapen, 2005). Nuclear disks are kinematically different from the much larger galaxy disks, showing differential rotational velocities and lower velocity dispersion.

In Fig. 1.1, we show an image of NGC 1097, a barred spiral galaxy in the local universe at z $\sim$ 0.003. This galaxy presents a textbook example of a nuclear ring in a barred galaxy. In the zoomed-in view, we can see the nuclear ring, where its intense star formation is shown in pink and purple. We plot the rotation velocities and velocity dispersion inferred from observations by Gadotti et al. (2019). The velocity dispersion of the ring is clearly lower than that of the surrounding disk which underlines its nature as a young, dynamically cold structure.

[1]There is no unambiguous definition that distinguishes nuclear disks from nuclear rings. Some researchers, such as Comerón et al. (2010), set the criterion that the width of a ring must be at most half the ring's radius; otherwise, the nuclear ring is referred to as a nuclear disk. Others simply consider the nuclear ring to be the outer part of the nuclear disk. Throughout this text, we will refer to these structures by the names they are commonly called in the literature. For example, in the case of the galaxy NGC 1097, we will use "nuclear ring," and in the case of the Milky Way, we will use "nuclear disk."

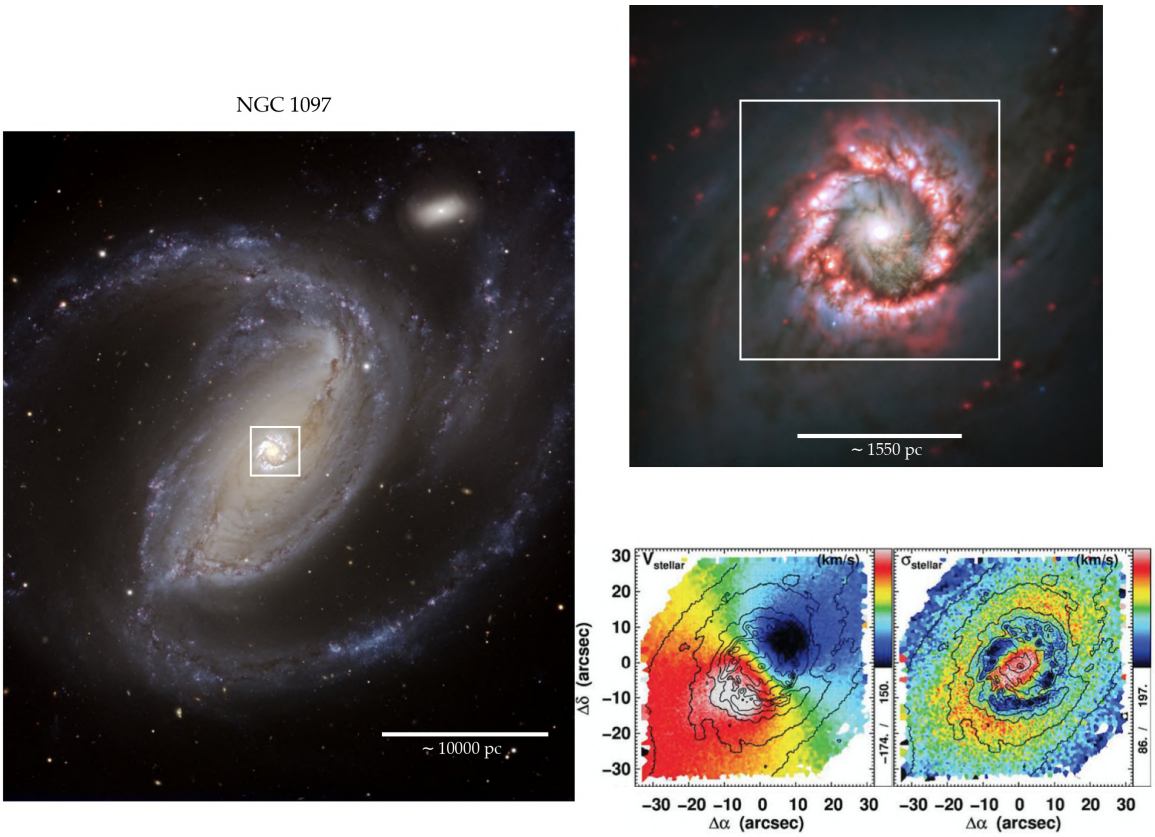

Fig. 1.1 Left: an almost-true color composite based on images made with the multi-mode VIMOS instrument on ESO's VLT. Credit: ESO. Top: Detail of its nuclear ring in the optical range acquired with the MUSE instrument on the ESO's VLT. Credit: ESO/TIMER survey. Bottom: Rotation velocity (left) and velocity dispersion (right). Credit: Fig. 3 in Gadotti et al. (2019)

These structures exhibit special features that make them of fundamental astrophysical interest. For example, they are very sensitive to galaxy-galaxy collisions, which can render them unstable and cause them to quickly disappear after such interactions (Ledo et al., 2010). This sensitivity makes them a useful tool to constrain the assembly history of galaxies because their absence may point to a recent major merger. Additionally, recent studies have shown through simulations that nuclear disks can be used to estimate the age of the Galactic Bar in MW-type galaxies. Since nuclear disks are formed by the funneling of gas through the bar, studying the age distributions of stars in the nuclear disk can help constrain when the Bar first appeared (Baba and Kawata, 2020). Furthermore, the extreme conditions in the central molecular zones, where nuclear disks form, which are quite different from those observed in the galaxy disks, make them very useful for studying mean relations between the properties of molecular gas and the intensity of star formation in extreme environments (Henshaw et al.,

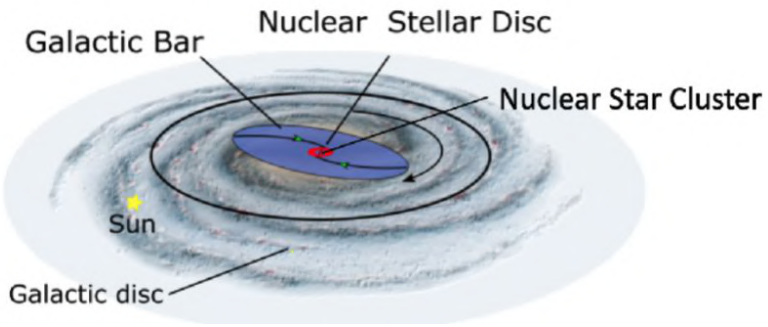

Fig. 1.2 Artistic representation of the Milky Way and its main features. Not to scale. The distance from the Sun to the NSD is $\sim$ 8 kpc. The NSD is about 300 pc in diameter. Credit: Courtesy of Mattia Sormani

2023). Due precisely to those extreme conditions of density, temperature, magnetic field, and turbulence, the central region of the Milky Way is the closest analog we have of a star forming region of the early universe (Kruijssen and Longmore, 2013).

Gadotti et al. (2020) analyzed a sample of 21 nearby ($z < 0.01$) barred spiral galaxies. They found that most of them, 19, present a nuclear ring and our galaxy seems to follow this trend. The presence of a rotating bar at the Milky Way's center has been confirmed in different studies through spectroscopic and kinematic analyses (see e.g. Queiroz et al., 2021; Rich et al., 2007). Additionally, several studies have identified a nuclear disk at the core of the Bar, the so-called Nuclear Stellar Disk (NSD), with the first clear reference to its existence coming from Launhardt et al. (2002). In Fig.1.2 we show a artistic representation of the Milky Way' structure to illustrate the location of the NSD

The NSD has a diameter of $\sim$300 pc, with a scale height of about 45 pc and a mass of 10^9 $M_\odot$ (Launhardt et al., 2002; Valenti et al., 2016; Gallego-Cano et al., 2020; Sormani et al., 2022). The NSD is an environment of extreme conditions. Its stellar density ranges about 10^4 to 10^5 times higher than that in the Galactic disk (Schödel et al., 2007, 2018). The star formation rate is the highest in the Galaxy when averaged by volume (Schödel et al., 2007; Mauerhan et al., 2010). In Fig. 1.3, we show a mosaic of the few hundred parsecs of the Galactic Center, where we can appreciate the NSD as a clear overdensity of stars.

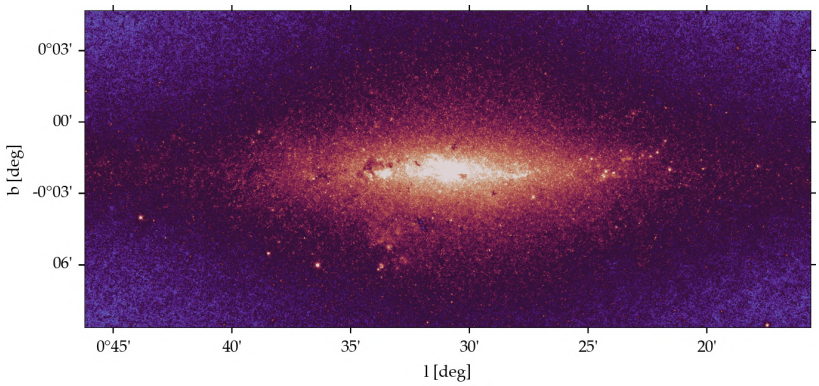

Fig. 1.3 Mosaic of the GC created with Spitzer IRAC (Channel 2, 4.5 μm) images from the GLIMPSE survey.

Through the analysis of the line-of-sight velocities of hundreds of individual stars from the spectroscopic survey APOGEE (Majewski et al., 2017), Schonrich et al. (2015) estimated the rotation velocity of the NSD to be $\sim$ 80 km/s, and found it to be kinematically cooler than the population of the surrounding Galactic bar. In Fig. 1.4 we can see the clear rotation pattern of the NSD. More recent studies by Schultheis et al. (2021), using spectroscopic data from KMOS/VLT, confirmed these results and provide further evidence on how the NSD is kinematically and chemically different from the Bar. A similar kinematic structure and rotation velocities were derived from the study of OH/IR masers by Lindqvist et al. (1992).

The velocity rotation of the NSD can also be determined via a statistical analysis of proper motions (Shahzamanian et al., 2022; Nogueras-Lara, 2022; Martínez-Arranz et al., 2024a). According to Fig. 1.4, the direction of the NSD rotation is clockwise, when seen from the Galactic north pole. Therefore, if we analyze the proper motion distribution for the stars of the NSD, we would expect to find a population moving eastward, corresponding to stars from the near side of the NSD, and a population moving westward, corresponding to stars from the far side. The blue histogram in Fig. 1.5 represents the observed kinematics of the proper motion component parallel to the Galactic plane, from the catalog by Shahzamanian et al. (2022). In this catalog we combined the GALACTICNUCLUES survey (Nogueras-Lara et al., 2019a) with the HST Paschen-α survey (Wang et al., 2010; Dong et al., 2011) to build a proper motion catalog of about 80000 sources covering an area of $\sim$ 550 arcsec^2 on the NSD. To disentangle the populations of the NSD and the Bar, we fitted different models to the distribution. We found that the best model corresponds to three Gaussians. We printed at the top of the figure the parameters of these Gaussians. The mean velocities for the red and orange ones are $|\mu_l| \approx 2$ mas/yr, that at the GC distance correspond to $\sim$ 80 km/s. These Gaussians represent the movement of the stars in the near and far side of the NSD, and their

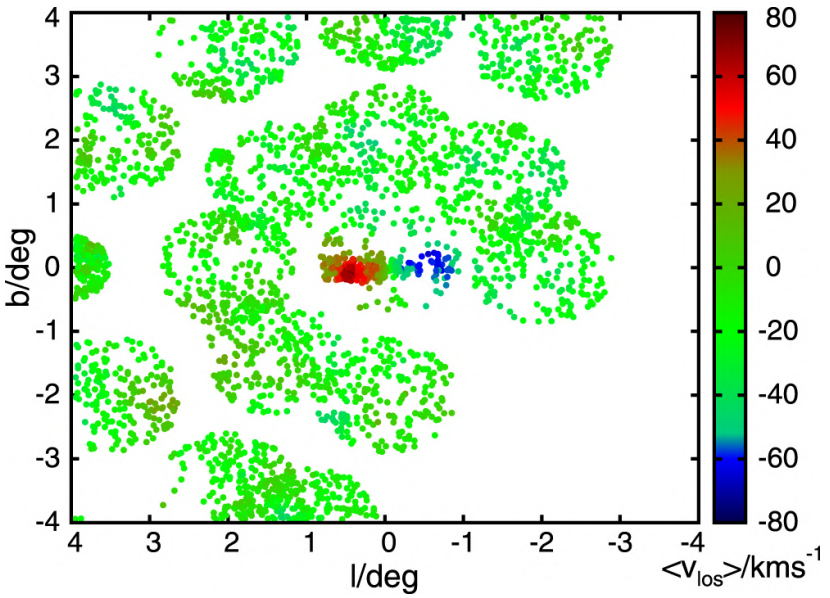

Fig. 1.4 Plot and caption correspond to Fig. 1 in Schonrich et al. (2015): ***Fig. 1**: Overview of APOGEE stars (colored dots) near the Galactic center in Galactic longitude l and latitude b. Colors represent the mean line-of-sight velocity v_{los} of each star and its closest 29 neighbors. Note the division into plates/fields and the clear dipole structure in v_{los} around the Galactic center.*

mean values agrees with the velocity rotation derived from spectroscopic data by Schonrich et al. (2015).

By combining proper motions and extinction it is also possible to distinguish between the near and far population of the NSD. Because of the large amount of gas and dust in the NSD, the extinction value is highly dependent on the line-of-sight distance (Nishiyama et al., 2009), so we can separate the near- and far-side stars by their extinction levels. Since the vast majority of observable stars are red clump stars, which exhibit a well-known intrinsic color with a small variation, $(H\text{-}Ks)_0 = 0.1 \pm 0.01$ (Girardi, 2016; Nogueras-Lara et al., 2021a), we can assume that the variation in the color of these stars is mainly caused by extinction. Therefore, we can use the variation in colors as a proxy for extinction and, hence, for line-of-sight distance. In Shahzamanian et al. (2022) we divided the catalog using two different color cuts. Forthe first one we select star with color $H-Ks < 1.7$[2], which correspond extinction level of stars on the near side of the NSD. For second cut only stars with color $H-Ks > 1.9$, which correspond extinction level the stars in the far side. In Fig. 1.6 we show the mean values of the component parallel to the Galactic plane for these two groups, where the rotational motion of the NSD becomes evident.

[2]We previously eliminated all foreground stars by a color cut $H-Ks > 1.3$ (see Nogueras-Lara et al., 2019a)

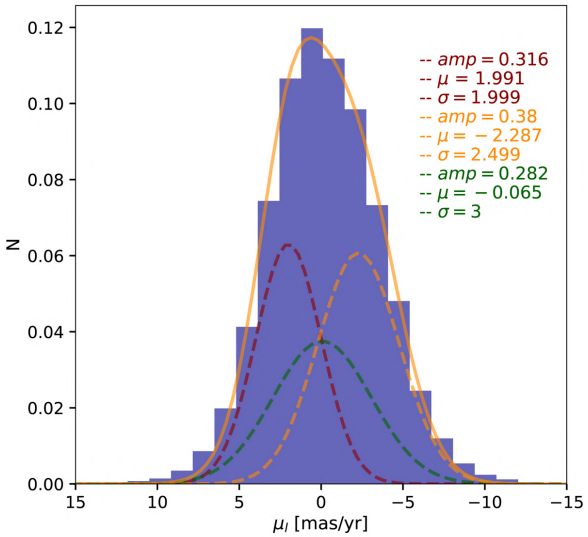

Fig. 1.5 The blue histogram represent the proper motion distribution for the component parallel to the Galactic plane form the catalog by Shahzamanian et al. (2022). Red and orange dashed Gaussian represent the population of the NSD moving westwards and eastward. The green Gaussian represents the Bar population. Credit: Fig. 9 in Shahzamanian et al. (2022)

Furthermore, simulations combined with observational data have come to similar conclusions about the properties of the NSD. For example, using the APOGEE data set and the KMOS data from Fritz et al. (2021), Sormani et al. (2022) created a kinematic model of the NSD, verifying the parameters that were previously estimated through observations. In Fig. 1.7, we show some results of the NSD simulation done by Sormani et al. (2022). We can see that the estimated mass matches the ones derived from observations, $\sim 10^9 M_\odot$, and the rotation velocity agrees with the values found by Schonrich et al. (2015) and Shahzamanian et al. (2022) (see Fig. 1.4 and Fig. 1.5)

1.2 The Central Molecular Zone

Overlapping with the NSD and having comparable scale height and velocity, we find the Central Molecular Zone (CMZ, Molinari et al., 2011; Henshaw et al., 2016), an accumulation of gas and dust inside the central ∼500 pc of the GC. It results from the inflow of interstellar gas, about $1 M_\odot$/yr, driven by the Galaxy Bar (Sormani and Barnes, 2019). The CMZ harbors the largest concentration of of molecular gas in the entire Galaxy, with about the 5% ($\sim$ 5 x $10^7 M_\odot$) of its whole molecular gas reservoir concentrated in less than 1% of its volume (Morris and Serabyn, 1996; Ferrière et al., 2007). The density, temperature, magnetic

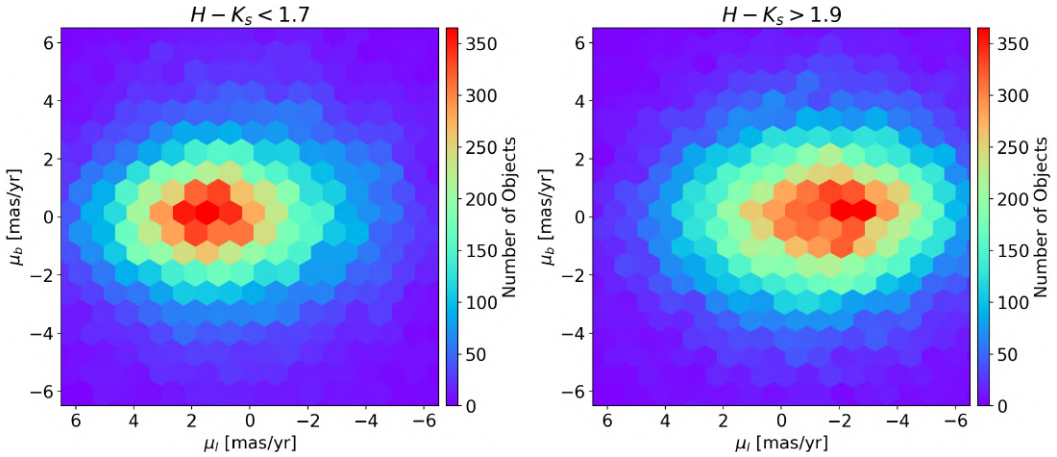

Fig. 1.6 Proper motion density plot of the component parallel to the Galactic plane as a function of reddening, from the catalog by Shahzamanian et al. (2022). Left: Low reddening. Right: High reddening. Credit: Fig. 10 in Shahzamanian et al. (2022)

field and velocity dispersion in the CMZ are orders of magnitude higher than those in the Galactic Disk (Shetty et al., 2012; Ginsburg et al., 2016; Longmore et al., 2017). Depite of these extreme conditions, or maybe because of them, in the last $\sim$ 100 Myr, the volume-averaged star formation in the NSD has been about 100 times higher than in the Galactic disk. Nevertheless, its star formation rate (SFR) is still at least an order of magnitude lower than expected given the amount of gas present in the area (Longmore et al., 2013a). Based on observations of dense molecular clouds that populate the CMZ, it has been proposed that the density threshold for gas in the GC environment is higher than the one required to trigger star formation in the Galactic disk (Johnston et al., 2014; Rathborne et al., 2015; Ginsburg and Kruijssen, 2018). This evidence is still insufficient to fully explain the peculiar lack of star formation in the CMZ. However, it does suggest that environmental factors are key to understanding the star formation process in such different environments as the Galactic disk and the GC. Thus, studying star formation in this extreme environment is crucial to improve our understanding of the relationships between molecular gas clouds and star formation rate.

Of particular interest in this regard are the dense clouds in the CMZ, which can be found mostly inside the NSD, for example in the Sgr B2 region or in the dust ridge that extends from the latter further inwards in projection. An extreme example of the different conditions of star formation in the GC, is the case of the dense molecular cloud G0.253+0.016, also known as the Brick. This cloud, with a mass of $\gtrsim 10^5$ $M_\odot$ concentrated within a projected radius of just $\sim$ 2-3 pc, a temperature of 20-30 K, and a column density of $\sim$ 8 x 10^4 cm^{-3}, has the potential to form a cluster as massive as the Arches (Lis et al., 1994; Kauffmann et al., 2013; Rathborne et al., 2015). Instead, this molecular cloud with possibly uniquely

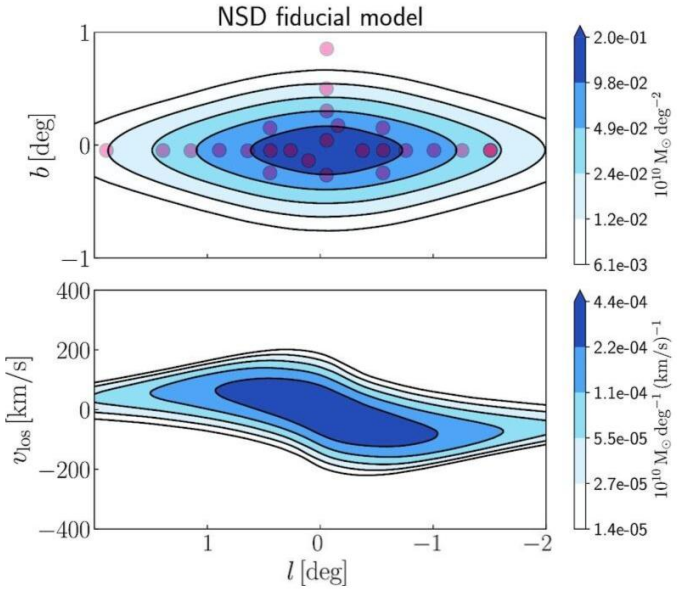

Fig. 1.7 NSD model by Sormani et al. (2022). Top: Mass distribution of the NSD, with red circles representing the KMOS data on which the model was constructed. Bottom: Velocity profile. 1 deg corresponds to $\sim$ 140 pc. Credit, Fig. 8 in Sormani et al. (2022).

extreme density and mass as compared to other clouds in the Milky Way, shows hardly any signs of star formation (Longmore et al., 2012; Mills et al., 2015).

Some hypotheses propose that the star-forming activity of the Brick and other dense molecular clouds in the GC is closely related to their orbital dynamics (Longmore et al., 2013b; Kruijssen et al., 2015). Thus, knowing the parameters of these features, such as positions and velocities, is key to shedding light on their unknown star-forming mechanisms, which seem to ignore the Kennicutt–Schmidt law (Schmidt, 1959; Kennicutt, 1998).

1.3 Young star clusters in the GC

A stellar cluster is a perfect place to study how the environment affects the outcomes of star formation. In order to understand the star-forming processes in the GC, we need to study the clusters present today in the GC. Recent studies of the Arches and Quintuplet clusters (Hosek et al., 2019; Gallego-Calvente et al., 2021, 2022) and also of young stars in the central parsec cluster (Bartko et al., 2010; Lu et al., 2013), have identified an excess of massive stars in the three of them, suggesting that their initial mass function (IMF) differs from that in the Galactic disk. Locating other clusters or stellar associations in the NSD and studying their mass distribution is crucial to better understand the IMF that operates in this environment.

Apart from the central parsec cluster, the Arches and the Quintuplet, no other clusters have been unambiguously defined in the NSD. This contrasts with recent observations that predicted that $\sim 10^6$ $M_\odot$ have formed in the NSD in the last 20-30 Myr (Matsunaga et al., 2011; Nogueras-Lara et al., 2020). According to these estimates, at least a dozen more young clusters should exist in the region. This discrepancy has come to be known as the "missing cluster problem".

Three main causes are responsible for this discrepancy. The first is linked to the extreme tidal forces in the area, capable of dissolving even the most massive clusters in less than 10 Myr (Kim et al., 1999; Kruijssen et al., 2014). Thus, clusters could have actually formed during the star-forming episodes of the last 30 Myr and then dissolved beyond recognition. The presence of massive young stars, apparently in isolation and scattered throughout the NSD, could be an indicator of this process (Dong et al., 2015; Clark et al., 2021). The second cause is the observationally challenging environment, which we will discuss further in the next section.

1.4 Observational Constrains

When studying the stellar population and features of the GC, there are two main constraints that play a fundamental role: crowding and extinction.

Crowding

The stellar density in the GC is the highest in the Galaxy and can reach levels up to 1 million times that of the Galactic disk (Schödel et al., 2007, 2018). This makes it impossible to identify structures by visual inspection looking for overdensities of sources, as even the most massive clusters blend with the dense stellar background. To illustrate this, in Fig. 1.8, we show the central area of the GC, approximately 200 pc $\times$ 150 pc. The positions of the Arches and Quintuplet clusters are marked with green arrows. The $\sim 10^4$ $M_\odot$ Arches cluster almost completely blends with the stellar background. A stellar association or a cluster less massive than the Arches would be impossible to detect by searching for local stellar overdensities. Even a cluster as massive as the Arches or the Quintuplet will be undetectable in a few more Myr in this environment (Kim et al., 1999; Kruijssen et al., 2014).

In order to be able to detect clusters or stellar associations in this regions, it is not sufficient to look for overdensities in the positions; we have to combine it with other parameters. To illustrate this point, we show in the left panel of Fig. 1.9 an HST image of the Quintuplet cluster by Hosek et al. (2022), and in the middle panel, a histogram of the detected number of sources in this area. Even with dedicated pointing on the area of the cluster, there is no

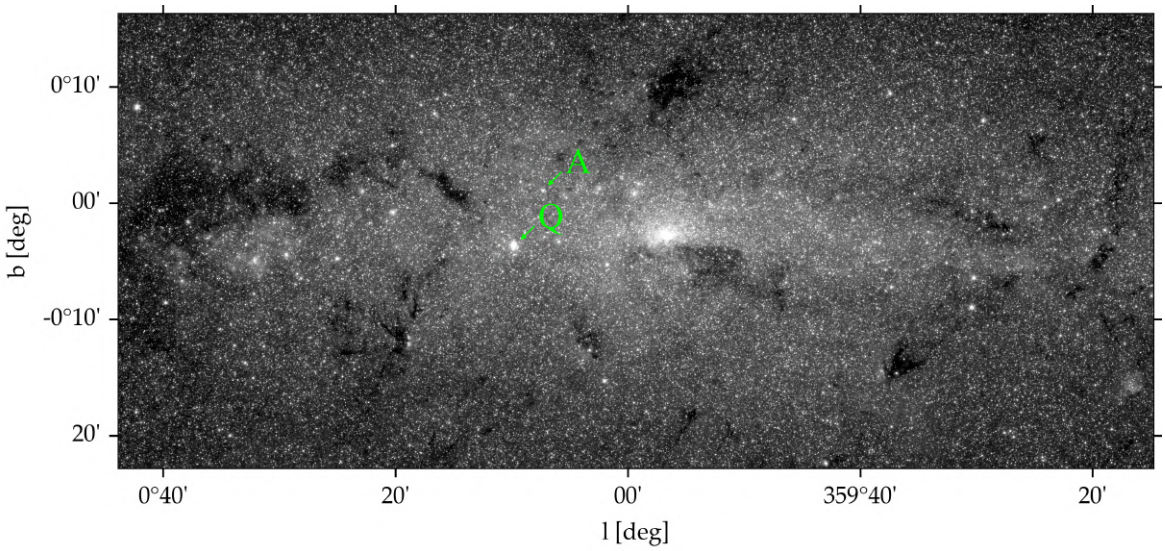

Fig. 1.8 Image of the GC from 4.5 μm Spitzer/IRAC image (Stolovy et al., 2006). The arrows indicate the positions of the Arches and the Quintuplet clusters. 1° ≈140 pc

overdensity indicating the presence of a massive cluster in the position space. It is only when we analyze the proper motions space, right panel in Fig. 1.9, that the presence of the cluster becomes evident.

Extinction

The interstellar extinction in the NSD is extreme, reaching levels in the optical range of $A_V \gtrsim 30$. Therefore, observations must be made in the near-infrared, where extinction reduces to $A_{Ks} \gtrsim 2.5$ (Schödel et al., 2010). Actually, the extinction is so severe, than even in the near-infrared there are areas in the NSD that are almost completely opaque.

In the J band (1.26 μm), only the brightest stars can be observed. To obtain reasonably deep observations, we need to use the H (1.61 μm) and Ks bands (2.14 μm). The range of of intrinsic stellar colors at [H-K] of the observable stars at the GC spans only about 0.2 mag, compared to reddening, that can lead to about 10 times larger observed colors (Schödel et al., 2010), which imposes a serious restriction on the use of color-magnitude diagrams (CMDs) to distinguish different-aged populations. Another major issue is differential extinction, which in the NSD varies on the scale of arcseconds (Scoville et al., 2003; Gosling et al., 2006; Schödel et al., 2007), and dramatically degenerates the CMDs.

To illustrate the effects that extinction and differential extinction have on CMDs in the GC, we have simulated three different-aged 10^4 $M_\odot$ clusters in the GC. We used the software *Spisea* (Hosek et al., 2020), which allows us to build single-age, single-metallicity clusters at the distance of the GC. In the right panel of Fig. 1.10, we present the H−Ks CMDs of 1, 10,

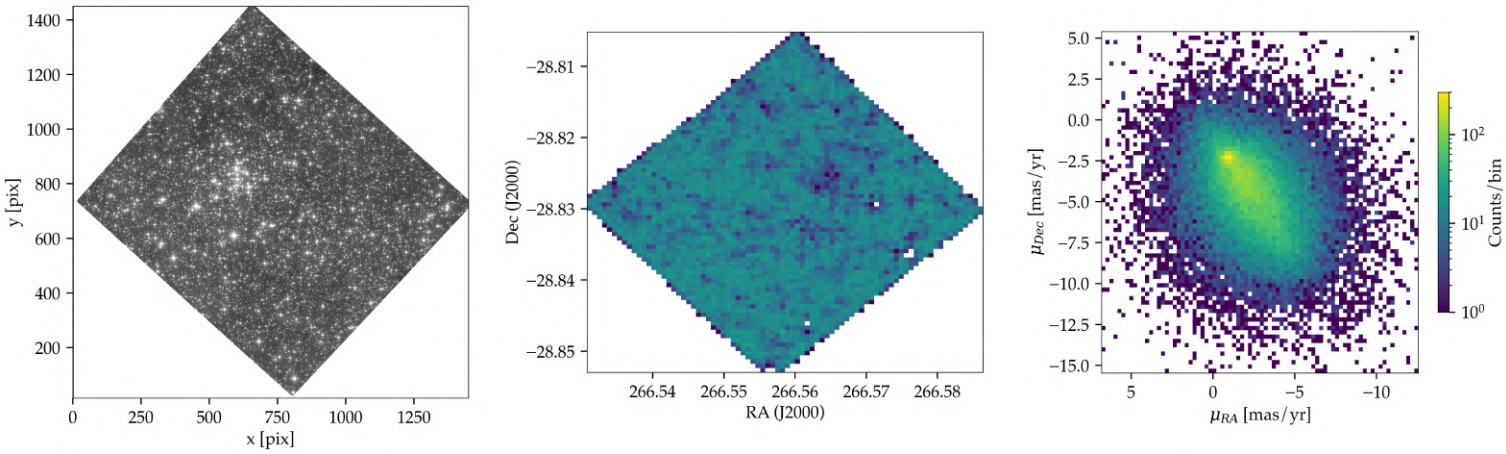

Fig. 1.9 Left: HST image of the Quintuplet cluster (Hosek et al., 2022). Center: Stellar positions histogram. Right: Stellar proper motions histogram. Both center and right histograms use the same color scale.

and 50 Myr old clusters and their respective isochrones assuming no differential extinction. Even without differential extinction, we can see how the isochrones run very close to each other for most of the magnitude range and distinguishing between population is not possible for most of the stars. In the left plot, we set the differential extinction to $dA_{Ks} = 0.1$. In this case, the colors of the star members of each cluster are completely mixed.

1.5 Open questions

The star formation history of the GC has undergone significant revision in recent years. Previous theories of quasi-continuous star formation (Figer et al., 2004) have been revised, and now new observation suggest a history of episodic bursts. These bursts, occurring within the last 1 Gyr, punctuate periods of relative calm. The star formation activity was particularly high between about 30 Myr and 0.1 Myr ago (Matsunaga et al., 2011; Nogueras-Lara et al., 2020). According to the amount of stellar mass that this last star formation episode would have formed, dozens of young stellar cluster should have been born in the NSD, instead only three are known today in the GC, the Arches, the Quintuplet and the central clusters.

One proposed explanation for this discrepancy is the hypothesis that star formation in the GC occurs predominantly in isolation, distinct from the cluster formations observed in more typical environments. This hypothesis finds support in the prevalence of isolated massive young stars (Dong et al., 2011) and the limited presence of stellar clusters. Some other studies suggest that the tidal forces the in the GC would have completely dissolved any cluster formed more than 10 Myr ago (Kim et al., 1999; Kruijssen et al., 2014).

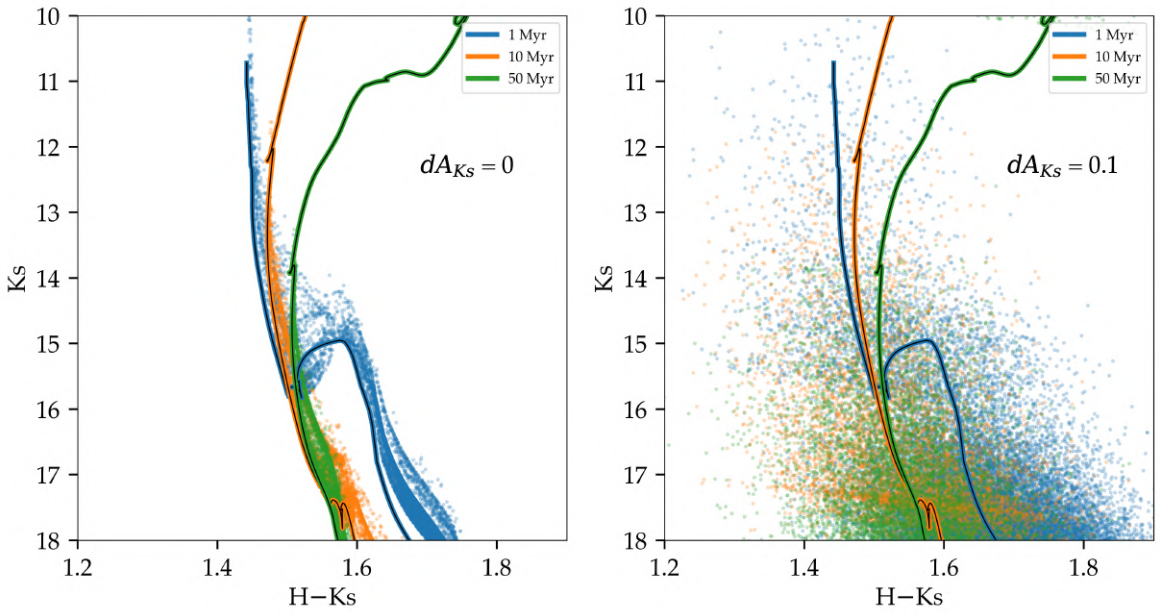

Fig. 1.10 CMD of simulated clusters. Left: Colored dots represent three $10^4 M_\odot$ clusters of 1, 10 and 50 Myr at the distance of the GC, 8.2 kpc. Lines represent the isochrones. We set the differential extinction to $dA_{Ks} = 0$. Right: Same simulations as left, but we set $dA_{Ks} = 0.1$

With the observational data we have today, we cannot determine whether the star formation mechanism of massive stars in the GC produces them mainly in isolation, or whether the main mechanism is to form them within a cluster. These possibilities raise different questions. In the first case, how does star formation in the GC differ from that in the Galactic disk, where massive stars form mainly within clusters? On the other hand, if formation within a cluster is the main mechanism, where are the clusters found?

Recent studies of the IMF within GC clusters reveal fundamental differences from IMFs observed in the Galactic disk. Specifically, the GC IMF appears to be top-heavy, with an overrepresentation of massive stars (Bartko et al., 2010; Hosek et al., 2019). This raises questions about the prevailing star formation processes: Why does the GC seem to produce a top-heavy IMF, and what does this imply about the unique conditions and processes influencing star formation in this region compared to the Galactic disk? This underscores the importance of studying additional clusters within this unique environment.

Closely related to the star formation in the GC are the dense molecular clouds present in the NSD. Some of these clouds happen to be some of the densest molecular clouds in the Galaxy, and in some cases show evidence of little or no star formation. The position within the NSD of these dense gas structures is key to understanding their apparent lack of star

formation. However, the three-dimensional shape and dimesinon of the NSD and CMZ are unclear. In addition, some studies have cast doubt on the precise positioning of one of these molecular clouds, known as Brick, within the GC (Zoccali et al., 2021). Further analysis is needed to pinpoint the shape and parameters of this complex region.

One way to study the dimensions and general shape of the NSD is through proper motion analysis. Recent studies have used Gaia's proper motion to identify large structures and clusters (Castro-Ginard et al., 2018; Laporte et al., 2022). The Gaia mission (Gaia Collaboration et al., 2016) and its latest data release provide precise proper motions for billions of sources, but unfortunately, it is blind to the GC. Nevertheless, Hosek et al. (2022) successfully linked the proper motions of stars in the Arches and Quintuplet clusters to the Gaia reference frame, allowing them to derive the stars' absolute motions and recalibrate their orbits. However, this study covers an area of less than 60 pc^2. A comprehensive proper motion catalog of NSD stars would enable a detailed study of the NSD and CMZ structures and dynamics.

Chapter 2

Objectives, Methods and Results

The use of proper motions has proven to be a powerful tool for the analysis of the Galactic disk and halo. For example, using proper motion analysis, open clusters or MW disk structures have been identified by analyzing Gaia data (Castro-Ginard et al., 2018; Laporte et al., 2022). Unfortunately, the GC is invisible to Gaia due to high extinction levels and extreme crowding. The main goal of this thesis is to introduce novel methodologies and tools to investigate the GC environment through proper motion analysis and shed some light on some of the open questions exposed in Sect. 1.5. In this section, I provide an overview of the objectives, methodology, and main results of my thesis.

2.1 Objectives

This research focuses on three main goals. The first is to constrain the distance to a dense molecular cloud in the GC by means of proper motion analysis. The second goal is to identify co-moving stars in the GC through the combination of proper motions and photometry catalogs, which could pinpoint the positions of young clusters. By investigating these topics we aim to provide insights into pressing issues in the field, such as the relation between the properties of molecular clouds and star formation or the 'missing cluster problem' in the NSD.

These objectives are limited by two factors: the extent of the available catalogs, which cover only a small percentage of the NSD area, and the precision of the data. To obtain valid results, we must use proper motions with the lowest uncertainty, which results in the loss of a substantial fraction of the data. Therefore, the third objective of this thesis is to prepare the creation of a large catalog of proper motions and photometry, covering a larger part of the NSD with high precision, to enable deeper observations. Through the forthcoming reduction and analysis of the new proper motions catalog, which combines the

GNS observations forn 2015 (Nogueras-Lara et al., 2019a) with a new epoch acquired in 2022, we anticipate discovering and confirming additional clusters. Ultimately, our goal is to contribute to resolving one of the central enigmas of the GC: Does the IMF in this extreme environment deviate fundamentally from that observed in the Galactic disk?

Throughout this thesis, we illustrate the application of novel methodologies and tools with two specific case studies. Importantly, these methods are designed to be broadly applicable across the entire NSD. Additionally, in the final section of the thesis, we present preliminary work for the upcoming GNS catalog.

2.2 Methods

The general methodology we have followed throughout the course of this research involves the analysis of proper motion catalogs in combination with photometric and spectroscopic data. In the following section, we will briefly describe the techniques used to constrain the line-of-sight distance to a molecular cloud in the GC, the identification of co-moving groups, and the confirmation of one of these co-moving groups aa a newly discovered potential young star cluster in the NSD. For a more detailed description of the methodology, please refer to the sections 3.2, 4.3, and 5.2.

2.2.1 Distance to the Brick

Models and observations show that the Bar and the NSD have different kinematic properties. Therefore, we can distinguish the Bulge stars from the NSD stars based on their proper motions: the Bar population, with a high velocity dispersion and a mean velocity of zero; and the NSD population, with a lower velocity dispersion and a mean rotational velocity of about 80 km/s parallel to the Galactic plane. (see e.g. Gadotti et al., 2020; Schultheis et al., 2021; Shahzamanian et al., 2022; Sormani et al., 2022). At the same time, the stellar population of the NSD can be divided into two groups: one streaming to the Galactic east on the near side of the NSD and one streaming west on the far side. To illustrate this point, we used the Action-based Galaxy Modelling Architecture software (*AGAMA*[1], Sormani et al., 2022) to recreate a simplified model of the NSD, that we show in Fig. 2.1. For clarity, we excluded the stars from the Bar and depicted only the stars on the outer edges of the disk. The arrow indicates the line of sight, and the colors represent the velocity along the y axis, v_y. The black circle represents a dense molecular cloud, whose size we have exaggerated. The dots with

[1] https://github.com/GalacticDynamics-Oxford/Agama

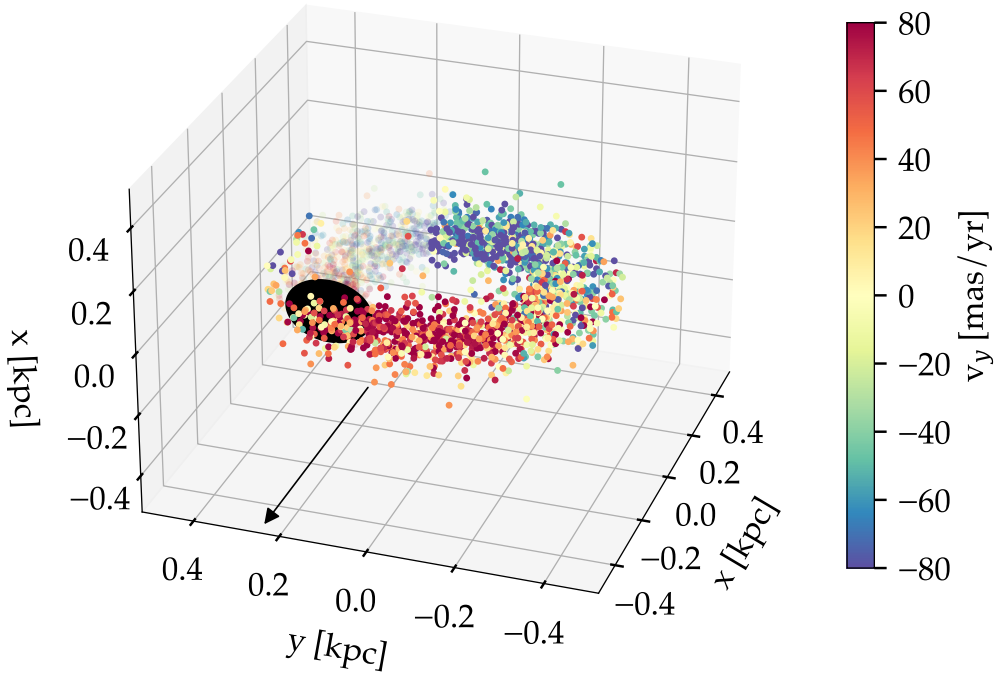

Fig. 2.1 Representation of the NSD. Arrow indicates line of sight from Earth. The colors represent the velocity v_y. The black circle represents a dense molecular cloud. Dots with lighter opacity represent stars hidden from view by the cloud.

lighter opacity represents the stars behind the cloud. The rotation pattern is evident in this model.

According to this model, if we analyze the proper motion distribution of an area free of dense molecular clouds in the NSD, we should be able to identify two populations with different mean motions: one moving east and the other moving west, plus the kinematically distinct population from the Bar (not included in the model). On the other hand if we analyze the proper motions of a area in front of a dense molecular cloud we will not detect the NSD population from the far side.

To illustrate the first case, we used the catalog from Libralato et al. (2021a) to analyze the proper motions of stars in an area of the NSD free of dark clouds. The histogram in Fig. 2.2 represents the component of the proper motions parallel to the Galactic plane [2]. To disentangle the different populations that form this distribution, we fit different combinations

[2]There is also a proper motion component perpendicular to the Galactic plane, but it is not relevant for this analysis.

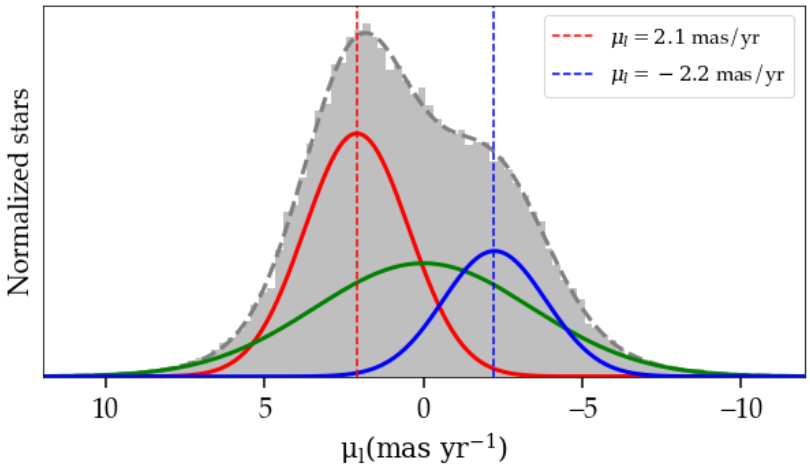

Fig. 2.2 The gray histogram represents the distribution of proper motions parallel to the Galactic plane from the catalog by Libralato et al. (2021a). The overplotted curves represent the Gaussians that best fit the distribution. The colored boxes show the peaks of the corresponding Gaussians and the equivalent values in km/s.

of Gaussians to it. We found that the best fit corresponds to three Gaussians, representing two different populations: the Bar (green) and the NSD (red and blue). The two Gaussians representing the NSD peak at approximately $\mu_l \approx |2|$ mas/yr (dashed lines in Fig. 2.2) which correspond to $\sim$ 80 km/s at the GC distance. These values agrees with the ones derived from spectroscopic data from Schonrich et al. (2015) and the simulations by Sormani et al. (2022). Similar values were found by analyzing proper motion catalogs in the GC by Shahzamanian et al. (2022).

In order to illustrate the second case, we studied the proper motion in front of the dense molecular cloud G0.253 + 0.016, a.ka. the Brick. If this cloud is inside the NSD, it would block the far side population (which would correspond to the blue Gaussian in Fig. 2.2) but not the near side population (red Gaussian). In the other hand, if the Brick is in front of the NSD (Zoccali et al., 2021) it will block both near and far side population and we will only observe the proper motion distribution of Bar stars

2.2.2 Identifying co-moving groups of stars

Stars are born from dense molecular gas. The velocity of this gas will be imprinted on the velocity distribution of the young stars. Effects such as two-body relaxation or tidal encounters with massive molecular clouds - the dominant effect at the GC (see Kruijssen et al., 2014) - will disrupt the spatial and kinematic coherence of groups of young stars after

less than 10 Myr in the GC. However, there exists a window of a few Myr after the birth of a cluster or association during which it will be detectable as a co-moving group.

We searched for such groups of young stars by looking for over densities in position-velocity space. For the proper motions we used the catalog by Libralato et al. (2021b). It contains the proper motions of $\sim$ 800.000 objects. We combined it with the astrophotometry catalog from the GNS (Nogueras-Lara et al., 2018), that provided us with H and Ks magnitudes. The combination of these two catalogs allowed us to obtain, for each star, four of the six parameters that span the position-velocity space. In addition, we constrained the third dimension in the position space, the line-of-sight distance, using the color, H$-$Ks, as a proxy. Considering the large variation of extinction along the line of sight in the GC (Nishiyama et al., 2009) and the relatively constant intrinsic color of the observable stars (in their vast majority late-type giants near the Red Clump) we assumed that the observed color was dominated by extinction, which implies that stars with similar colors will lie at similar locations along the line-of-sight. Hence, we could define a five dimensional space to look for overdensities, three dimensions for positions and two for velocity.

In order to find overdensities in the combined catalog of positions and velocities we developed a tool based on the Density-Based Spatial Clustering of Applications with Noise (DBSCAN) algorithm (Ester et al., 1996). A similar method was successfully used to search for open clusters in the Galactic disk , using Gaia data (Castro-Ginard et al., 2018). We tested our algorithm using proper motions data for the Arches and Quintuplet cluster presented by Hosek et al. (2022), and obtained the same results within the uncertainties.

2.2.3 Spectroscopic confirmation of young stars

We can define a cluster or stellar association as a group of stars that move together and are relatively close in position. Due to the extreme crowding of stars at the GC (Schödel et al., 2007, 2018), and the fact that the stars show a coherent eastwards or westwards streaming motion in the NSD (depending on whether they are located in front or behind the plane of the sky), this criterion may not be sufficient to reliably identify a cluster in the NSD. We can add to the selection criterion that the member stars of a potential cluster have to be young. Since stellar colors are of very limited use to classify stars in the extremely reddened GC environment (see e.g. Nogueras-Lara et al., 2019a), this requires spectroscopic observations. Late-type giants, the by far dominating observable stellar type at the GC, show prominent CO-bandhead absorption in their spectra. The absence of this feature and the presence of H and He absorption lines are markers for hot, massive early type , and therefore young stars.

We reduced and analyzed spectroscopic data, acquired with the ESO VLT KMOS multi-object integral field spectrometer, from an area that partially overlaps with the candidate

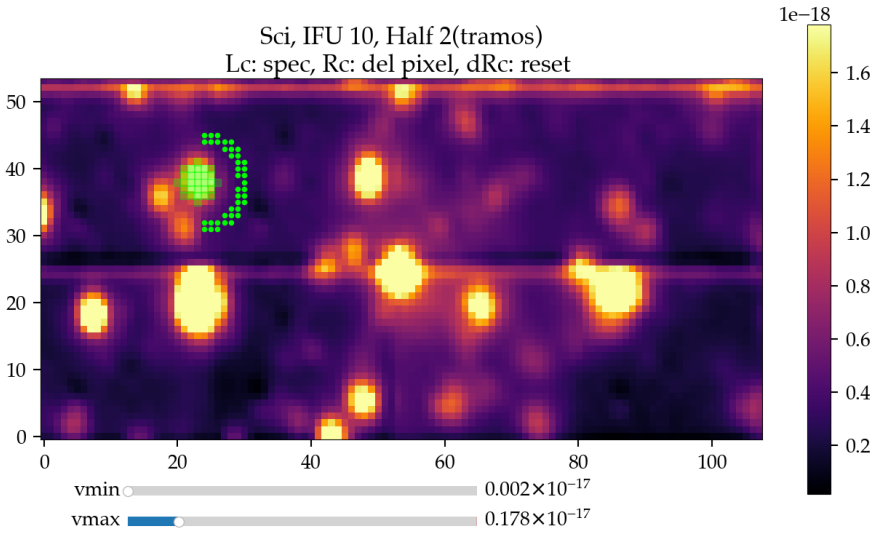

Fig. 2.3 Spectrum extraction software for spectroscopy field data. Green squares mark the extraction area. Green circles mark the pixel used for sky subtraction. In this case the software is avoiding to select as sky the two bright sources close to the target star.

clusters we found in Martínez-Arranz et al. (2024a). First, we reduced the data using the standard KMOS pipeline provided by ESO (Freudling et al., 2013). Next, we extracted the spectra of the field objects and cross-referenced them with the astrophotometry catalog. For the extraction of the spectra we developed a specific tool to extract spectra by clicking on the desired stars, adjusts the sky subtraction to avoid pixels with stellar emission or defective pixels and subsequently normalizes the spectrum. In Fig. 2.3 we show a screenshot of the spectrum extraction software. Finally we provide the field stars with proper motions using the Libralato et al. (2021b) catalog.

2.3 Results

We summarize here the main results of PhD project, which are described in detail in Sections 3.3, 4.4, and 5.3.

2.3.1 Distance of the Brick molecular cloud

We obtained proper motions for two different fields, the Brick field and a nearby comparison field, on a nearby area. In the comparison field, which is free of molecular clouds, we clearly distinguished the population from the Bulge and the population from the NSD. The NSD

population consists of two groups: the group in the near edge of the disk, which moves eastward, and the one from the far side, which moves westward. In contrast, in the Brick field, the latter component is missing due to obscuration by the Brick itself. The fact that the stars from the far side are missing, while those from the near side are present, indicates that the Brick is actually located inside the NSD, constraining its distance to $\sim$ 8.2 kpc, and not at $\sim$ 7.2 kpc as proposed by Zoccali et al. (2021). Similar analysis is applicable to others dense molecular cloud in the GC.

2.3.2 Co-moving groups

We created a tool to find overdensities of stars in a 5D space, spanned by two coordinates in position, two in velocity, and one in extinction, as a proxy for the distance along the line-of-sight. Based on this data, we developed a methodology that allowed us to look for co-moving groups in an environment as crowded as the NSD. We have found three co-moving groups that contain previously known massive young stars (Clark et al., 2023), indicating that these structures must be relatively young. These co-moving groups probably pinpoint the positions of stellar clusters or associations formed in the NSD. The estimated masses of these clusters range from 3500 to 6000 $M_{\odot}$, with radii between 1.5 and 2.2 pc. Considering the recent findings of star formation in the GC, where approximately 10^6 $M_{\odot}$ of young stars formed in the recent history of the NSD, we expect to find more of these comoving groups when analyzing future catalogs encompassing a larger area of the NSD.

2.3.3 Cluster confirmation

Through spectroscopic analysis of areas that partially overlap with one of the co-moving groups described above, we located seven massive stars. Analyzing the proper motions of these stars and the proper motions of other stars in the field, we concluded that this group of stars forms part of a cluster or stellar association. We estimated the mass of the cluster to M = 1742 $\pm$ 761 $M_{\odot}$, with a maximum age of 5-6 Myr.

Chapter 3

Distance to the Brick cloud

This chapter contains the literal transcript of the published article *Distance to the Brick cloud using stellar kinematics* (Martínez-Arranz et al., 2022). It introduces a novel methodology designed to constrains the distance to the dense molecular cloud known as The Brick, confirming its positions within the NSD. This methodology has broader applicability, extending to other dense molecular clouds within the GC. Additionally, it provides insights into the structure and rotational velocity of the NSD through analysis of proper motion.

Distance to the Brick cloud using stellar kinematics

Á. Martínez Arranz[1], R. Schödel[1], F. Nogueras-Lara[2], and B. Shahzamanian[1]

[1]*Instituto de Astrofísica de Andalucía (CSIC), University of Granada, Glorieta de la astronomía s/n, 18008 Granada, Spain*

[2]*Max-Planck Institute for Astronomy, Königstuhl 17, 69117 Heidelberg, Germany*

Astronomy and Astrophysics: Galactic structure, stellar clusters and populations. V683, A13

DOI: 10.1051/0004-6361/202243263

Abstract

The Central Molecular Zone at the Galactic center is currently being intensively studied to understand how star formation proceeds under the extreme conditions of a galactic nucleus. Knowing the position of molecular clouds along the line of sight towards the Galactic center has have important implications in our understanding of the physics of the gas and star formation in the central molecular zone. It was recently claimed that the dense molecular cloud G0.253 + 0.016 (the Brick) has a distance of ∼7.20 kpc from the Sun. That would place it outside the central molecular zone, and therefore of the nuclear stellar disc, but still inside the Bulge.

Theoretical considerations as well as observational studies show that stars that belong to the nuclear stellar disc have different kinematics from those that belong to the inner Bulge/Bar. Therefore, we aim to constrain the distance to the Brick by studying the proper motions of the stars in the area.

We used ESO HAWK-I/VLT imaging data from epochs 2015 and 2019, to compute proper motions on the Brick and in a nearby comparison field free of dark clouds.

The stellar population seen towards the nuclear stellar disc shows three kinematic components: 1) Bulge stars with an isotropic velocity dispersion of ∼3.5 micro-arc second per year; 2) Eastward moving stars on the near side of the nuclear stellar disc; 3) westward moving stars on the far side of the nuclear stellar disc. We clearly see all three components towards the comparison field. However, towards the Brick, which blocks the light from stars behind it, we can only see kinematic components 1) and 2).

3.1 Introduction

In the Galactic center, at a distance of ~ 8 kpc (McNamara et al., 2000; Ghez et al., 2008; Genzel et al., 2010), we can find the central molecular zone (CMZ), a flattened structure of gas and dust within a radius of ∼200 pc (Kruijssen et al., 2014; Tress et al., 2020). Occupying a similar space as the CMZ there is the so called nuclear stellar disk (NSD), a rotating structure (Schonrich et al., 2015; Shahzamanian et al., 2022), with a radius of ~ 150 pc and scale heigh of ~ 45 pc (Launhardt et al., 2002; Gallego-Cano et al., 2020; Sormani et al., 2020).

Although most stellar mass in the NSD formed probably $\gtrsim$ 8Gyr ago, it has been one of the most active star forming regions of the Milky Way in the past 100 Myr (Matsunaga et al., 2011; Nogueras-Lara et al., 2019a). Nevertheless, the current star formation rate appears to be about a factor of ten lower than expected, considering the high gas density and dense molecular clouds present in the area (Longmore et al., 2013a).

In order to fully understand the star formation history in the Galactic center and the evolution of the Galactic Bulge, it is crucial to better understand the structures of the NSD and CMZ (Sormani et al., 2022). One important question to address, that would help us move towards a better understanding of this region is where the dense molecular clouds are located along the line of sight (Kruijssen et al., 2015).

In a recent publication by Zoccali et al. (2021), the molecular cloud G0.53+0.016 (the Brick) was suggested to be at a distance of 7.2 ± 0.20 kpc from the Sun; that is outside the NSD, but still inside the Bulge. This result is based on the photometric analysis of the Brick stars, which they found brighter than they should be if they were placed at the Galactic center.

This claim was recently challenged by Nogueras-Lara et al. (2021a), who found that the Brick presents a stellar population compatible with that of the NSD (Nogueras-Lara et al., 2019a), and is located at a distance of 8.4 ± 0.5 kpc, what would place it inside of the CMZ/NSD.

In this letter we cross-check the work of Nogueras-Lara et al. (2021a) with kinematic data, considering one of these two possibilities, based on the assumption that the Brick is mostly opaque to near-infrared light (Longmore et al., 2012) and, therefore, we can only detect stars in front of the cloud: A) the Brick is outside the NSD and inside the Bulge; in that case we would expect to find only stars with typical Bulge proper motions, i.e. zero mean proper motion and isotropic velocity dispersion (Kunder et al., 2012; Shahzamanian et al., 2022). Or B) the Brick is inside the NSD, in which case we would expect to find two different kinematic groups; one belonging to the Bulge population and the other to the NSD itself; i.e with stars on the near side of the disk moving eastward and those on the far side, westward (Schonrich et al., 2015; Shahzamanian et al., 2022).

3.2 Data and methods

We combined imaging data from the wide-field near-infrared camera HAWK-I/VLT from two epochs, 2015 and 2019[1]. The 2015 data, henceforth D15, correspond to the GALACTIC-NUCLEUS survey (GNS, Nogueras-Lara et al., 2018, 2019a), acquired with fast photometry mode and reduced with the speckle holography algorithm (**?**) to provide a 0.2" homogeneous angular resolution (Nogueras-Lara et al., 2019a). The 2019 data, henceforth D19, were acquired with the new GRAAL ground layer AO system with an average angular resolution of 0.4" (Zoccali et al., 2021) for H and Ks bands.

[1]Based on observations made with ESO Telescopes at the La Silla Paranal Observatory under programmes ID 195.B-0283 and ID 0103.B-0262

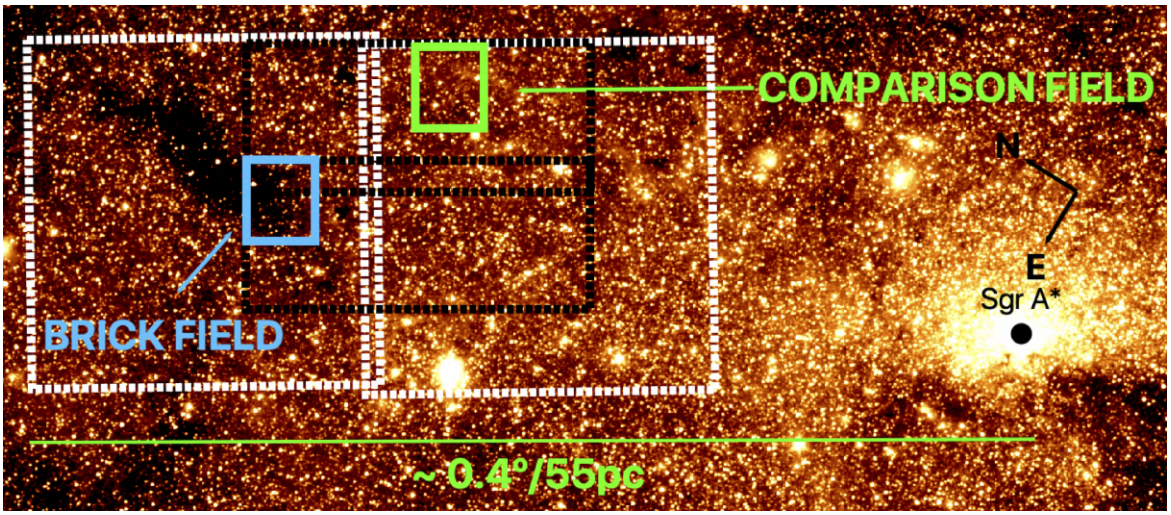

Fig. 3.1 Pointings from GNS (outlined in black) and D19 (in white) overlaid on a 4.5 μm Spitzer/IRAC image (Schödel et al., 2014). The GNS pointings cover smaller areas because of detector windowing. The overlapping areas used for proper motions calculations are shown in blue (on the Brick) and green lines (comparison field).

Table 3.1 Comparison and Brick field coordinates

Field	l(°:′:″)	b(°:′:″)
Comparison	+0:09:50.946	+0:02:53.924
Brick	+0:13:43.943	+0:00:17.924

The images from both data sets overlap on a small region on the Brick, that is outlined in Fig. 4.1, along with the comparison field. Both fields have the same dimensions of 0.027° by 0.034° (3.7 pc by 4.7 pc), centered on the coordinates show on Table 3.1, at a projected distance of $\sim$0.22° / 30 pc and $\sim$0.28° / 39 pc respectively to the galactic east of Sgr A*.

3.2.1 D15 data

The acquisition and reduction of D15 data is described in Nogueras-Lara et al. (2018, 2019a). Due to saturation issues with Ks band for stars brighter than $\sim$11.5 mag, we used for proper motions calculation only H band data.

3.2.2 D19 data

We used two pointings of D19 (outlined in white on Fig.4.1). These data consisted of 15 jittered exposures (DIT = 10s, NDIT = 1) and 32 jittered exposures (DIT = 10s, NDIT = 3), respectively. We applied standard data reduction (sky subtraction, flat fielding, bad pixel correction). The sky was produced from the jittered images, by stacking the different frames and selecting the pixels with the smallest values. This procedure was necessary because the extreme source density towards the target will not result in a homogeneous sky when applying a median. For the photometry and astrometry we used *StarFinder* (Diolaiti et al., 2000). In order to compute the mean position and uncertainties of the detected stars, we aligned all jittered frames taking the first one as a reference, using a linear polynomial and considered stars in different frames as the same if they were less that 1 pixel apart. Due to the long exposure time of these images, non-linearity and saturation effects become increasingly important for stars brighter than $H = 14$, resulting in increased astrometric uncertainties (Fig. 3.2). Therefore, for the fine alignment of the frames we considered only stars with magnitudes $14 \leq H \leq 16$, which have the smallest position uncertainties according to Fig. 3.2 We only accepted stars detected in all frames. We used the mean and the uncertainty of the mean of the positions in all frames. We only used areas covered by at least four pointings.

We calibrated the 2019 data photometrically via common stars with the SIRIUS/IRSF catalogue of Nishiyama et al. (2006), as done for the GNS data (Nogueras-Lara et al., 2019a).

3.2.3 Proper motions

We aligned D19 with D15 data using common stars. We applied a colour cut $H - Ks > 1.3$ to remove foreground stars (see Nogueras-Lara et al., 2019a). For an estimation of the displacement and rotation angle between both data sets, we made a first alignment by finding similar 3-point asterisms with *astroalign* package in python (**?**) and a second one with a polynomial fit (*IDL polywarp*), considering two stars as the same if they were less 1 pixel apart. This procedure was iterated until the number of common stars remained stable. We computed the alignment uncertainties using a Jackknife resampling approach; we found that a polynomial of degree 2 resulted in the most accurate solution.

After aligning the lists, we compute the velocities for each star by subtracting the positions of common stars and divided them by the time baseline (~ 4 year). We computed the uncertainties quadratically propagating the errors in position for each star and the alignment uncertainty for the D19 stars. From this point on, we considered only stars with proper motions uncertainties below $2.0\,mas\,yr^{-1}$ and with an absolute magnitude difference with GNS smaller than 0.5 magnitudes (Fig. 3.3).

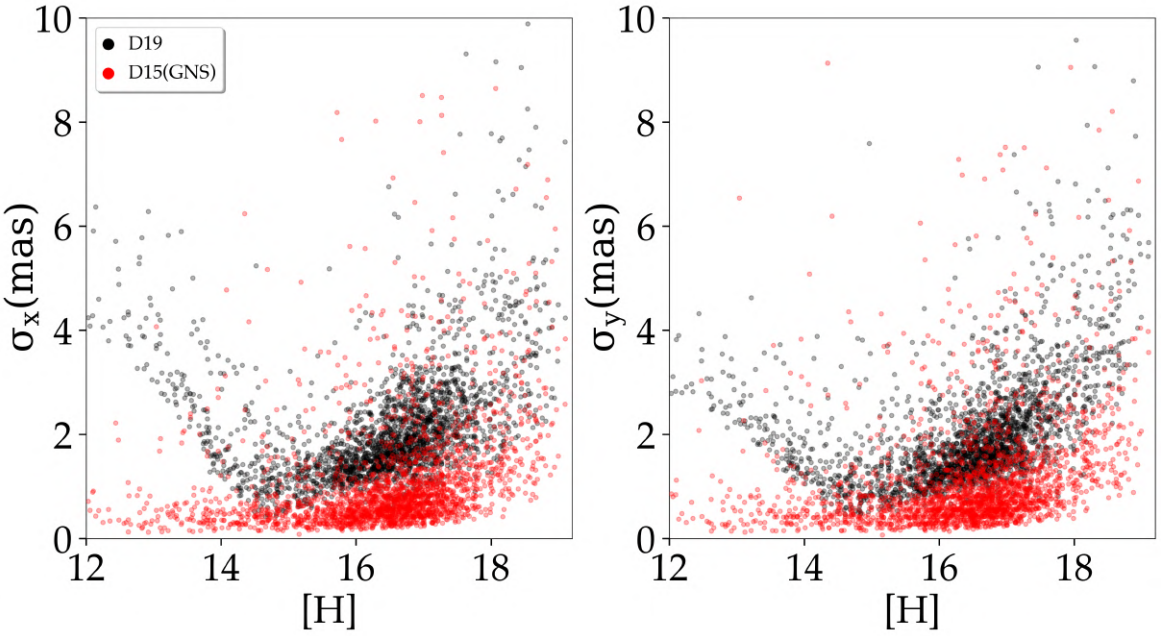

Fig. 3.2 Relative astrometric uncertainty as a function of H magnitude for all stars on the Brick and comparison fields that are common to D15(red dots) and D19 (black dots).

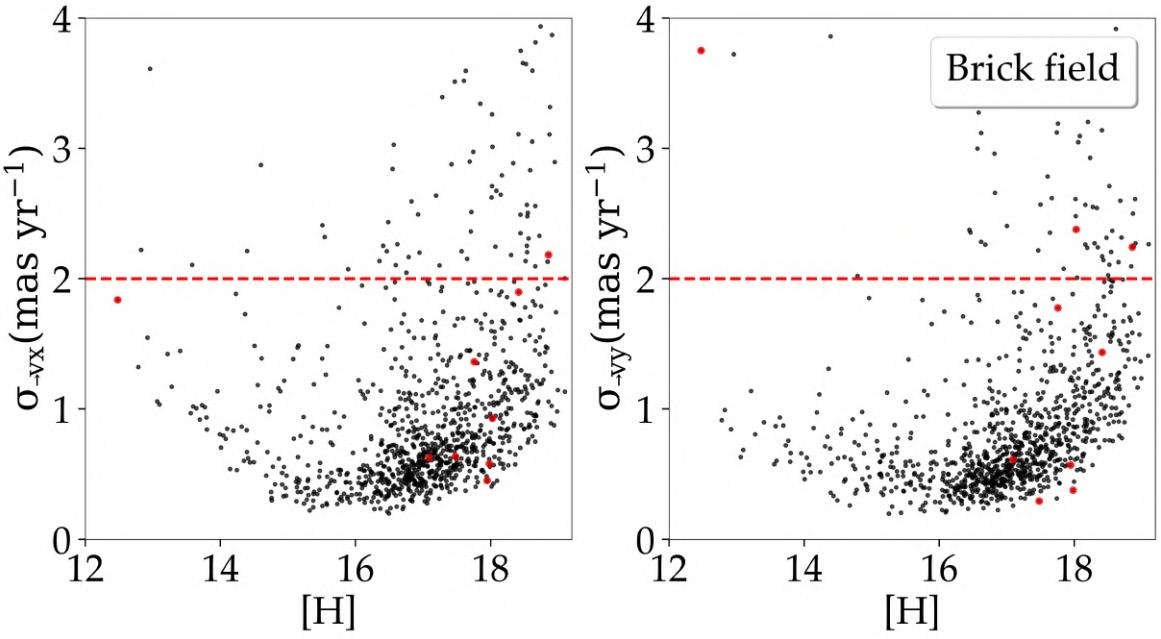

Fig. 3.3 Uncertainties for v_x and v_y as a function of H magnitude for stars with colors $H-Ks>1.3$ on the Brick field. We considered only stars with velocity uncertainties smaller than $2\,mas\,yr^{-1}$ (red dashed line). We did not consider stars with absolute difference in magnitude with GNS bigger than 0.5 (red dots). We applied the same criteria in both fields.

3.3 Results

We studied stellar kinematics on two fields: the Brick field, and the Comparison field, to galactic west of the Brick, on the NSD (Fig. 4.1).

3.3.1 Comparison field

Figure 3.4 (top left) shows the proper motions distribution perpendicular to the Galactic Plane. We computed the binning of the data with the python function *numpy.histogram_bin_edges* (Harris et al., 2020), and considered the uncertainty for the height of each bin as the square root of the number of the stars in that bin. We fitted it with different Gaussian models, using the package *dynesty* (Speagle, 2020) in python, that estimates Bayesian posterior probabilities and evidences. We try with one, two and three Gaussians models. To estimate the goodness of each fit we used the logarithm of posterior probability, $logZ$ (see Shahzamanian et al., 2022). We found that the best fit is achieved with two Gaussians. We show the best fit Gaussian model along with the proper motions distribution in Fig. 3.4 (top left) and their parameters in Tab. 3.2; uncertainties correspond to 1σ spread of each parameter posterior distribution. We interpret that the red Gaussian in Fig. 3.4 (top left), with the broader velocity dispersion, represents the stars from the Bulge, in agreement with Kunder et al. (2012) and Shahzamanian et al. (2022), and the narrow ones represents the stars from NSD.

The proper motions parallel to the Galactic Plane show a broader distribution than the ones perpendicular to the Galactic Plane (Fig. 3.4 top right), in agreement with Shahzamanian et al., 2022. We followed the procedure explained in the previous paragraph with perpendicular components. We found the best fit corresponding to a three Gaussians model. The mean Gaussians and the proper motion distribution are shown in Fig. 3.4 (top right) and their parameters in Table 3.2.

We interpret the three-Gaussians model in Fig. 3.4 (top right) as: bulge stars, with about zero proper motion, high velocity dispersion (Soto, M. et al., 2012; Shahzamanian et al., 2022); and eastward and westward moving stars on the near and far side of the NSD (Schonrich et al., 2015; Shahzamanian et al., 2022).

The lower amplitude of the Gaussian representing the westward moving stars is probably a consequence of these stars experiencing higher extinction than the eastward moving stars, since the former probably belong to the far side of the NSD. To check this, we de-reddened the stars in the comparison field using a star-by-star approach assuming that the intrinsic colour $H-Ks$ is similar for all the stars analysed (see Nogueras-Lara et al., 2021a). In Fig.3.5 we show mean Ks extinction as a function of μ_l. On average, the extinction of

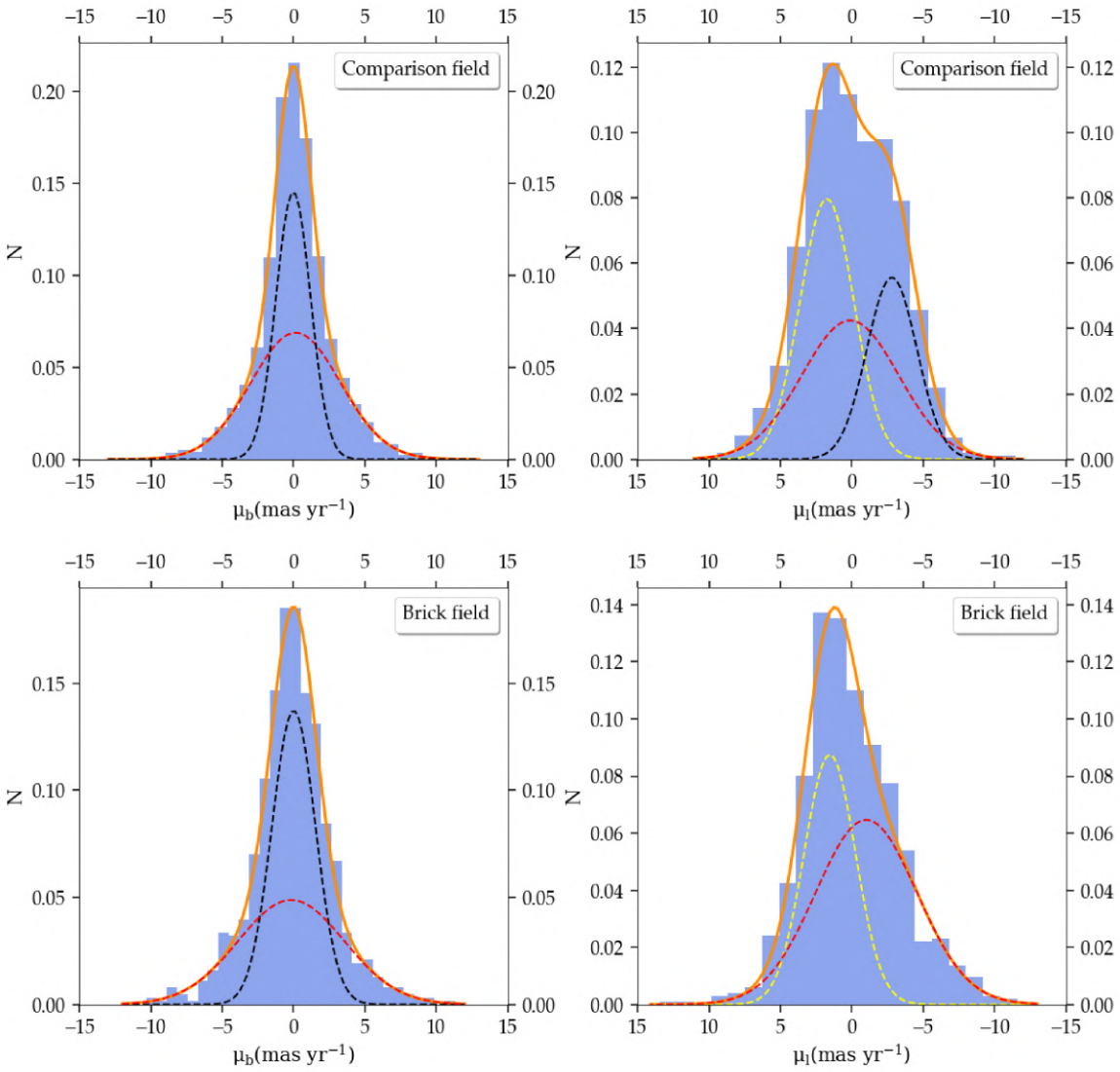

Fig. 3.4 Proper motion distribution for the comparison field (top row) and the Brick field (bottom row). Left hand plots correspond to the perpendicular component, where the red Gaussian represents the Bulge stars and the black one the NSD stars. Right hand plots correspond to the parallel component, where the red Gaussian represents the Bulge stars and the yellow and black ones the NSD stars moving eastward and westward respectively.

Table 3.2 Best-fit parameters and uncertainties for the comparison field data (Fig. 4.1)

Comparison field			
perpendicular	Bulge	NSD	-
μ_b $(mas\ yr^{-1})$	$0.15^{+0.13}_{-0.12}$	-0.02±0.08	-
σ_b $(mas\ yr^{-1})$	3.14±0.16	$1.21^{+0.10}_{-0.11}$	-
amp_b	0.54±0.06	0.44±0.06	-
parallel	Bulge	NSD	NSD
μ_l $(mas\ yr^{-1})$	$0.10^{+0.50}_{-0.49}$	$-2.77^{+0.43}_{-0.45}$	$1.76^{+0.37}_{-0.35}$
σ_l $(mas\ yr^{-1})$	$3.39^{+0.26}_{-0.24}$	$1.78^{+0.30}_{-0.29}$	$1.90^{+0.30}_{-0.31}$
amp_l	$0.35^{+0.13}_{-0.12}$	$0.25^{+0.08}_{-0.09}$	$0.38^{+0.11}_{-0.12}$

Notes: μ, σ and *amp* are the mean velocity, standard deviation and amplitude of the Gaussians fitted to the distribution. Uncertainties correspond to 1σ spread of each parameter posterior distribution. *Perpendicular* and *parallel* indicate the proper motions direction in relation with the Galactic plane.

eastward moving stars is smaller than for the westward moving stars, which justifies why we detected fewer westward moving stars (see also Fig. 10 of Shahzamanian et al., 2022).

To compute the mean proper motion values of the NSD and Bulges stars, since we do not consider an absolute frame of reference, our basic assumption is that the mean proper motion of all stars is zero. This assumption does not appear to be valid in the comparison field since we detected more stars from the near side of the NSD than from the far side, i.e, there is a net eastward proper motion present in the field. This makes our reference frame drifts eastwards and results in an underestimation of eastwards motion and an overestimation of westward motions. If we correct this by assuming the same mean eastward and westward velocities, then we see that the near and far sides of the NSD rotate with approximately 2.27 $mas\,yr^{-1}$ that, within uncertainties, agrees with measurements and theoretical expectations (Schonrich et al., 2015; Shahzamanian et al., 2022; Sormani et al., 2022).

The mean velocities ($\overline{\mu}_b$ and $\overline{\mu}_l$) and the velocities dispersion (σ_b and σ_l) for the Bulge population are in agreement with the values found in the literature (Soto, M. et al., 2012; Kunder et al., 2012; Shahzamanian et al., 2022) and also theoretical studies (Sormani et al., 2022).

3.3.2 Brick field

In the Brick field, we proceed as we did in the comparison field for the perpendicular component. Also in this case two Gaussians optimally describe the data (Fig. 3.4, bottom left

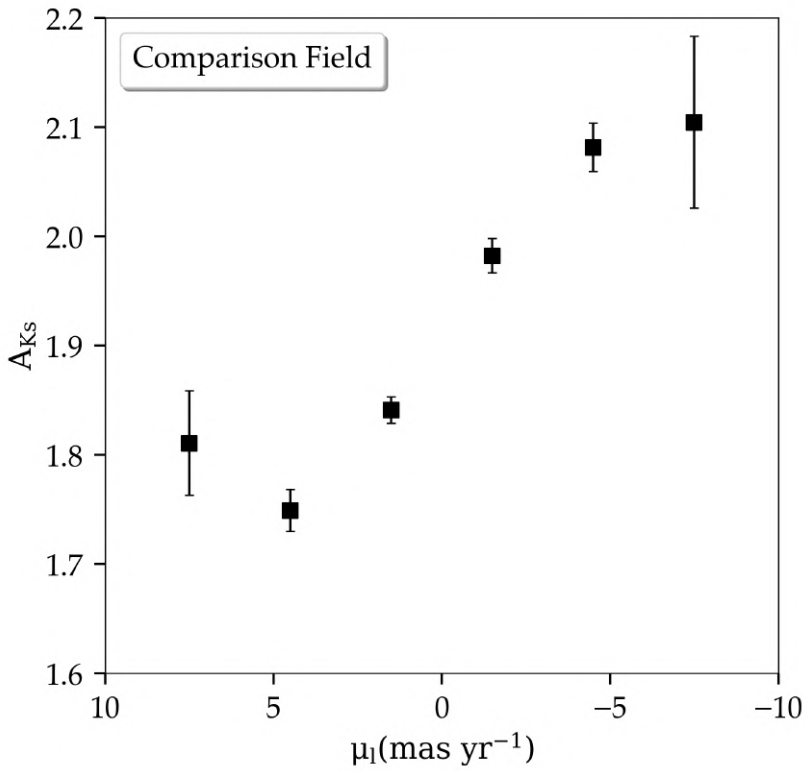

Fig. 3.5 Extinction as a function of μ_l for the comparison field. Squares and bars represent the mean extinctions and their statistical uncertainties for stars in bins of 3 $mas\ yr^{-1}$ width. Statistical uncertainties for μ_l are smaller than the width of the squares.

and Tables 3.3). These results agree with the values found for the comparison field for the perpendicular components.

For the parallel component, the 3-Gaussians model does not converge to a single solution. The best fit to the distribution corresponds to a 2-Gaussians model (Fig. 3.4 bottom row and Table 3.3). The absence of a third Gaussian in the model could mean that the mean opacity on the Brick is too high to observe stars through it, blocking the light from the stars in the far side of the NSD, which is not surprising because the Brick is an extremely dense MIR-dark cloud (Longmore et al., 2012), and agrees with the results found by Nogueras-Lara et al. (2021a); or that the number of detected sources is not big enough to affect the distribution in a significant way.

As happened in the comparison field, in this case, with no sources moving westward (or just a small number of them), the reference frame drifted eastward, and in a more pronounced way because of the extreme extinction caused by the Brick. As a consequence, the mean velocity for the Bulge Gaussian is not around zero any more and the velocity of eastward moving stars is underestimated. Since we know that the mean velocity of Bulge stars should

Table 3.3 Best-fit parameters and uncertainties for the Brick field data (Fig. 4.1)

Brick field		
perpendicular	Bulge	NSD
μ_b $(mas\ yr^{-1})$	$-0.16^{+0.25}_{-0.24}$	$-0.02^{+0.12}_{-0.11}$
σ_b $(mas\ yr^{-1})$	$3.73^{+0.18}_{-0.19}$	1.53 ± 0.12
amp_b	0.45 ± 0.06	0.53 ± 0.06
parallel	Bulge	NSD
μ_l $(mas\ yr^{-1})$	$-0.84^{+0.51}_{-0.52}$	$1.57^{+0.33}_{-0.31}$
σ_l $(mas\ yr^{-1})$	$3.44^{+0.19}_{-0.21}$	$1.81^{+0.40}_{-0.43}$
amp_l	$0.59^{+0.14}_{-0.15}$	$0.38^{+0.16}_{-0.15}$

Notes: μ, σ and *amp* are the mean velocity, standard deviation and amplitude of the Gaussians fitted to the distribution. Uncertainties correspond to 1σ spread of each parameter posterior distribution. *Perpendicular* and *parallel* indicate the proper motions direction in relation with the Galactic plane.

be around zero, we can compensate the drifting effect by requiring that the mean motion of the Bulge stars is zero. That leaves us with a mean velocity for the parallel component of the NSD of $\mu_{east} = 1.57 + 0.84 = 2.41\ mas\ yr^{-1}$. This value agrees, within the uncertainties, with our results in the comparison field and with the rotation velocities for the disk found by Shahzamanian et al. (2022) and Schonrich et al. (2015).

3.4 Conclusions

We analyzed the stellar kinematics for two different regions, one on the dense molecular cloud G0.253+0.016 (the Brick) and another on a Comparison field westward from it, delimited with blue and green on Fig. 4.1. We found that, in both cases, the models that best describe the parallel and perpendicular components of the proper motion distributions are compatible with the presence of two different populations.

On the comparison field, for the perpendicular component of the velocity, we can optimally fit the proper motion distribution with two Gaussians (Fig. 3.4 top left) representing Bulge and NSD population. We interpret the broader Gaussian as characterizing the stars from the Bulge and the narrow one corresponding to the population of the NSD. Three Gaussians optimally describes the proper motion distribution for the parallel component: 1) corresponding to the Bulge population and 2) and 3) to the NSD population, moving eastward and westward respectively (Fig. 3.4 top right). On the Brick field, as happened on comparison field, we clearly identify two different populations; represented with two Gaussians for the

perpendicular component (Fig. 3.4 bottom left) and, because extinction, also two Gaussians for the parallel (Fig. 3.4 bottom right).

The velocity dispersion values for the Bulge populations in both fields are in agreement with the ones found by Soto, M. et al. (2012), Kunder et al. (2012) and Shahzamanian et al. (2022). With respect to the parallel component, the values obtained in both fields are compatible with each other and also with the rotation velocity for the NSD found by Schonrich et al. (2015) and Shahzamanian et al. (2022).

If the Brick were located at a distance from the Sun of ~ 7.20 kpc as claimed by Zoccali et al. (2021), it would be placed well outside the NSD, but still inside the Bulge; consequently, we would not expect to find traces of two different populations in the distribution, but only of one. Instead, we can clearly distinguish two different populations; furthermore, the parameters of these distributions are in agreement with those found by other authors for the NSD and Bulge populations. These are strong indicators suggesting that the Brick is embedded in the NSD and the CMZ, hence, located at the Galactic center.

This conclusion is supported by different arguments in other studies. For example, the turbulent velocity dispersion found for the gas in the Brick cloud does not match that found in other molecular clouds in the Galactic plane, which are significantly lower (see e.g. Henshaw et al., 2016, 2019).

Acknowledgments

We acknowledge financial support from the State Agency for Research of the Spanish MCIU through the "Center of Excellence Severo Ochoa" award for the Instituto de Astrofísica de Andalucía (SEV-2017-0709).
We acknowledge financial support from national project PGC2018-095049-B-C21 (MCIU/AEI/FEDER, UE).
FN-L gratefully acknowledges support by the Deutsche Forschungsgemeinschaft (DFG, German Research Foundation) – Project-ID 138713538 – SFB 881 ("The Milky Way System", subproject B8), and the sponsorship provided by the Federal Ministry for Education and Research of Germany through the Alexander von Humboldt Foundation.

Chapter 4

Co-moving groups in the nuclear stellar disk

This chapter contains the literal transcript of the published article, *Co-moving groups around massive stars in the nuclear stellar disk* (Martínez-Arranz et al., 2024a). The article highlights significant progress in several areas. Firstly, it introduces innovative methodologies and tools designed specifically for identifying co-moving groups within the GC. Additionally, it reports the discovery of three potential young stellar clusters or associations located within the NSD. Furthermore, the article describes the implementation of techniques aimed at eliminating false-positive co-moving groups within the GC, ensuring the accuracy of the findings. Additionally, it discusses the validation of the structure and rotational velocity of the NSD through the analysis of stellar kinematics.

Co-moving groups around massive stars in the nuclear stellar disk

Á. Martínez Arranz[1], R. Schödel[1], F. Nogueras-Lara[2], M. W. Hosek Jr.[3], and F. Najarro[4]

[1]*Instituto de Astrofísica de Andalucía (CSIC), University of Granada, Glorieta de la astronomía s/n, 18008 Granada, Spain*

[2]*Max-Planck Institute for Astronomy, Königstuhl 17, 69117 Heidelberg, Germany*

[3]*University of California, Los Angeles, Department of Astronomy, Los Angeles, CA 90095, USA*

[4]*Centro de Astrobiología (CSIC/INTA), ctra. de Ajalvir km. 4, 28850 Torrejón de Ardoz, Madrid, Spain*

Astronomy and Astrophysics: Galactic structure, stellar clusters and populations. V683, A13

DOI: 10.1051/0004-6361/202347937

Abstract

Over the last $\sim$ 30 Myr, the nuclear stellar disk in the Galactic center has been the most prolific star-forming region of the Milky Way when averaged by volume. Remarkably, the combined mass of the only three clusters present today in the nuclear stellar disk adds up to only $\sim$10% of the total expected mass of young stars formed in this period. Several causes could explain this apparent absence of clusters and stellar associations. The stellar density in the area is so high that only the most massive clusters would be detectable against the dense background of stars. The extreme tidal forces reigning in the Galactic center could dissolve even the most massive of the clusters in just a few megayears. Close encounters with one of the massive molecular clouds, which are abundant in the nuclear stellar disk, can also rapidly make any massive cluster or stellar association dissolve beyond recognition. However, traces of some dissolving young clusters and associations could still be detectable as co-moving groups.

It is our aim to identify so far unknown clusters or groups of young stars in the Galactic center. We focus our search on known, spectroscopically identified massive young stars to see whether their presence can pinpoint such structures.

We created an algorithm to detect over-densities in the 5D space spanned by proper motions, positions on the plane of the sky, and line-of-sight distances, using reddening as a proxy for the distances. Since co-moving groups must be young in this environment, proper motions provide a good means to search for young stars in the Galactic center. As such, we combined publicly available data from three different surveys of the Galactic center, covering an area of $\sim$ 160 arcmin^2 on the nuclear stellar disk.

We find four co-moving groups around massive stars, two of which are very close in position and velocity to the Arches' most likely orbit.

These co-moving groups are strong candidates to be clusters or associations of recently formed stars, showing that not all the apparently isolated massive stars are run-away former members of any of the three known clusters in the Galactic center or simply isolated massive stars. Our simulations show that these groups or clusters may dissolve beyond our limits of detection in less than $\sim$6 Myr.

4.1 Introduction

Located around the Galactic center (GC), 8.2 kpc away from Earth (GRAVITY Collaboration et al., 2020), we find the nuclear stellar disk (NSD), a flat-rotating structure (Schonrich et al., 2015; Shahzamanian et al., 2022) of $\sim$200 pc across and $\sim$50 pc scale height (Launhardt

et al., 2002; Gallego-Cano et al., 2020). The NSD is an old structure, with most of its stellar population at least ~ 8 Gyr old (Nogueras-Lara et al., 2020).

The NSD constitutes an extreme environment marked by intense tidal forces, elevated stellar density, and exceptionally strong magnetic fields. Despite these challenging conditions, the NSD emits approximately 10% of the total Lyman continuum flux in the entire Milky Way, while occupying less than 1% of the galaxy's volume (Morris and Serabyn, 1996; Launhardt et al., 2002; Nishiyama et al., 2008). Recent studies suggest that intense star-forming activity occurred in the NSD between about 0.1 and 30 Myr ago, reaching a star-forming rate of about 0.1 $M_\odot$ per year in this period (Matsunaga et al., 2011; Nogueras-Lara et al., 2020). This would correspond to more than 1 million solar masses of young stars. While such intensive star formation left clear signs in the form of massive stellar clusters and associations in the Milky Way's disk, the evidence for recent star formation in the NSD is more indirect. For example, there are only two known massive young clusters, the Arches and Quintuplet clusters (both at projected distance of about 25 pc from Sagittarius A*), and one association of young, massive stars in the central parsec (Bartko et al., 2010; Lu et al., 2013). They formed between 2 and 6 Myr ago and are about $1 \times 10^4\,M_\odot$ each. In addition, a few dozen massive young stars have been detected distributed throughout the central 100 pc (e.g., Clark et al., 2021; Cano-González et al., 2021; Clark et al., 2023). Finally, on the order of $1 \times 10^5\,M_\odot$ of young stars of age $\sim$10 Myr have been reported in the Sgr B1 HII region (Nogueras-Lara et al., 2022b). Together, all these stars still make up only a fraction of the stars that formed in the past few tens of megayears, which begs the question of where the "missing" young stars are.

This absence of direct observations of the products of star formation is due to the peculiar characteristics of the GC region. On the one hand, the stellar surface density is extremely high, which makes it hard or even impossible to detect any but the most massive clusters in the form of local stellar over-densities.

On the other hand, extreme interstellar extinction and its variability on small angular scales means that young hot stars cannot be easily distinguished photometrically from cool, old giants (see Schoedel et al., 2014; Cano-González et al., 2021). The extreme and differential extinction in the GC (e.g., Nishiyama et al., 2009; Nogueras-Lara et al., 2019b) limits observations to the near-infrared wavelength range, where it is impossible to identify young clusters in color-magnitude diagrams (CMDs), which are highly affected by the reddening (Nogueras-Lara et al., 2018).

Also, strong tidal forces in the GC will dissolve a cluster as massive as the Arches in $\lesssim 10$ Myr (Portegies Zwart et al., 2001; Kruijssen et al., 2014), blending it with the background population. Spectroscopy needs to be performed at high angular resolution,

which implies a very small field of view. Therefore, conducting spectroscopic searches is not a practical option due to the extensive time required to sample the entire region. However some clusters and stellar associations could still be detectable as co-moving groups, which is a detection method that has hardly been explored so far (with the exception of Shahzamanian et al. 2019).

Several studies have shown how stellar kinematics can unveil different kinds of structures, such as open clusters in *Gaia* data (Castro-Ginard et al., 2018) or substructures in the Galactic plane of the Milky Way (Laporte et al., 2022). In the GC, stellar proper motions have previously been used to study the structure of the NSD (see for example Shahzamanian et al. 2022; Martínez-Arranz et al. 2022; Nogueras-Lara 2022). Membership probabilities and orbits for the Arches and Quintuplet clusters have also been derived using proper motion analysis (Hosek et al., 2022).

We have created a new method for revealing co-moving groups in the highly crowded environment of the GC. This tool is based on the Density-Based Spatial Clustering of Applications with Noise (DBSCAN) algorithm (Ester et al., 1996), and a similar version of it has previously been used by Castro-Ginard et al. (2018) to detect open clusters in *Gaia* Data Release 2 (DR2). In this case, we looked for over-densities in a 5D parameter space. In this paper we present four co-moving groups in the GC associated with four different massive stars (Fig. 4.1) identified by Clark et al. (2021).

4.2 Data

We used proper motion data from the catalog by Libralato et al. (2021b) (from now on L21) acquired with the *Hubble* Space Telescope (HST) Wide-Field Camera 3 (WFC3), combined with photometric data from the GALACTICNUCLEUS catalog (Nogueras-Lara et al., 2018, 2019a) acquired with the Very Large Telescope's High Acuity Wide-field K-band Imager (HAWKI) instrument. In order to test the cluster search algorithm we used proper motion catalogs for the Arches and the Quintuplet clusters by Hosek et al. (2022) and extinction maps and catalogs in the H and Ks band by Nogueras-Lara et al. (2021a).

4.2.1 Proper motions

The catalog of L21 was produced based on two sets of observations covering the area inside the white boxes in Fig. 4.1. They were acquired with the near-infrared channel of the Wide-Field Camera 3, mounted on the HST, in October 2012 and August 2015. The proper motions were calibrated using reference stars for *Gaia* DR2 (Gaia Collaboration et al., 2016). More

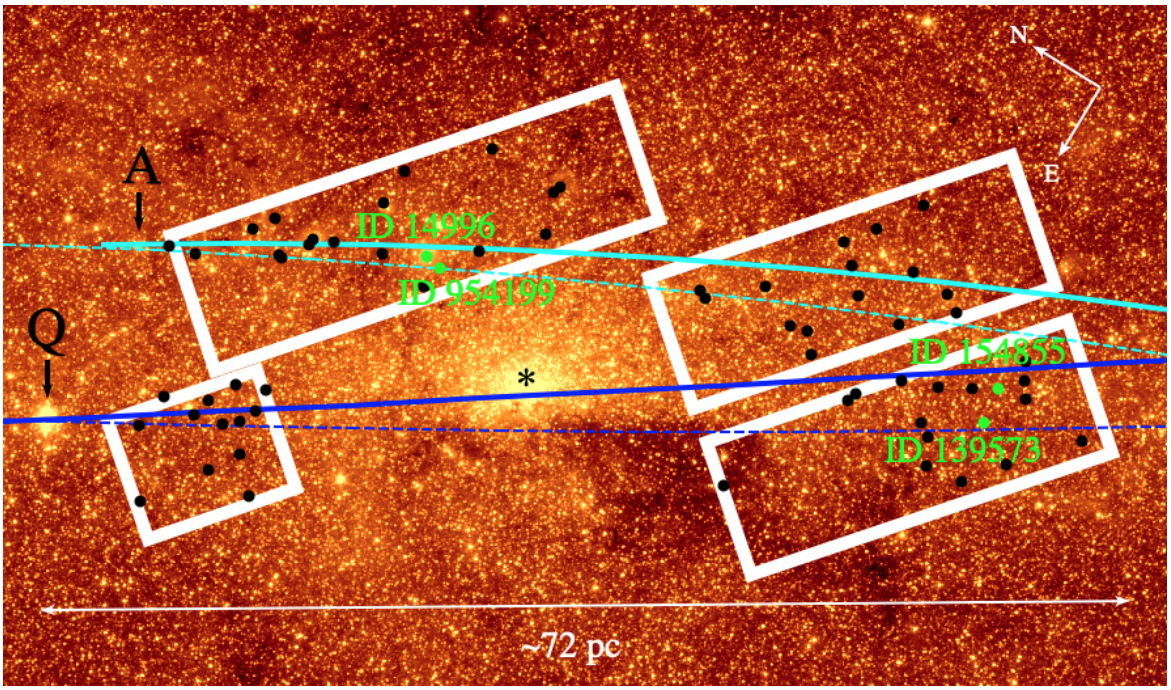

Fig. 4.1 Survey coverage, cluster orbits, and massive star distribution in the GC. Regions covered by Libralato et al. (2021b) (indicated by white boxes) are superimposed on a 4.5 μm *Spitzer*/IRAC image (Stolovy et al., 2006). The cyan and blue lines represent the most probable prograde orbits of the Arches and Quintuplet clusters, respectively, as determined by Hosek et al. (2022). The continuous line indicates movement toward the Galactic east (in front of the plane of the sky), while the dashed line indicates movement toward the Galactic west (behind the plane of the sky). The plotted points correspond to massive stars identified by Clark et al. (2021) for which proper motion data are available. Among these stars, the green points are associated with a co-moving group, and their ID numbers correspond to their index as listed in Libralato et al. (2021b). The letters A and Q and the asterisk denote the positions of the Arches and Quintuplet clusters and SgrA*.

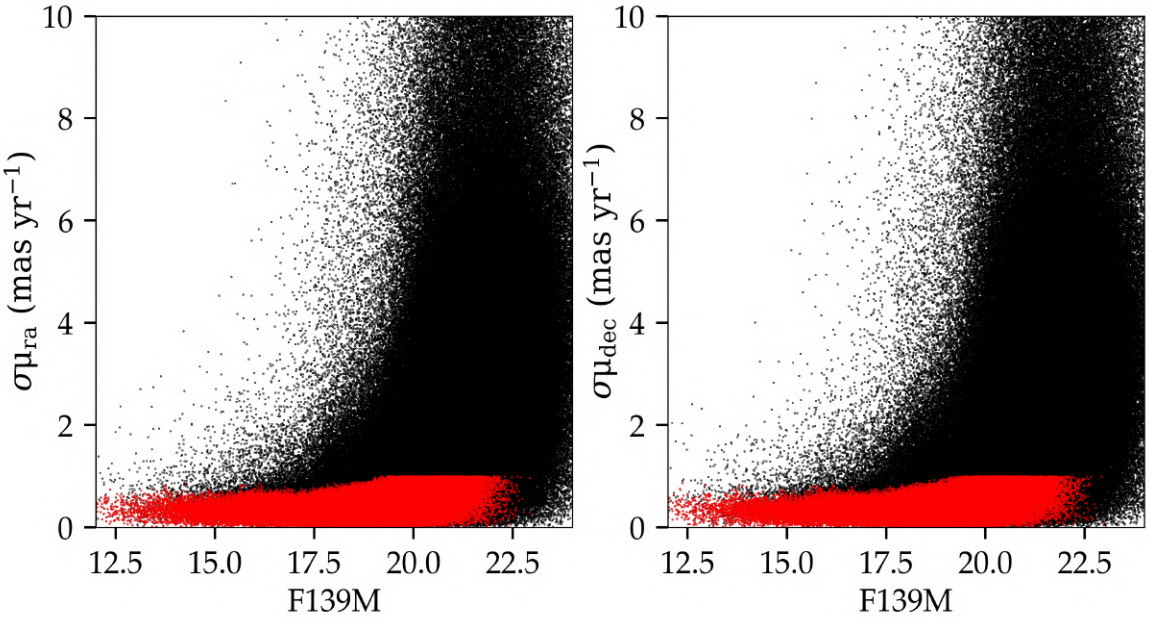

Fig. 4.2 Proper motion error versus magnitude in L21. Proper motion error in right ascension (left) and declination (right) versus F139M magnitude for the whole proper motion catalog (black) and the trimmed data (red).

details about the acquisition, reduction, and analysis of the data are available in L21.[1] The final catalog consists of absolute proper motion measurements for $\sim$ 830.000 stars, which we trimmed in a similar way as done by Libralato et al. (2021b), namely: we excluded stars with proper motions faster than 70 mas /yr, we selected only stars with proper motion errors lower than the 85th percentile in bins of 0.1 mag width and, finally, we discarded stars with proper motion error bigger than 1 mas /yr (Fig. 4.2).

We cross-referenced the catalog with the GALACTICNUCLEUS survey (Nogueras-Lara et al., 2018, 2019a) to assign H and Ks magnitudes to the members of L21. GALACTICNUCLEUS was specifically designed to observe the GC, providing highly accurate point spread function photometry for over three million stars in the NSD and the innermost Galactic bar. The photometric uncertainties are remarkably low, remaining below 0.05 magnitudes at H$\sim$ 19 mag and Ks $\sim$ 18 mag. Once we obtained H and Ks magnitude values for the L21 members, we employed a color cut H$-$Ks $>$ 1.3 to remove the foreground population.

To assess the data quality, we extracted the mean velocity values for various components of the NSD and bulge from L21 and compared them with values reported in the literature. Further information about this process can be found in Appendix 4.A.

[1]The proper motions catalogs are available at https://academic.oup.com/mnras/article/500/3/3213/5960177

4.3 Methods

We assumed that a stellar group would belong to the same cluster or stellar association if its members are close together in space and have similar velocities. It would be defined by a 6D parameter space, three dimensions for the components of the velocities and three for the components of the position. We only have data for proper motions and positions in the plane of the sky, but we can indirectly constrain the third dimension in position: the line-of-sight distance. Considering the considerable variation in extinction along the line of sight in the GC (e.g., Nishiyama et al., 2009; Nogueras-Lara et al., 2018), and the relatively constant intrinsic colors of the observable stars (they vary by not more than a few 0.01 mag; see for example Fig. 33 in Nogueras-Lara et al., 2018), we hypothesize that changes in color are mainly influenced by extinction (see also Nogueras-Lara et al., 2021a). Therefore, if a group of stars shares similar colors, it is likely that they are located at a similar depth within the NSD (Nogueras-Lara, 2022). We searched the data looking for over-densities in the 5D space formed by proper motions along the RA and Dec directions, coordinates in the plane of the sky, and color.

4.3.1 The algorithm

We developed a tool for detecting co-moving groups in the GC based on DBSCAN (Ester et al., 1996; Sander et al., 1998; Schubert et al., 2017). DBSCAN requires two input parameters: ε and N_{min}. The parameter ε establishes the distance within which the algorithm scans for nearby points around a specific data point. N_{min} specifies the minimum number of points that should be within the ε radius to form a dense region. Considering these two parameters DBSCAN classifies each point in one of these 3 categories: Core point, if the number of points around it within a radius of ε is $\geq N_{min}$. Border Point, if it is not a core point, but it is within an ε distance of one, and Noise, if it is neither a core point nor a border point. The algorithm will iterate until all points are labeled with one of these categories. Core and border points are considered cluster members. As there is no preferred dimension in the 5D parameter space, we standardized the parameters. This means they have a mean of zero and a variance of one, ensuring that their contributions to the clustering process are balanced.

The conditions present in the NSD, where the stellar densities vary greatly on scales of a few arcseconds due to the high and patchy extinction (Nogueras-Lara et al., 2021a) and the high densities of stars (Nogueras-Lara et al., 2019a), make the selection of ε particularly challenging. If we choose a value that is too small, the required minimum number of sources within a distance epsilon will never be fulfilled and no cluster will be found. On the other

hand, if we choose a value that is too large, then spurious clusters present in the data just by chance will be detected because of statistical fluctuations.

In order to find an appropriate value for ε, we assumed that if there is a cluster in a particular dataset, then the distances among its members will be smaller, on average, than the distances between any other group of points in the same dataset. So, for each run of the algorithm we computed the distances to the k^{th} nearest neighbor (k-NN) in the 5D space for all the stars in the area of analysis. Then, we generated a random sample with the same number of stars. To achieve this, we utilized the Gaussian kernel density estimator, specifically the gaussian_kde function from Scipy (Virtanen et al., 2020), to estimate the distribution of each astrometric parameter from the original dataset. We sampled from the estimated distributions to create a simulated population. Subsequently, we computed the k-NN distances for the simulated population. Since these populations are randomly generated, any existing clusters present in the original data are effectively destroyed in the simulated population. To mitigate the inherent variability resulting from the random generation of simulations, we performed 20 different simulations and calculated the average values. This approach allowed us to minimize the impact of slight differences between individual simulations.

If there were any cluster in the real data, then the minimum of the k-NN distances in the real data would be smaller than the minimum of the simulated data with no cluster in it. Next, we chose the value for ε as the mean between both minima, the real and the simulated one[2]. By choosing an epsilon smaller than the minimum neighbor distance for the simulated data, we tried to avoid any association of points that could show up in the data just by chance.

4.3.2 Testing the algorithm

To test our clustering tool, we used data from (Hosek et al., 2022, H22 hereafter). They consist of astro-photometry data (equatorial coordinates, proper motions and magnitudes in F127M and F153M filters) acquired with the WFC3/HST camera in the areas of the Arches and Quintuplet clusters.

In H22, membership probabilities for the Arches and Quintuplet clusters are assigned, considering stars as cluster members if their membership probability is greater than 0.7. The membership probability assigned to each star by this work is based on the proper motions of the stars in an area of approximately 4 arcmin^2 around each cluster. For further insight into the probability assignment process, refer to Appendix B in Hosek et al. (2022). Figure 4.B.1

[2]A similar method for constraining the value of ε was used by Castro-Ginard et al. (2018).

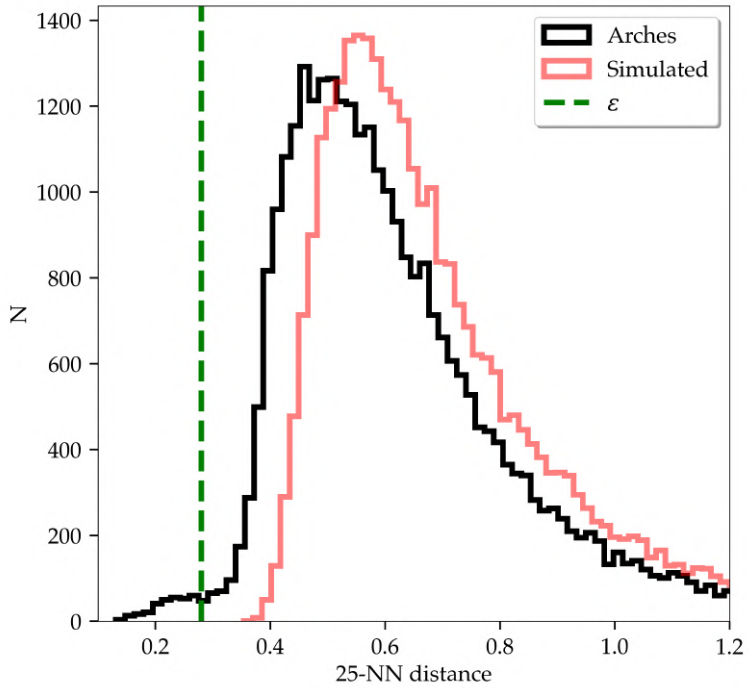

Fig. 4.3 NN distance analysis: Arches versus simulated data. The black histogram represents the distance of each point, in 5D space, to its 25-NN for the Arches data in H22. The red one is for the simulated data with no cluster. The green line marks the chosen value for epsilon in this particular case.

displays the stars identified as belonging to the Arches and Quintuplet clusters based on this criterion.

In the following, we describe the processes we undertook, using the data for the Arches cluster in H22 as an example. First, we chose a starting value. For this example we chose $N_{min} = 25$. We tried our algorithm with different values of N_{min}. We found that using any value of N_{min} between 20 and 35 with H22 data returned similar values for proper motions and velocity dispersion as those found in H22 for both the Arches and Quintuplet datasets. Then we computed the 25-NN distance in a 5D space; velocity, position and color (black histogram in Fig. 4.3). Then we randomly generated a simulated population following the procedure described above, thus eliminating any real cluster from the data, and calculated the 25-NN distance for the simulated data (red histogram in Fig. 4.3). We can see that the real set of data, which we know has a cluster in it, has smaller minimum 25-NN distances than the set of simulated data with no real cluster in it. These lower values correspond to the points that are closest in the 5D space. Then we selected our ε as the mean value between

the minimum of the real data and the minimum of the simulated data (green dashed line in Fig. 4.3).

Next we ran the algorithm on the Arches dataset of H22 with the ε and N_{min} parameters that were set in the previous step. In Fig. 4.4 top row, we can see in orange the points labeled as cluster members that were returned by our algorithm. We repeated the process with the Quintuplet dataset (bottom row in Fig. 4.4). The mean values and their standard deviations for the proper motions that we obtain in each case are $(\mu_{*ra}, \mu_{dec})^{Arches} = -0.85 \pm 0.23$, -1.89 ± 0.24 mas/yr, and $(\mu_{*ra}, \mu_{dec})^{Quintuplet} = -0.97 \pm 0.19$, -2.29 ± 0.22 mas/yr (left panels in Fig. 4.4). The values of the mean proper motions in both cases are similar to the ones obtained by Hosek et al. (2022): $(\mu_{*ra}, \mu_{dec})^{ArchesH22} = -0.80$, -1.89 mas/yr, and $(\mu_{*ra}, \mu_{dec})^{QuintupletH22} = -0.96$, -2.29 mas/yr. The velocity dispersions we obtained for both clusters, $\sigma \sim 0.2$ mas/yr, are comparable with the velocity dispersion found in other studies (Stolte et al., 2008, 2014; Clarkson et al., 2012). We computed the half-light radii of both clusters by transforming the magnitudes into fluxes using the python package species (Stolker et al., 2020). These values are displayed in the orange boxes in the central plot of Fig. 4.4. The ratio between these radii, approximately 2, aligns with the values reported in the literature for the half-light radius of the Arches cluster (12.5 arcsec; Hosek et al., 2015) and the Quintuplet cluster (25 arcsec) (Rui et al., 2019). The smaller half-light radii values we obtained may indicate the detection limit of our algorithm, which appears to be less sensitive to the outer members of the clusters. When comparing the stars identified as members of the Arches and Quintuplet clusters by our algorithm with those that H22 considered as likely members of the clusters (with membership probabilities $p \geq 0.7$), we observe a level of completeness of approximately 42% for the Arches and approximately 31% for the Quintuplet. This represents approximately 45% of contamination in the Arches cluster and around 35% in the Quintuplet cluster found by our algorithm. These differences arise from restrictions in the parameter space of our algorithm. While the algorithm is configured to search for clusters in the 5D space, it also considers proximity in the parameter space defined by RA and Dec coordinates as a requirement for a star to be considered a cluster member. Consequently, stars farther away from the cluster core, which are likely members according to Hosek et al. (2022), are labeled as noise due to this criterion (see our Fig. 4.B.1, top row). If we relax the restrictions of the algorithm and search only in the parametric space of velocities, the completeness level for the Arches and Quintuplet clusters with respect to those selected by H22 increases to 82% and 85%, respectively (Fig. 4.B.1, bottom row). This represents 25% contamination in the Arches cluster and 15% for the Quintuplet found by the algorithm. However, it is important to note that due to the extreme crowding in the NSD and the fact that clusters as dense as the Arches or the Quintuplet are not expected to be found

in the area, conducting a search for clusters or stellar associations using this configuration, which focuses solely on proximity in the velocity space, is not practical in the GC.

We compared the Arches catalog calculated by (Clark et al., 2018a, hereafter C18) with the members identified in Hosek et al. (2022) (see Fig. 4.B.1 top row, left plots) and those selected by our algorithm using the 5D configuration (top row of Fig. 4.4). We display the matched positions in the top row of Fig. 4.5. The C18 catalog comprises 194 stars, including confirmed and candidate Arches members. The matches between H22 and C18 are approximately 50% of C18. In comparison, the percentage of matches with the algorithm-selected members is around 70% of C18. This may indicate that the algorithm in its 5D configuration is effective at identifying members at the core of the clusters. In the bottom row of Fig. 4.5 , we present histograms of magnitude residuals for these matches. Given that the photometry in H22 and C18 originates from distinct catalogs, the low residual values with a mean of $\overline{\Delta F153M} \sim 0.016$, indicate non-spurious matches.

The Arches cluster experiences a significant variation in extinction, as discussed in the study by Hosek et al. (2015). This is evident in the broader distribution observed in the CMD of the stars identified as Arches members (Fig. 4.4).

We ran a second test where we inserted the recovered Arches cluster, as determined by the algorithm in its 5D configuration, maintaining its original properties (see Fig. 4.4, top row) into a simulated population of stars. We then ran the cluster algorithm on this simulated population, which included the cluster. This simulated population consisted of the same objects as those in L21, but we shuffled the velocities of the stars while maintaining their positions. This velocity shuffling eliminated any possible substructure present in the catalog. Additionally, we excluded areas with the presence of dark clouds from the simulated population (see Fig. 3 in Nogueras-Lara et al., 2021a). We first crossmatched the data from H22 with the GALACTICNUCLEUS catalog (Nogueras-Lara et al., 2018, 2019a) in order to assign H and Ks magnitudes to the stars, in the same way as we did with L21. Since the extinction is not homogeneous across the NSD, we had to correct the color of the cluster stars according to the value of extinction at the place where the stars will be inserted. For this purpose we used the extinction maps in H and Ks from Nogueras-Lara et al. (2021a). We inserted and recovered the model cluster 50 times, placing it in random positions across the simulated population on each occasion. The first and second rows in Table 4.1 show the mean motions and their dispersions for the inserted and for the recovered clusters. The last two columns of the table show the percentage of recovered stars and the percentage of contaminating stars that the recovered cluster contained. We recovered on average more than 80% of the original stars with less than 20% of contamination from other stars. The difference in μ_{*ra} and μ_{dec} between inserted and recovered cluster is $\sim 2\%$

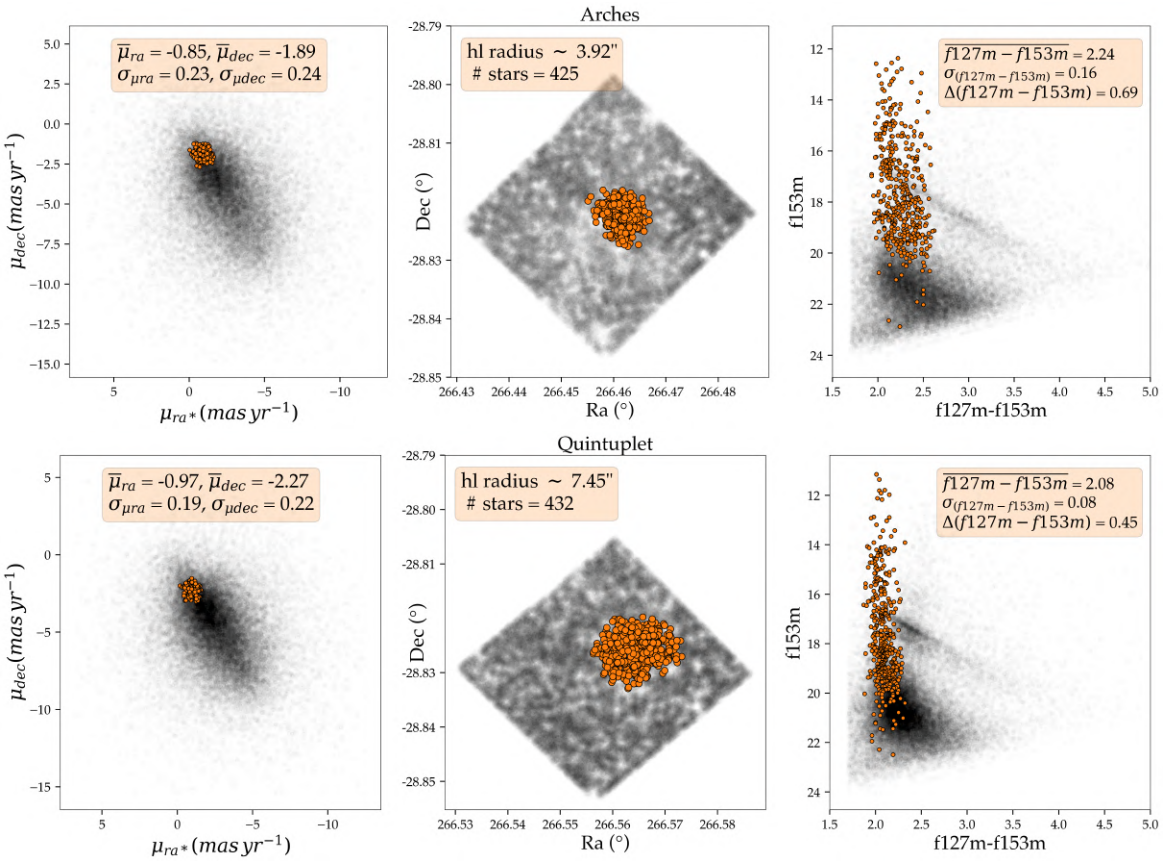

Fig. 4.4 Arches cluster (upper row) and Quintuplet cluster (lower row) as recovered by the algorithm in its 5D configuration. Left column: Vector-point diagram. Middle column: Stellar positions. Right column: CMD. Orange points represent the objects labeled as cluster members. Black points represent objects that are not labeled as cluster members.

Finally, in order to test the detection limit of the cluster algorithm, we repeated the experiment but this time we inserted less dense clusters. In order to simulate them, we used as models the recovered cluster parameters for Arches and Quintuplet from the H22 data (Fig. 4.4). Since the masses of both clusters are comparable, $\sim 10^4 M_\odot$ (Clarkson et al., 2012; Harfst et al., 2010) and they are in a similar environment, we assumed that they will evolve in a similar way. We used Quintuplet, with an age of ∼4 Myr (Figer et al., 1999a; Liermann et al., 2012; Clark et al., 2018b) as a model for the evolutionary path that the younger Arches, ∼2.5 Myr (Figer et al., 1999a; Najarro et al., 2004; Espinoza et al., 2009), would follow. By doing so, we could approximate the growth rate of the Arches cluster, assuming that its half-light radius will be similar to that of the Quintuplet in about 1.5 Myr. Next, we moved the Arches stars along the direction of their individual proper motion vectors, assuming this growth rate as constant over time. Then, we evolved the Arches cluster at different time lengths.

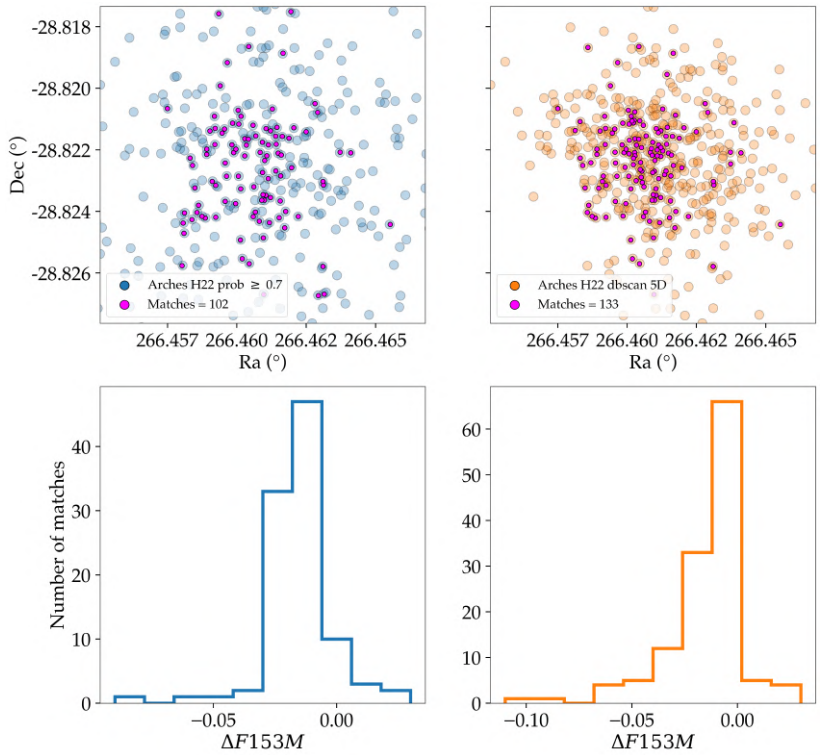

Fig. 4.5 Arches members: H22 versus 5D algorithm. Top row: Arches members according to H22 (blue points), those selected by the algorithm in the 5D configuration (orange points), and the matches with the Arches members considered in C18 for each case (fuchsia points). Bottom row: Magnitude residuals for the matches.

We inserted each of these models into the L21 data as we did before with the non-evolved models, and then ran our algorithm to recover them. This process was repeated 50 times for each model. The statistics for some of these simulations are presented in Table 4.1. Given that the environment changes with each insertion, the table displays the average and standard deviation for the 50 insertions. We defined the detection limit of our algorithm when the percentage of model stars recovered by the algorithm became lower than the percentage of contaminating stars in the recovered cluster (last two columns in Table 4.1). We can see that this limit is reached when our Arches model evolved ~ 3.3 Myr. Based on this analysis, the detection of a hypothetical cluster as massive as the Arches, which has evolved over 6 million years since its formation, would exceed our detection limits: more than 50% of the members of this cluster would probably be contamination. This detection limit is comparable with theoretical predictions of the time it would take for a massive cluster to dissolve in the GC (Portegies Zwart et al., 2001; Kruijssen et al., 2014).

Table 4.1 Cluster recovering simulations.

Cluster	μ_{ra} (mas/yr)	μ_{dec} (mas/yr)	$\sigma_{\mu ra}$ (mas/yr)	$\sigma_{\mu dec}$ (mas/yr)	R(arcsec)	% recov.	% contam.
Model 0.0 Myr	-0.83	-1.78	0.22	0.25	22	-	-
Recovered	-0.84±0.01	-1.81±0.02	0.32±0.04	0.34±0.04	39±4	85±6	17±6
Model 0.6 Myr	-0.79	-1.71	0.22	0.27	22	-	-
Recovered	-0.81±0.01	-1.74±0.01	0.32±0.04	0.35±0.04	39±4	84±6	16±6
Model 1.5 Myr	-0.81	-1.69	0.22	0.28	43	-	-
Recovered	-0.83±0.06	-1.77±0.11	0.33±0.07	0.36±0.14	43±4	80±11	19±11
Model 2.1 Myr	-0.70	-1.73	0.24	0.27	69	-	-
Recovered	-0.73±0.02	-1.80±0.03	0.34±0.06	0.34±0.08	50±3	78±5	21±9
Model 3.0 Myr	-0.74	-1.69	0.23	0.28	122	-	-
Recovered	-0.79±0.07	-1.84±0.12	0.39±0.12	0.43±0.19	63±6	61±11	32±15
Model 3.3 Myr	-0.68	-1.62	0.24	0.31	152	-	-
Recovered	-0.83±0.19	-1.92±0.25	0.51±0.19	0.60±0.29	73±13	57±8	43±18
Model 3.6 Myr	-0.72	-1.51	0.23	0.37	191	-	-
Recovered	-0.95±0.23	-1.98±0.34	0.61±0.23	0.73±0.33	82±16	50±10	52±20
Model 3.9 Myr	-0.79	-1.57	0.22	0.34	228	-	-
Recovered	-1.13±0.29	-2.29±0.44	0.76±0.27	0.96±0.38	93±23	43±12	65±21
Model 4.5 Myr	-0.83	-1.51	0.22	0.37	322	-	-
Recovered	-1.28±0.32	-2.53±0.48	0.89±0.28	1.11±0.38	97±29	28±11	76±20
Model 5.1 Myr	-0.93	-1.61	0.24	0.32	416	-	-
Recovered	-1.45±0.26	-2.85±0.30	1.01±0.17	1.26±0.22	108±32	16±5	89±10

Rows that start with the word Model refer to the clusters we inserted to be recovered for the algorithm and the time we evolved then. The rest of rows refers to the statistics of the recovered clusters. Columns are: proper motion in RA and Dec directions, standard deviations for the proper motions, cluster radius, percentage of stars recovered from the original model and percentage of stars contamination in the recovered cluster. The uncertainties are the standard deviation for the 50 runs in each case.

4.3.3 Mass estimation

In order to estimate the mass of the co-moving groups, we employed the python package Spisea (Hosek et al., 2020). This package allows the generation of single-age, single-metallicity clusters, which we utilized to generate models for comparison with the selected co-moving groups. Firstly, we assigned extinction and differential extinction to the model. To compute these values, we utilized the extinction value of each star in the cluster from the catalog provided by Nogueras-Lara et al. (2021a) along with its standard deviation. Secondly, we assigned a mass and an age to the model and generated a simulated cluster. Then, we established a reference interval using a bright and a faint star within our co-moving group. Next, we compared the number of stars within this interval in our simulated cluster to that of the co-moving group. If the simulated cluster had a higher number of stars within the interval, we adjusted the mass of the model to a smaller value and generated a new simulated cluster. We repeated this process, gradually decreasing the mass of our simulation by 1% increments until the number of stars in the reference interval of the model is not bigger than the number of stars inside the reference interval of the co-moving group.

To assess the reliability of this approach, we initially applied this procedure using the members considered likely to be part of the Arches cluster according to Hosek et al. (2022). (Fig. 4.B.1 top row, left plots). The mean extinction was calculated by performing a crossmatch with the catalog for the GC by Nogueras-Lara et al. (2021a). In addition, we assigned an age of 2.5 million years to the model (Najarro et al., 2004; Espinoza et al., 2009) and solar metallicity (Najarro et al., 2004). We adopted a one-segment power-law model for the initial mass function (IMF) with a slope of $\alpha = -1.8$, according to Hosek et al. (2019). Due to the quality of proper motion data in the catalog, for magnitudes fainter than K$\sim$17 and brighter than K$\sim$11, the number of stars generated in the simulated cluster differs significantly (by more than threefold) from the observed count in the Arches cluster. As a result, we limited the reference interval for comparison to stars with magnitudes between K = 17 and K = 11 mag. Then, we iteratively adjusted the model mass until the number of stars in the model was not greater than the number of stars in the cluster. The procedure was repeated 50 times, and the resulting mean mass and standard deviation values were recorded. We obtained an estimated mass of approximately 12264 ± 495 $M_{\odot}$, which is consistent with the estimated mass of the Arches cluster (Harfst et al., 2010; Clarkson et al., 2012). The results of one of these 50 runs are presented in Fig. 4.6.

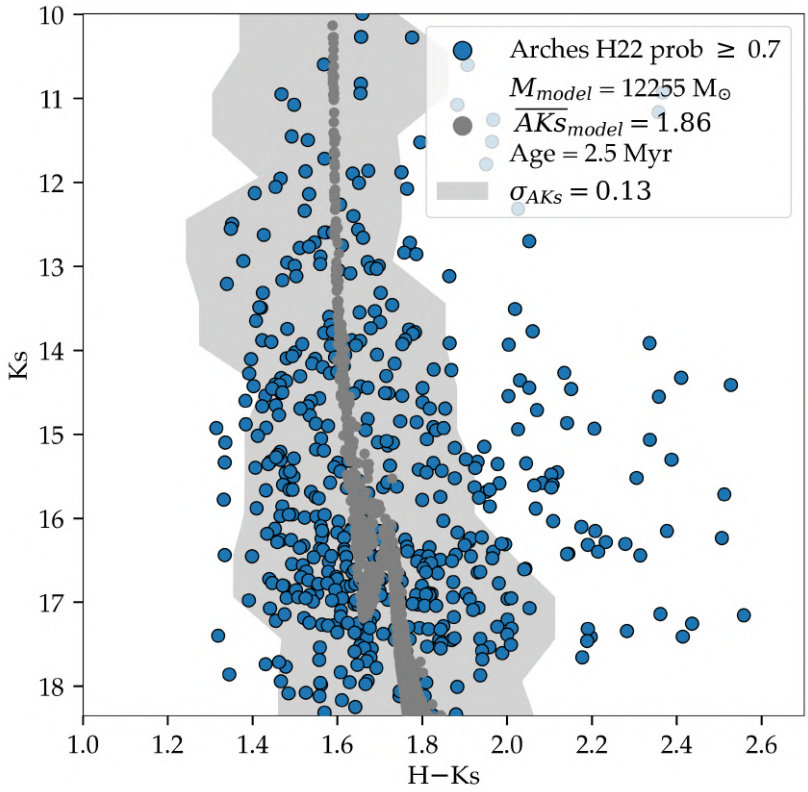

Fig. 4.6 Arches cluster versus simulated cluster: CMD comparison. The blue dots represent the members of the Arches cluster, while the gray dots represent a simulated cluster with an age of 2.5 Myr. The mean extinction is given by AKs = 1.85. The shaded area in the plot represents the uncertainty in the position of the model members in the CMD due to differential extinction, σ_{Aks}.

4.4 Results

Given the constraints posed by our algorithm and the relatively rapid dissolution of clusters in the NSD, we are compelled to confine our search to specific regions where the presence of young stars is likely. Thus, we restricted our search to around the massive stars listed in the catalog by Clark et al. (2021), which cannot be significantly older than 10 Myr. The maximum radius of the co-moving groups that we were able to recover from the simulation is $\sim$ 100 arcsec($\sim$ 4 pc). So, based on this, we limited the search area to a radius of 50 to 150 arcseconds around the massive stars. Then, we identified the massive young stars from Clark et al. (2021) that have a counterpart in L21 after the quality cut. This selection accounts for a total of 59 objects, indicated by the black and green dots in Fig. 4.1.

We divided the search methodology into two distinct parts. Firstly, we applied our algorithm to each of the massive stars, exploring 20 different configurations. These configurations

involved changes in the search radius (50, 75, 100, 125n and 150 arcseconds) and the value for N_{min} (15, 20, 25, and 30). In this initial phase, we identified and selected six distinct massive stars that exhibit co-movement within a group.

The high density of sources in the NSD increases the probability of stars being closely positioned in the 5D space, which could potentially lead to the detection of spurious clusters or associations. To address this issue, we conducted a simulation-based study as the second part of our analysis. In this phase, we ran our algorithm over simulated populations and compared the resultant clusters with those obtained from real data. We conducted this analysis for each of the previously identified co-moving groups, utilizing the stars in their vicinity as the basis for the simulated populations. In the simulations, we kept the positions and magnitudes of the sources unchanged while randomly mixing their velocities. We then applied the algorithm to the simulated population. Since the velocities of the stars were shuffled, any group found in the simulations would represent statistical clusters (i.e., the outcome of random associations). We repeated this process 10000 times for each of the six cases. Subsequently, we compared the relationship between the area and the number of stars for these clusters with those found in the real data. The assigned area for each identified group corresponds to the minimum bounding box, calculated using the Python package alphashape. We show as an example the results of this analysis for the co-moving groups associated with the stars ID 14996 and 427662 (Fig. 4.7 and Fig. 4.8). We can see in the left plots of these figures that the area of the simulated clusters and the number of stars they contain exhibit a clear linear correlation. To quantitatively assess the likelihood that the co-moving group identified in the real data is merely a random association of stars, we compared it with the linear fit of the groups found in the simulations. Specifically, we compared the residual to the linear fit for the groups found in the simulations with the residuals to the same fit for the co-moving groups found in the real data. If the residuals of the co-moving group identified in the real data do not surpass the 3σ level of the residual distribution for the clusters found in the simulations, we discarded it. The right plots in Figs. 4.7 and 4.8 illustrate this comparison for the co-moving group associated with star ID 14996, which passed the cut, and ID 427662, which did not. We extended this analysis to all six identified co-moving groups linked to massive stars. Out of these, four groups successfully met the established criteria (green dots in Fig. 4.1) and were consequently considered unlikely to be the outcome of random stellar associations.

Out of these four co-moving groups, the ones associated with the massive stars ID 14996 and 954199 significantly overlaps. Thus, we decided to run the algorithm around the barycenter of both massive stars. We found a single co-moving group containing both massive stars. Fig. 4.9 shows the vector point diagram, positions and CMD for the co-moving

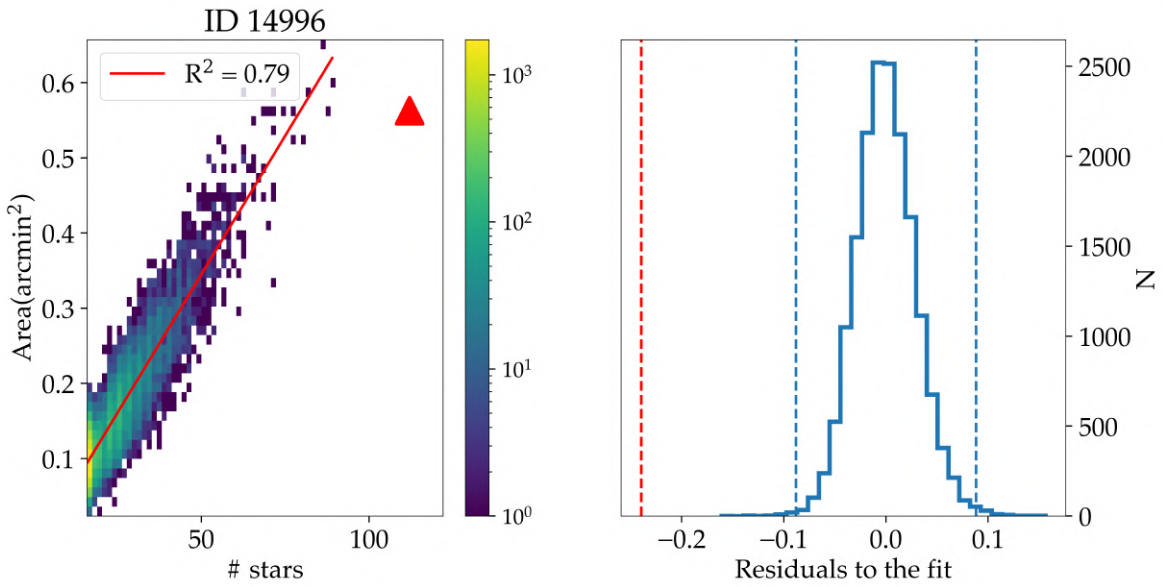

Fig. 4.7 Areal density of the co-moving group associated with star ID 14996 versus simulated clusters. Left: Area versus the number of stars for ∼15000 statistical clusters identified by the algorithm across 10000 simulated populations. The red line represents the linear fit between the area and the number of stars.The red triangle represents the co-moving group associated with star ID 14996. Right: Histogram showing the distribution of the residuals for the groups found in the simulated populations to the linear fit. The dashed blue lines mark the $\pm 3\sigma$ levels of the distribution. The dashed red line marks the residual to the fit for the co-moving group associated with star ID 14996.

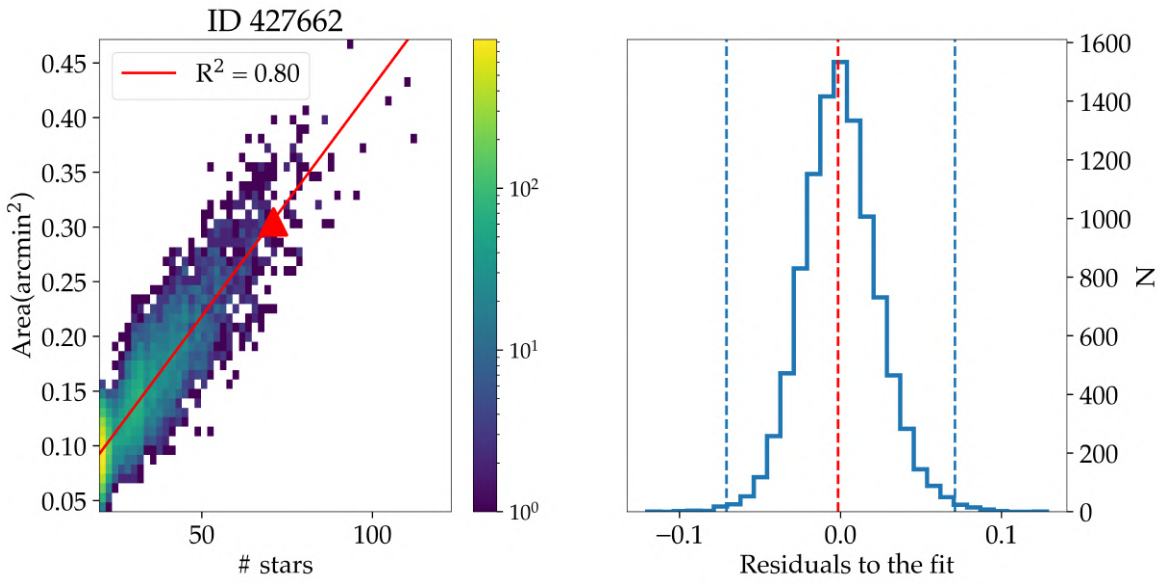

Fig. 4.8 Same as Fig.4.7 but for the co-moving group associated with star ID 427662

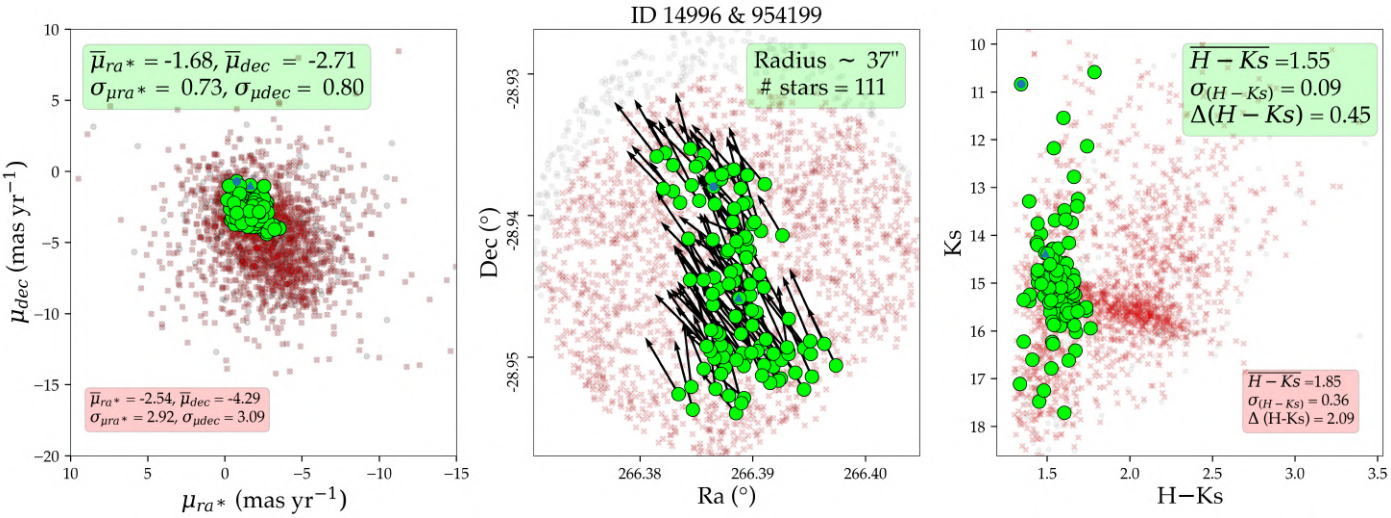

Fig. 4.9 Co-moving group analysis overview. From left to right: Vector-point diagram, coordinates, and CMD. Green points represent the members of the co-moving group. The blue circle and triangle represent the massive stars ID 14996 and ID 954199, respectively. Arrows indicate the direction in the equatorial reference frame. Inside the green boxes are the values for the mean proper motion and sigma for the co-moving group associated with star ID 14996, the number of stars members, the mean color and its sigma, and the maximum difference in color within the group. The radius represents half the distance between the two farthest members of the group. Red crosses mark the stars in the neighborhood of the co-moving group and black dots the rest of the stars in the area.

group associated with star ID 14996 and ID 954199. Fig. 4.C.1 shows similar plots for the rest of the massive stars that are associated with a co-moving group that passed the final cut. In all three plots we show the co-moving groups with the smallest $\sigma_{\mu ra}$ and $\sigma_{\mu dec}$ that we found in each case. To provide a comparison, we have included red crosses to represent the stars surrounding the co-moving group within a distance of approximately 1.5 times the radius of the co-moving group. The corresponding values for these stars are displayed in the red boxes.

The four massive stars associated with a co-moving group are classified by Clark et al. (2021) as either primary or secondary Paschen α emitters (Table 4.2), indicating that they are likely young stars. Furthermore, stars the with IDs 14996 and 154855 are reported by Clark et al. (2021) as a blue supergiant (O4-5 Ia^{+}) and a Wolf-Rayet (WN8-9ha), respectively. This classification suggests that they cannot be older than a few million years.

The co-moving groups linked to stars ID 14996 and ID 954199 are associated with a known HII region (Dong et al., 2017), which further supports the presence of young stars. Both groups have a velocity comparable with the proper motions derived for the Arches cluster by Libralato et al. (2020) – $\mu_{ra}* = -1.45 \pm 0.23$, $\mu_{dec}* = -2.68 \pm 0.14$ mas/yr –

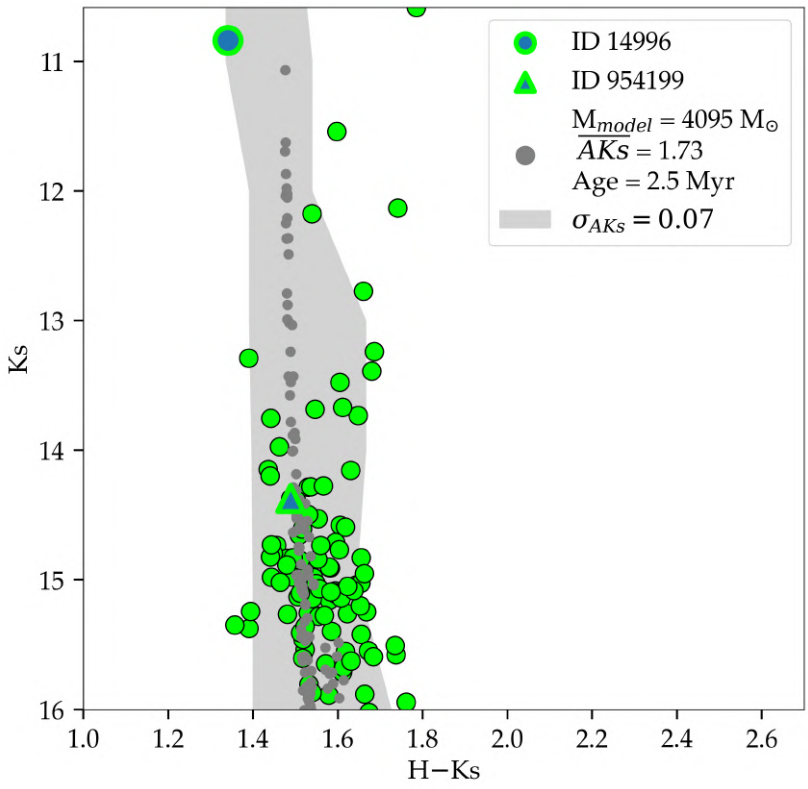

Fig. 4.10 Similar to Fig. 4.6 but for the co-moving group associated with star ID 14996. The point with a blue interior represents the massive star.

which are also calibrated in *Gaia* DR2. Worth to mention that they lie along the path of the most probable orbit for the Arches cluster calculated by Hosek et al. (2022) (cyan line in Fig. 4.1). The positions and velocities of these co-moving groups indicate that they may have formed in a similar location and possibly at a similar time as the Arches cluster. Another possibility is that these groups are part of the tidal tail resulting from the Arches cluster. The velocities and their projected distance from the Arches of approximately 20 pc align well with the tidal tail simulation presented in Habibi et al. (2014).

It is worth mentioning that a co-moving group of six stars in the same area was identified in a different study by Shahzamanian et al. (2019). This study used a different catalog and clustering method. Interestingly, three of these stars have a counterpart in the co-moving group associated with ID 14996. Additional investigations regarding this group will be presented in an upcoming publication (Martínez-Arranz et al. in prep.)

Regarding the groups associated with stars ID 154855 and 139573, they display similar velocities and comparable mean extinctions: $\overline{AKs}_{154855} = 1.85 \pm 0.09$ and $\overline{AKs}_{139573} = 1.85 \pm 0.06$. Additionally, they are relatively close to each other in the plane of the sky.

This proximity suggests that they may have been born as part of the same stellar formation process.

The mean color for all four co-moving groups is around $\overline{H-Ks} = 1.55$ (Fig. 4.9, Fig. 4.C.1). This indicate that they are located close to the outer edge of the NSD (see Fig. 14 in Nogueras-Lara et al., 2019a).

Given the numerous unknown parameters involved, such as cluster membership probability, age, metallicity, and IMF, estimating the masses of the co-moving groups presented in Fig. 4.9 and Fig. 4.C.1 becomes a challenging task. However, for the group associated with massive stars ID 14996 and 954199, if we consider the possibility that it formed through the same process that gave rise to the Arches cluster or is part of its tidal tail, we can adopt similar assumptions for their IMF, metallicity, and age as used for the mass estimation of the Arches cluster (Fig. 4.6). These assumptions include a top-heavy IMF (Hosek et al., 2019), a solar metallicity (Najarro et al., 2004) and an age of 2.5 Myr (Espinoza et al., 2009). Following a procedure similar to the one described in section 4.3.3, we estimated the mass for this group, and the results are presented in the first row of Table 4.2.

For the groups associated with the massive stars ID 154855 and 139573, we conducted a series of simulations using various combinations of metallicity ([M/H] = 0 and [M/H] = 0.3), age (2, 5, and 8 Myr), and two different IMF models: the broken power-law derived by Kroupa (2001) and the top-heavy one derived by Hosek et al. (2019). This resulted in a total of 12 different combinations, each of which was run 50 times for both groups. The estimated masses, along with their standard deviations, are presented in Table 4.2.

All three groups exhibit velocity dispersions ranging from 0.72 to 0.83 mas/yr. In our simulations (Table 4.1), the clusters with these values of velocity dispersion show a contamination level around 55 to 65%. Assuming a similar level of contamination in the co-moving groups we found, along with the aforementioned unknown parameters, could potentially result in variations in the estimated masses by a factor of approximately 2.

4.5 Discussion and conclusions

We have developed a method for scanning the GC for co-moving groups that offers the possibility of tackling the so-called missing cluster problem from a new angle. We present here the first results of this new analysis. We found four different co-moving groups around known massive stars in the NSD. Our toy model roughly estimates the time that it takes for a massive cluster in the GC to dissolve beyond the detection limit of our algorithm, and therefore we are able to restrict the age of the co-moving groups that we present. We believe

Table 4.2 Massive stars within a co-moving group.

ID and Type	RA - Dec	Mass ($M_\odot$)
14996 Ppα	17h45m32.7624s -28d56m16.67	3902 ± 422
954199 Spα	17h45m33.2952s -28d56m44.81	
154855 Spα	17h45m09.6408s -29d11m30.01	5900 ± 850
139573 Ppα	17h45m14.208s -29d11m41.50	5292 ± 825

First column: ID for the massive stars as they appear in L21, and classification by Clark et al. (2021). Ppα and Spα stand for primary and secondary Paschen α emitters. Second: coordinates. Third: estimated masses for the associated co-moving groups and their standard deviation.

that the presence of these groups constitutes direct evidence of recent star formation in the GC.

We analyzed the area around 59 known massive stars in the GC and find that four of them probably form part of a co-moving group. The relatively high velocity dispersion and low density of these co-moving groups, compared to those of the Arches or Quintuplet clusters, suggest two possible scenarios. Firstly, these co-moving groups may have originated from a dense cluster that has already undergone significant dissolution. Alternatively, they may have originated from a less dense stellar association. Recent studies have proposed that a substantial portion of the stars in the GC may have been born as part of loose associations of stars rather than gravitationally bound clusters (Ginsburg and Kruijssen, 2018). Supporting this scenario, the identification of $\sim 10^5$ $M_\odot$ of young stars in the SgrB1 regions (Nogueras-Lara et al., 2022b), which are only ~ 5 million years older than the Arches and Quintuplet clusters, provides further evidence. In the specific case of the group linked to the massive stars ID 14996 and 951499, there is a possibility that it is part of the tidal tail of the Arches cluster.

These groups show that not all apparently isolated massive stars in the NSD are run-away members from the nuclear star cluster, the Arches, or the Quintuplet. They highlight the location of stellar association and/or clusters smaller than Arches or Quintuplet and/or in an advanced state of dissolution (Clark et al., 2021).

On the one hand, the small number of co-moving groups detected by our analysis may be influenced by the quality of the dataset and by our conservative selection criteria. On the other hand, the large number of apparently unaccompanied massive young stars (along with the conclusion by L21 that they are not runaways from the known massive clusters) provides evidence that massive stars may form in isolation in the GC.

With the available datasets, we cannot estimate metallicities or radial velocities. Additionally, our estimations of ages and masses for the entire co-moving group are only rough approximations. To constrain these parameters and confirm the nature of these groups, future spectroscopy observations will be necessary.

The proper motions catalog that we used in this paper covers only a fraction of the NSD, and the uncertainty cut in proper motion that we made in the analysis significantly reduces the number of disposable sources. A wider and deeper set of data is necessary to continue with the search and corroborate these preliminary results. We are currently working on the reduction of a second epoch of GALACTICNUCLEUS that covers the NSD almost entirely. Combined with the first epoch (Nogueras-Lara et al., 2018), this will result in an unprecedented level of precision for proper motion measurements. Preliminary tests suggest an estimated uncertainty of ~ 0.5 mas/yr.

This new technique opens exciting possibilities for research of the GC. A more complete detection of young clusters in the NSD would allow us to address the crucial question of whether the IMF in the GC is fundamentally different from that in the Galactic disk.

Acknowledgments

Author Á. Martínez-Arranz and R. Schödel acknowledge financial support from the Severo Ochoa grant CEX2021-001131-S funded by MCIN/AEI/ 10.13039/501100011033 and support from the State Agency for Research of the Spanish MCIU through the "Center of Excellence Severo Ochoa" award for the Instituto de Astrofísica de Andalucía (SEV-2017-0709). Á. Martínez-Arranz and R. Schödel acknowledge support from grant EUR2022-134031 funded by MCIN/AEI/10.13039/501100011033 and by the European Union NextGenerationEU/PRTR. and by grant PID2022-136640NB-C21 funded by MCIN/AEI 10.13039/501100011033 and by the European Union. We extend our gratitude to Paloma for generously sharing her expertise and guidance.

Appendix

Appendix 4.A Quality check

To assess the quality of the data, we identified the NSD and bulge through stellar kinematics and compared the obtained values with those reported in the literature. Firstly, we transformed the proper motions from equatorial to Galactic with the package SkyCoord from astropy (Astropy Collaboration et al., 2022). Since the proper motions in the L21 catalog are in the *Gaia* DR2 reference frame, we further transformed them into a reference frame where SgrA* is at rest. This transformation involved subtracting the velocity of SgrA* in the International Celestial Reference Frame, which is $(\mu_l, \mu_b)^{SgrA*} = -6.40, -0.24$ mas/yr (Gordon et al., 2023). In Fig. 4.A.1 we can see the distribution of the Galactic proper motions of L21 for the components perpendicular and parallel to the Galactic plane (gray histograms). Then, we fit different Gaussian models to these distributions using the python package dynesty (Speagle, 2020). We found that a two-Gaussians fit best reproduces the perpendicular component and three the parallel one (see Fig. 4.A.1 and Fig.4.A.2). In Table 4.A.1 we can see the values for these Gaussians, which we interpret as representative of the bulge and NSD populations (see Shahzamanian et al. 2022). In the left panel of Fig. 4.A.1, the red Gaussian represents the bulge population and the black one the NSD. In the right panel, the red Gaussian also represents the bulge population. The blue one represents the stars of the NSD that stream toward the Galactic east and the black one those that stream toward the Galactic west. The bulge velocity in this reference frame should ideally be zero, but we can see that the parallel component is $\mu_l = 0.64$ mas/yr. Due to data incompleteness, we tend to detect more stars from the near side of the NSD, introducing a bias in velocities toward stars moving to the west. To rectify this bias, we adjusted the bulge component to center it around zero. Consequently, the revised values for the NSD components are μ_l = 1.97 mas/yr and μ_l = -2.17 mas/yr. These revised results are consistent, within the known uncertainties, with the values previously determined for the mean velocities of stars in the NSD (Kunder et al., 2012; Schonrich et al., 2015; Shahzamanian et al., 2022; Sormani et al., 2022; Martínez-Arranz et al., 2022; Nogueras-Lara, 2022). It is noteworthy to mention that in Libralato et al. (2021b), the fitting

of the data for the parallel component solely involves the use of two Gaussians, without considering the existence of the NSD.

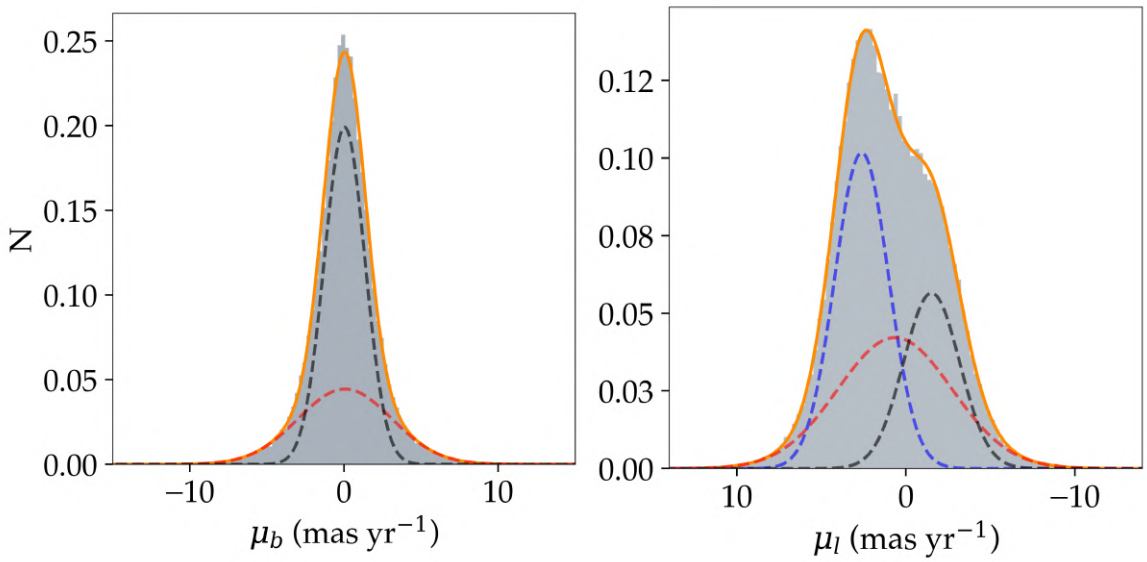

Fig. 4.A.1 Proper motion distributions in L21. Gray histograms represent the proper motion distributions for the perpendicular (left) and parallel (right) proper motion components of the stars in L21. The red Gaussian represents the bulge stars in both plots. The black Gaussian on the left represents the perpendicular component of the NSD stars. On the right, the blue and black Gaussians represent stars on the near and far side of the NSD, respectively.

Table 4.A.1 Best-fit parameters and uncertainties for L21 data (Fig. 4.A.1).

Perpendicular	Bulge	NSD	
$\mu_b\,(mas\,yr^{-1})$	0.07 ± 0.04	0.05 ± 0.02	-
$\sigma_{\mu_b}\,(mas\,yr^{-1})$	3.04 ± 0.05	1.32 ± 0.02	-
amp_b	0.34 ± 0.02	0.65 ± 0.02	-
Parallel	**Bulge**	**NSD**	**NSD**
$\mu_l\,(mas\,yr^{-1})$	0.64 ± 0.07	2.61 ± 0.07	-1.53 ± 0.13
$\sigma_{\mu_l}\,(mas\,yr^{-1})$	3.38 ± 0.13	1.60 ± 0.07	1.66 ± 0.09
amp_l	0.36 ± 0.07	0.41 ± 0.04	0.23 ± 0.04

μ, σ, and *amp* represent the mean velocity, standard deviation, and amplitude of the Gaussians fitted to the distribution.

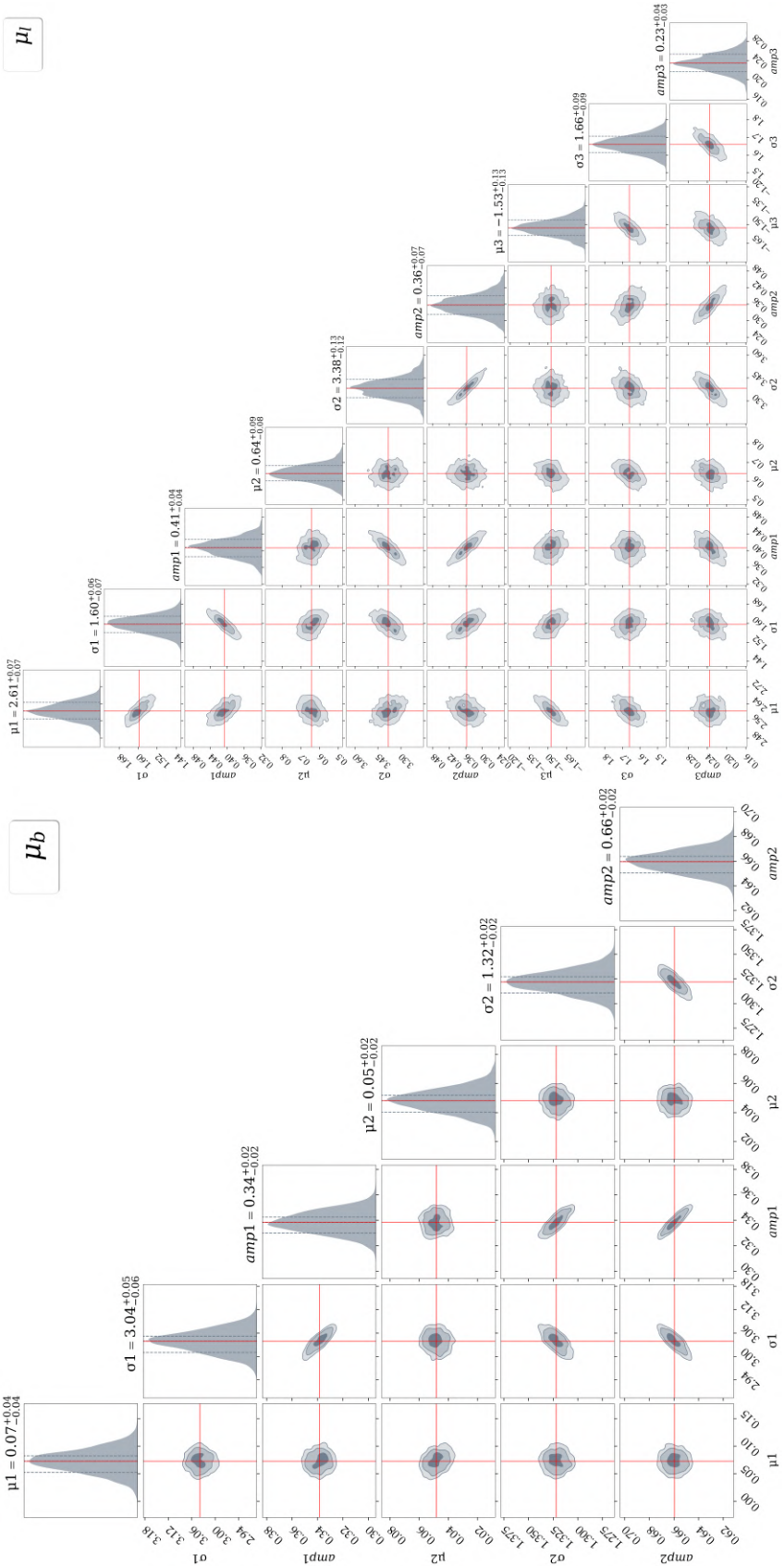

Fig. 4.A.2 Posterior probability distributions of the free parameters for Gaussian fitting for the L21 proper motion distributions: the perpendicular component of the proper motions (left) and the parallel one (right).

Appendix 4.B Testing the algorithm

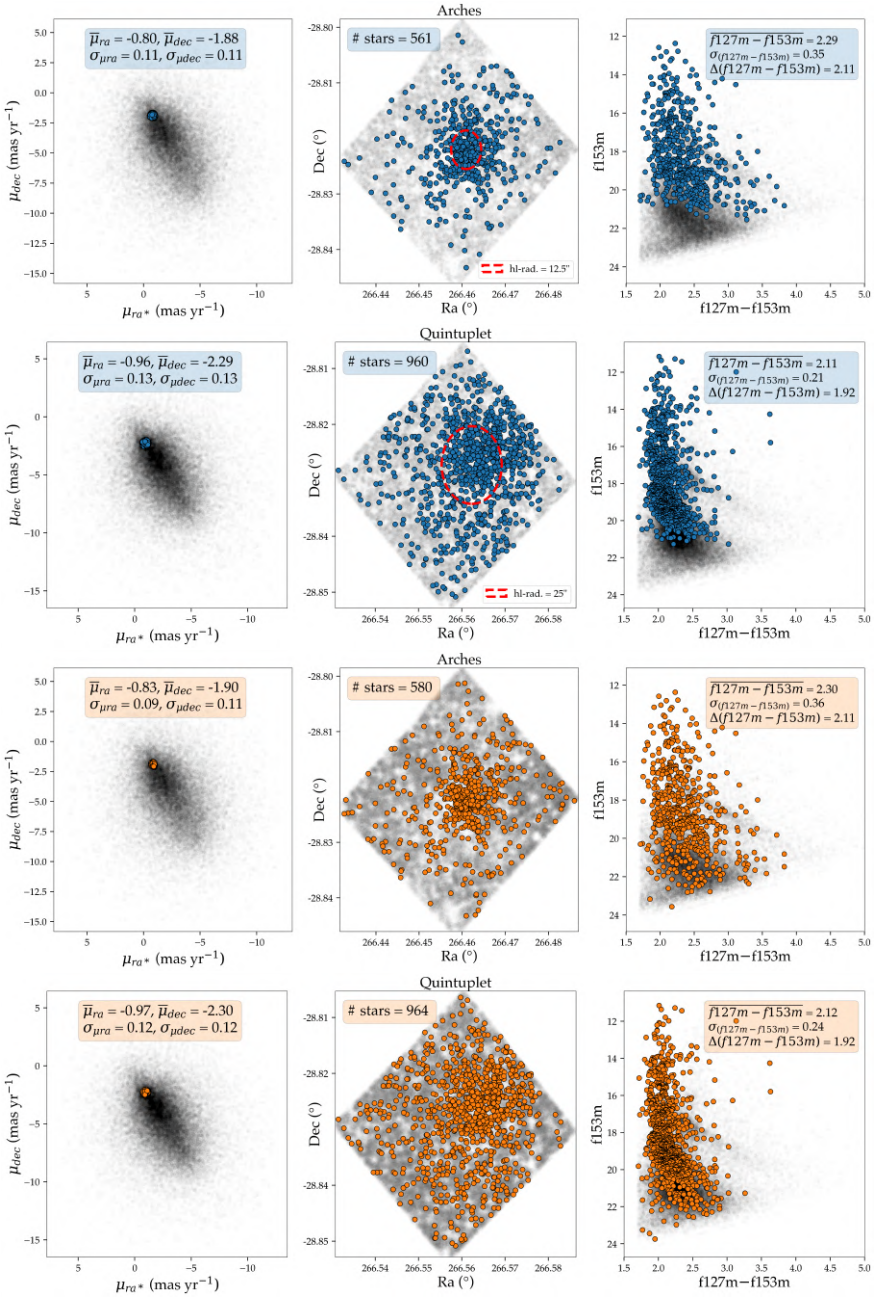

Fig. 4.B.1 Comparison of Arches and Quintuplet clusters based on algorithm settings. In the top row, we present the members of the Arches and Quintuplet clusters according to Hosek et al. (2022). The blue points indicate stars with a likelihood ≥ 0.7 of belonging to the respective clusters, as determined in the aforementioned study. The red circles represent the half-light radii for each cluster, as found in the literature (Hosek et al., 2015; Rui et al., 2019). The left columns display the vector-point diagram, the middle columns show the stellar positions, and the right columns display the CMD. In the bottom row, we present the Arches and Quintuplet clusters as recovered by the algorithm when configured to search only in 2D space formed by the proper motion components. With this configuration, 75% of the stars labeled as Arches members match those of Hosek et al. (2022), and 85% in the case of Quintuplet cluster.

Appendix 4.C Results

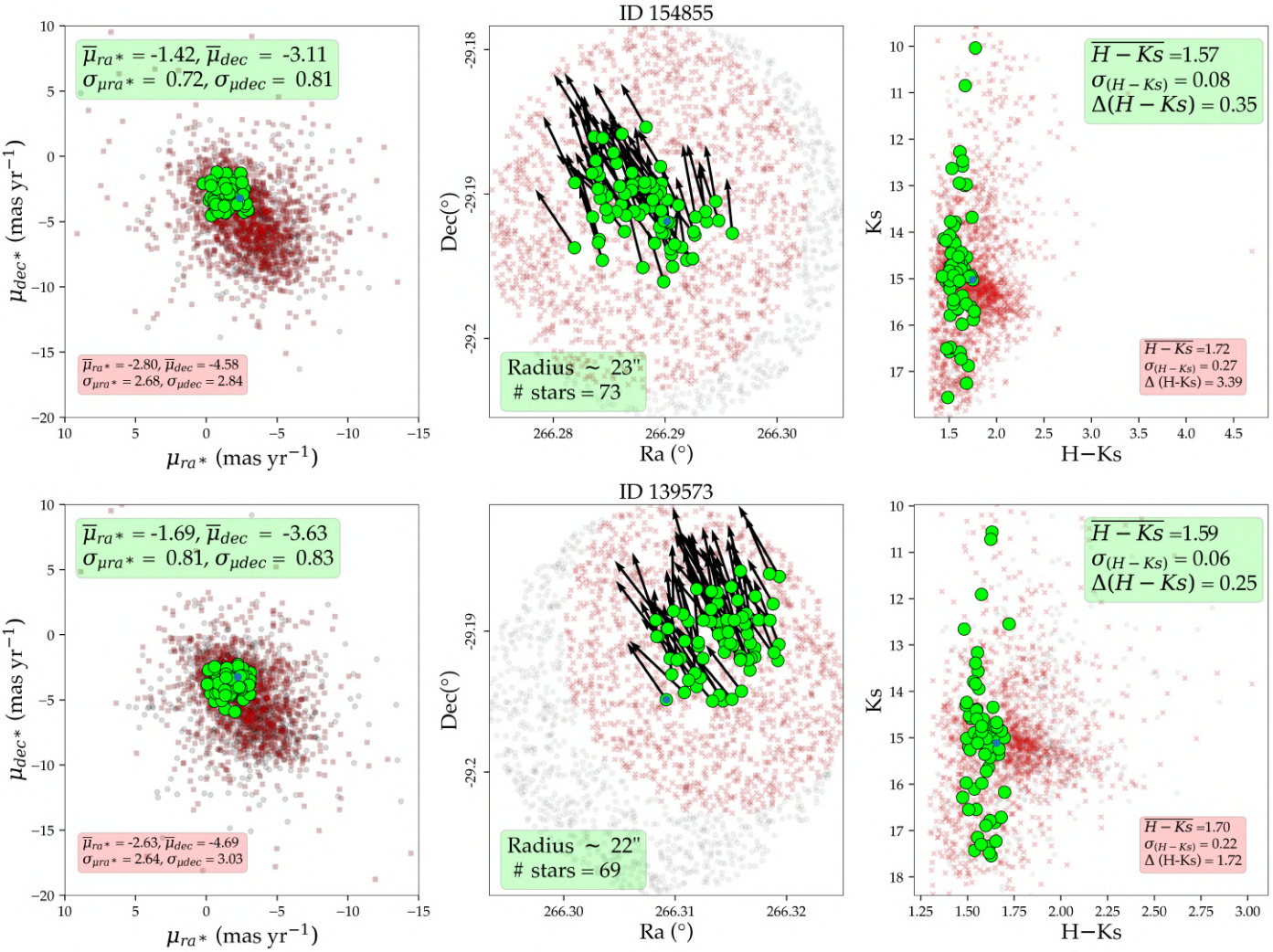

Fig. 4.C.1 Same as Fig. 4.9 but for the rest of the massive stars that belong to a co-moving group (green points in Fig. 4.1)

Chapter 5

Young Cluster at the Galactic Center

This chapter contains the literal transcript of the published article, *Spectroscopic evidence of a possible young stellar cluster at the Galactic Center* (Martínez-Arranz et al., 2024b). it confirms that a co-moving group identified by our previous work (Martínez-Arranz et al., 2024a) is indeed a young cluster with high probability.

Spectroscopic evidence of a possible young stellar cluster at the Galactic Center

Á. Martínez Arranz[1], R. Schödel[1], F. Nogueras-Lara[2], F. Najarro[3], R. Castellanos[3], and R. Frediani[1]

[1]*Instituto de Astrofísica de Andalucía (CSIC), University of Granada, Glorieta de la astronomía s/n, 18008 Granada, Spain*

[2]*Max-Planck Institute for Astronomy, Königstuhl 17, 69117 Heidelberg, Germany*

[3]*Centro de Astrobiología (CSIC/INTA), ctra. de Ajalvir km. 4, 28850 Torrejón de Ardoz, Madrid, Spain*

Astronomy and Astrophysics: Galactic structure, stellar clusters and populations. V683, A13
DOI: 10.1051/0004-6361/202449877

Abstract

The nuclear stellar disk has been the most prolific star-forming region in the Milky Way over the past ∼30 million years. Notably, the cumulative mass of the three clusters currently found in the nuclear stellar disk, the Quintuplet, the Arches, and the Nuclear clusters, amounts to just 10% of the total anticipated mass of young stars that formed in this period. This discrepancy, known as the missing cluster problem, is attributed to factors such as high stellar density and tidal forces. Traces of dissolving clusters may exist as comoving groups of stars, providing insights into the star formation history of the region. Recently, a new cluster candidate associated with an HII region was reported through the analysis of kinematic data

Our aim is to determine whether the young and massive stellar objects in the region share proper motion, positions in the plane of the sky, and line-of-sight distances. We use reddening as a proxy for the distances.

We reduced and analyzed integral field spectroscopy data from the KMOS instrument at the ESO VLT to locate possible massive young stellar objects in the field. Then, we identified young massive stars with astrophotometric data from the two different catalogs to analyze their extinction and kinematics. We present a group of young stellar objects that share velocities, are close together in the plane of the sky, and are located at a similar depth in the nuclear stellar disk. The results presented here offer valuable insights into the missing clusters problem. They indicate that not all young massive stars in the Galactic center form in isolation; some of them seem to be the remnants of dissolved clusters or stellar associations.

5.1 Introduction

The Galactic center (GC) is located at a distance of ∼,8.25,kpc (GRAVITY Collaboration et al., 2020) and harbors the nuclear stellar disk (NSD). This flat rotating structure (Schonrich et al., 2015; Shahzamanian et al., 2022) spans about 150 pc across and has a scale height of 40 pc (Launhardt et al., 2002; Sormani et al., 2022). With a star formation rate of $\in [0.2-0.8]$ $M_{\odot}$/yr over the past 30 Myr (Matsunaga et al., 2011; Nogueras-Lara et al., 2020), the NSD stands out as the most prolific star-forming region of the Galaxy when averaged over volume. This contrasts with the number of star clusters currently known in the NSD, namely the Arches and Quintuplet clusters, which account for a few percent of this mass at most. This discrepancy, known as the missing clusters problem, can be attributed to the challenging conditions in the GC, including substantial and varying extinction (Nishiyama et al., 2009; Nogueras-Lara et al., 2019b), which limit observations to the near-infrared, making the identification of young stars very challenging. Clusters in this environment dissolve in $\lesssim$10 Myr (Kim et al., 1999; Portegies Zwart et al., 2001; Kruijssen et al., 2014),

and color-magnitude diagrams are dominated by reddening, making them a poor tool for cluster identification (Nogueras-Lara et al., 2018). However, recent studies found substantial masses of young stars in Sgr B1 and Sgr C (Nogueras-Lara et al., 2022a; Nogueras-Lara, 2024), supporting coeval formation followed by rapid dissolution in the NSD.

Identifying young stellar associations via spectroscopy is feasible, but is constrained by the limited field of view and time requirements. It is impractical to cover the entire NSD with spectroscopic surveys, but specific areas can be targeted by identifying comoving groups (Shahzamanian et al., 2019; Martínez-Arranz et al., 2024a). This two-step approach involves first identifying comoving groups and then confirming the presence of young massive stars through spectroscopy to uncover previously undetected clusters or associations.

A comoving group is characterized as a set of stars whose members are close in space and share similar velocities, exhibiting a velocity dispersion lower than that of other stars in the field. It can be defined by a 6D parameter space, three dimensions for the velocity components, and three for the position components. While the available catalogs for the GC only provide positions and proper motions in the plane of the sky, the third dimension in position, the line-of-sight distance, can indirectly be constrained by using observed stellar colors. Given the substantial extinction variability in the NSD (Nogueras-Lara et al., 2021a; Shahzamanian et al., 2022; Nogueras-Lara, 2022) and the almost constant intrinsic colors of observable stars, with variations H−Ks color $\lesssim 0.01$ mag (see Fig. 33 in Nogueras-Lara et al., 2018), we propose that the alterations in color primarily result from extinction (see also Nogueras-Lara et al., 2021a). Therefore, a group of stars exhibiting similar colors likely shares a comparable depth within the NSD (Nogueras-Lara, 2022).

If a comoving group is indeed the remnant of a cluster or a stellar association and is now in the process of dissolution, its member stars should still be relatively young, with ages of about $\lesssim$10 Myr. Massive young stars (MYSs) can be separated from cool late-type stars via an analysis of the spectral CO and Brγ lines in the near-infrared (Paumard et al., 2006; Habibi et al., 2019). Cool late-type stars present the ^{12}CO(2,0), ^{12}CO(3,1), and ^{12}CO(4,2) bandhead absorptions at 2.30, 2.33, and 2.35 μm, respectively. Young hot massive stars do not show these features and occasionally present an emission or absorption Brγ line at 2.16 μm and/or HeI abortion at 2.06 μm.

A comoving group was reported in Shahzamanian et al. (2019). This group was found in a known HII-emitting area (Dong et al., 2017), with the presence of a strong Paschen-α emitting star (Dong et al., 2011; Clark et al., 2021), making this region a solid candidate for hosting MYSs. Subsequently, we collected spectroscopy data of this regions. Here, we analyze the spectra of the objects in the area centered in the comoving group and select the MYSs based on the analysis of their spectra. Finally, we cross-match these objects with two

Table 5.2.1 KMOS observation parameters.

Target	RA, Dec (°)	Date	DIT(s)	[$\lambda(\mu m)$]
Sci	266.3817, -28.9448	3,6/06/21	115	[1.93, 2.50]
Sky	266.1914, -28.8962		NDIT = 1	

different catalogs: the GALACTICNUCLUES survey (Nogueras-Lara et al., 2018, 2019a) and the proper motion catalog by Libralato et al. (2021b), to obtain photometry and proper motions.

5.2 Data and methods

5.2.1 Spectroscopy data

We acquired infrared field spectroscopy data with the Very Large Telescope (VLT) K-band Multi Object Spectrograph (KMOS) at the European Southern Observatory (ESO), under ESO program ID 105.20CN.001[1]. KMOS (Sharples et al., 2013) is equipped with 24 integral field units (IFUs), each offering a field of view of 2.8 by 2.8 arcsec (red square in Fig. 5.2.1). The observations were conducted in MOSAIC mode, where the individual IFUs of the 24 arms are arranged in such a way that with 16 successive telescope pointings, a contiguous rectangular area can be covered (dashed line in Fig.5.2.1). With all 24 IFUs and 16 pointings, it is possible to map an area of ~ 0.8 arcmin^2. In order to eliminate the infrared emission from the atmosphere, we needed to acquire images of an area of the sky that was relatively free of stars. Typically, these images are obtained by jittering the science observations. However, due to the crowded environment of the GC, the sky observations cannot be obtained from the jittered observations of the target field. Thus, we used a separate field centered on a dark cloud in the GC as the sky (Tab. 5.2.1).

We reduced the data using the EsoReflex KMOS pipeline (version 3.0.1, Freudling et al., 2013) using the standard recipes provided by ESO. To correct for atmospheric absorption, we used molecfit (Smette et al., 2015) on a standard star spectrum. The default configuration fits a polynomial to eight intervals, from 1.975 to 2.475 μm. Simultaneous fitting of all eight intervals degrades the quality of the corrections for atmospheric absorption at the shortest and longest wavelengths. To improve this, we divided the intervals into three overlapping groups

[1] https://www.eso.org/sci/publications/announcements/sciann16012.html

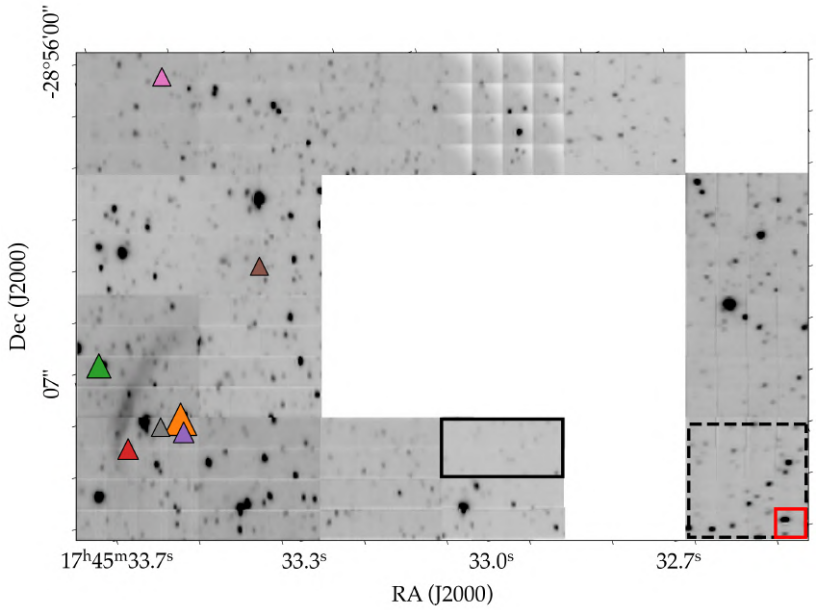

Fig. 5.2.1 KMOS field of view. The colored triangles depict identified MYSs with a K magnitude brighter than 14.5. The size of each point is proportional to its magnitude. The red square represents the area covered by a single IFU. The dashed black square represents the area covered by a single IFU after completing an observational sequence in the MOSAIC mode (16 pointings). The solid black box indicates the size of the fields into which we divided the image to be able to align them with the GC catalogs.

(1.975 to 2.291 μm, 2.269 to 2.379 μm, and 2.360 to 2.475 μm), ran molecfit separately for each group, and then combined the results.

5.2.2 Astrophotometry data

To provide precise astrometric information for the objects in the KMOS image, we conducted a cross match with two different catalogs: the GALACTICNUCLEUS survey (hereafter GNS) (Nogueras-Lara et al., 2018, 2019a), and the 2D proper motion catalog by Libralato et al. (2021b) (hereafter L21). The combined dataset from these two catalogs is referred to as GNS-L21.

GNS

GNS is a near-infrared survey (J, H, and Ks bands) covering an area of approximately 6000 pc^2 in the GC with an angular resolution of 0.2″. This high spatial resolution is achieved through the application of holographic imaging techniques (Schödel et al., 2013). GNS delivers highly precise PSF photometry for over three million stars in the NSD and inner

Galactic bar. In order to eliminate foreground stars belonging to the spiral arms and the bulge, we applied a color cut H−Ks > 1.3 (see Fig. 6 in Nogueras-Lara et al., 2021b) . For more details about the GNS, we refer to Nogueras-Lara et al. (2018) and Nogueras-Lara et al. (2019a)

L21

We used L21 to provide the stars observed with KMOS with proper motion values. This catalog resulted from two observation sets covering approximately 205 arcmin^2 (see Fig. 1 Libralato et al., 2021b). These observations, performed in October 2012 and August 2015, used the near-infrared channel of the Wide-Field Camera 3 (WFC3) on the Hubble Space Telescope (HST). Proper motions were calibrated with reference to *Gaia* DR2 (Gaia Collaboration et al., 2016), yielding absolute proper motion measurements for around 830,000 stars. We trimmed the catalog by discarding stars with proper motion errors exceeding 1 mas/yr. For detailed information on data acquisition, reduction, and analysis, we refer to Libralato et al. (2021b).[2]

5.2.3 Methods

The analysis of the data was divided into two distinct stages: First, we extracted spectra from the objects in the field of view from the KMOS data cubes, and second, we identified these sources in the GNS-L21 catalog.

In the initial stage, we extracted spectra for approximately 300 stars and classified them into two categories: late-type stars or MYS. Our primary criterion was the presence of CO bandhead absorption, which is characteristic of asymptotic giant branch stars and late-type G, K, M giants (Schultheis et al., 2003; Nandakumar et al., 2018). To identify MYSs, we selected objects whose spectra did not exhibit any detectable CO absorption.

We extracted the spectra using an aperture of 0.5 arcsec, corresponding to the full width at half maximum of the standard stars used for calibration in the KMOS pipeline. We performed background subtraction from a ring with a radius of twice the full width at half maximum and a width 0.2 arcsec around each object to eliminate any Brγ interstellar emission, which is pervasive in the GC. We customized the background subtraction to avoid using bad pixels or pixels with strong stellar emission.

To estimate the signal-to-noise ratio (S/N) in the MYSs, we selected wavelength intervals in the spectra without any obvious lines and calculated the S/R as the ratio of the mean and standard deviation of the continuum. To ensure that we selected reliable spectra with a clearly

[2]The proper motions catalogs are available at https://academic.oup.com/mnras/article/500/3/3213/5960177

Table 5.2.2 Parameters of Candela 1 members. Uncertainties in the proper motions are as they appear in LIB21

ID, type	RA, Dec(°)	μ_{RA}, μ_{Dec}(mas/yr)	H	Ks
M1, O4If	266.3865, -28.9380	-0.77±0.53, -0.69±0.38	12.18	10.84
M2, O6V	266.3857, -28.9357	-0.78±0.46, -1.35±0.35	13.71	12.17
M3, O7V	266.3877, -28.9369	-1.73±0.51, -1.94±0.51	14.68	13.29
M4, B0Ia	266.3868, -28.9381	-1.45±0.15, -3.79±0.26	14.66	13.35
M5, B0Ia	266.3818, -28.9388	-0.46±0.44, -2.05±0.29	14.98	13.61
M6, ?B1	266.3774, -28.9353	-1.34±0.22, -1.74±0.28	15.38	13.99
M7, ?	266.3869, -28.9375	-1.09±0.28, -1.93±0.25	15.58	14.15

distinguished level of the continuum from the background and for which we can determine with certainty that no CO lines were present, we classified as MYSs only stars that without these lines had an S/R > 15. This threshold corresponds to stars whose continuum level is at least twice higher than that of the sky. In our context, this applies to stars brighter than Ks∼14.5. In Fig. 5.2.2, we display the spectra of the MYSs with magnitudes brighter than Ks = 14.5. They are color-coded as in Fig. 5.2.1.

In the second part of the analysis, we identified the objects in the KMOS field within the GNS-L21 catalog, enabling us to assign proper motions and H and Ks magnitudes. A significant misalignment issue was present in the 16 pointings necessary for a single IFU to complete an entire tile in mosaic mode (indicated by the dashed black square in Fig. 5.2.1). Specifically, notable misalignment was observed between the first eight and the last eight pointings at most IFUs. To compensate for this, we divided the KMOS field into subfields, each encompassing eight consecutive pointings (approximately 15 arcsec^2), where consistent IFU alignment was maintained (black box in Fig. 5.2.1). Using the astroalign Python package (Beroiz et al., 2020) and dedicated scripts, we cross-matched objects in these parcels with those in the catalogs. Almost all the objects identified in the KMOS field of view, including the seven identified MYSs, had counterparts in the GNS-L21 catalog.

5.3 Results

We display the identified MYSs in the KMOS image with counterparts in the GNS-L21 catalog in the left and central panels of Fig. 5.2.3. We called this group Candela 1, and we refer to it as Can1 throughout. The triangles represents Can1 members, color-coded as in Fig. 5.2.1 and Fig. 5.2.2. The estimated stellar types, coordinates, proper motions, and magnitudes of the Can1 member are shown in Table 5.2.2.

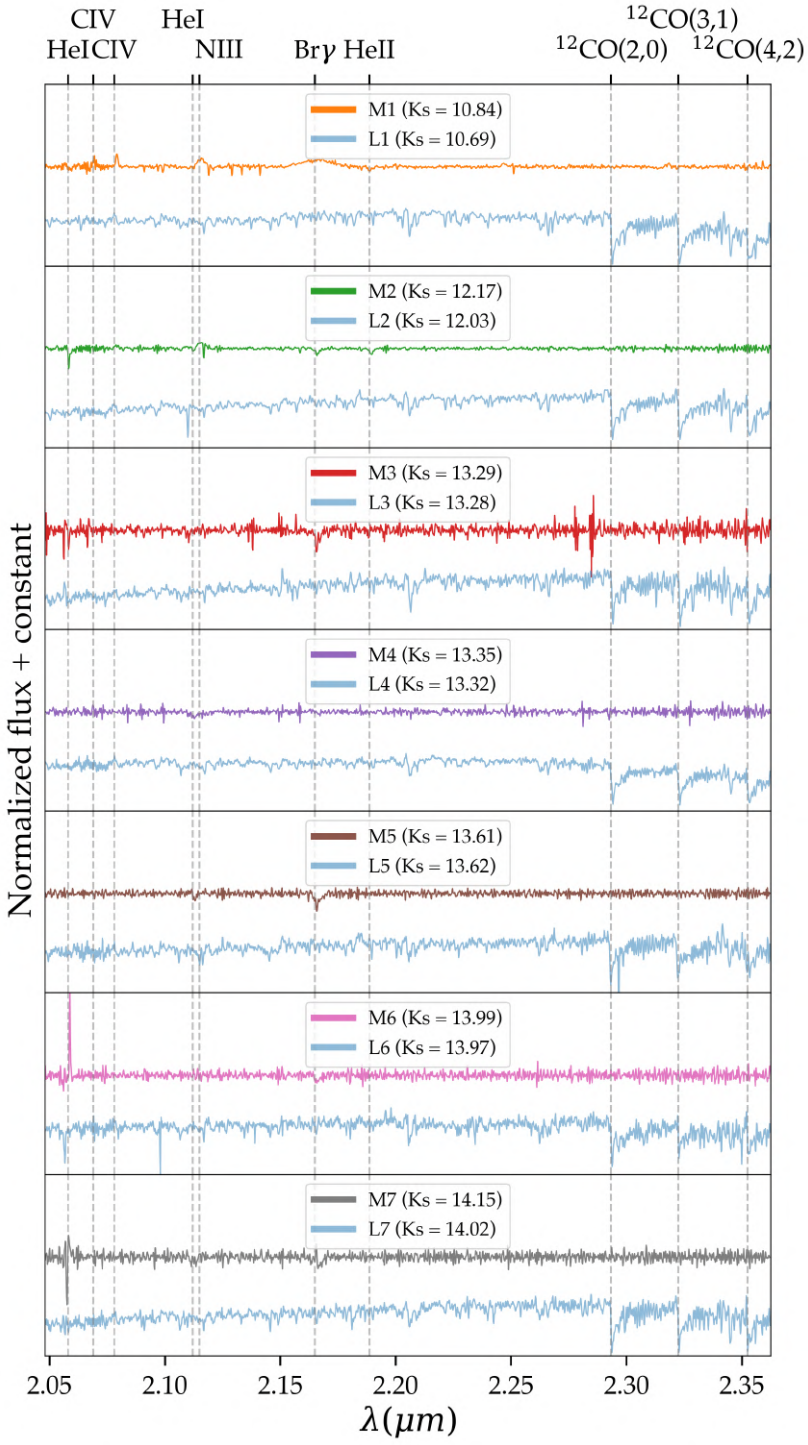

Fig. 5.2.2 Spectra of the MYSs. The MYSs are color-coded as in Fig. 5.2.1 and Fig. 5.2.3. In blue we show for comparison late-type spectra from stars in the field of approximately the same magnitude as the MYSs.

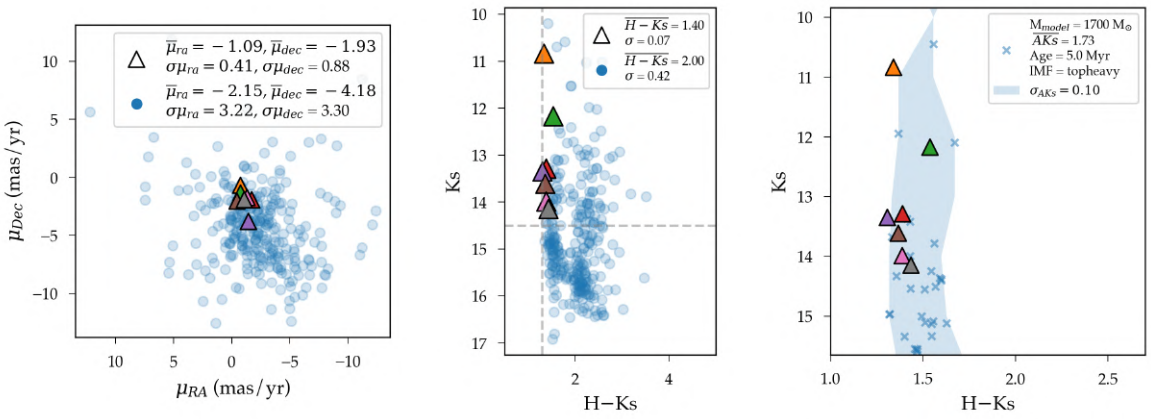

Fig. 5.2.3 KMOS object proper motions and CMD, and cluster simulation. The triangles represent Can1, and the blue circles represent the remaining objects in the field. Left: Vector-point diagram. Middle: CMD. The vertical dashed line marks the color-cut we made to exclude foreground stars (H−Ks = 1.3). The horizontal dashed line marks the magnitude cut we made to exclude stars with low spectroscopic S/R (Ks = 14.5). Right: Spisea cluster simulation. The blue crosses represent members of a simulated cluster. The legend box displays the main features of the cluster. The shaded area represents the uncertainty in the position in the CMD for the members of the simulated cluster due to variations in extinction.

In the left panel of Fig. 5.2.3, we show a vector-point diagram of their equatorial proper motions, and the middle panel shows a CMD. Notably, in the left panel of Fig. 5.2.3, the velocity dispersion of Can1 is significantly lower than the one corresponding to the remaining stars in the field. In the middle panel, we observe that all Can1 members display a similar color, indicating that they are affected by similar extinction. This supports the idea that these stars are located at a similar depth in the NSD. The similar values in velocity, position in the sky, line-of-sight distance, and the fact that all seven members are massive young stars strongly indicates that this group shares a common origin. Moreover, this group is situated within an HII region (Dong et al., 2017), displaying significant Brγ emission, as illustrated Fig. 5.A.1. This provides additional evidence for recent in situ star formation (Hankins et al., 2019).

If Can1 is part of a larger cluster or stellar association, we can estimate its mass by comparing it with simulated clusters. The Python package Spisea (Hosek et al., 2020) allows the generation of single-age, single-metallicity clusters, and we used it to create models for a comparison with Can1. To generate a cluster model, we needed to set several parameters as input for Spisea: distance, extinction, initial mass function (IMF), age, and metallicity. We adopted a distance of 8.25 kpc (GRAVITY Collaboration et al., 2020). We obtained the extinction value for each star in Can1 from the catalog provided by Nogueras-Lara et al. (2021a). Estimating a single value for the remaining variables was challenging with the

current data set. We therefore ran a series of simulations with various combinations. For the ages, we selected four different values ranging from 2.5 Myr, which is the age of the youngest cluster in the NSD, the Arches (Espinoza et al., 2009), to 10 Myr, which is the maximum estimated dissolving time for a massive cluster in the GC (Kim et al., 1999; Kruijssen et al., 2014). For the metalicity, we considered [M/H] = 0 and [M/H] = 0.3 (Najarro et al., 2004; Nogueras-Lara et al., 2020; Schultheis et al., 2021; Feldmeier-Krause, 2022). Additionally, we used two different IMFs: a broken power law derived by Kroupa (2001), and a top-heavy one derived by Hosek et al. (2019). This resulted in a total of 16 possible configurations, each run 400 times, producing a total of 6400 simulations.

For each of these simulations, we defined a magnitude interval to compare the model with Can1, using the brighter and fainter magnitudes of Can1. Then, we randomly assigned either a very low or a very high initial mass to the model and compared the number of stars in the magnitude interval with the number of stars in the Can1. If the number of stars in this interval differed from the number of stars in the Can1, we adjusted the mass of the cluster by either increasing or decreasing it. This process was repeated, and the mass was gradually adjusted with $\pm 1\%$ increments until the number of stars in the magnitude interval for the model equaled the number of stars in Can1. Due to completeness limitations, this method only allowed us to estimate a lower limit for the parent cluster of the comoving group, yielding a value of $M_{estimated} = 1742 \pm 761\ M_{\odot}$. In Fig. 5.2.3 right panel, we present the CMD of one of these 6400 simulated models alongside the real values of Can1 for comparison.

To investigate the probability of finding a group of seven stars classified as MYSs with a velocity dispersion as low as that of Can1 formed purely by a random association of stars in the field, we conducted a permutation test. We found that the probability of a random association of stars exhibiting similar dynamical characteristics is lower than 0.4%. For more details, we refer to Appendix 5.B.

Determining the radial velocities (v_r) of the stars in the comoving group poses challenges due to the featureless spectra they exhibit, in addition to the maximum observation resolution of approximately 30 km/s. Nevertheless, stars M2 and M3 present a sufficiently intense Brγ absorption line and a sufficiently high S/R to facilitate a rough estimation of the v_r . We conducted a Gaussian fitting of the Brγ line, measuring the shift of the line peak relative to the value at rest (Br$\gamma = 2.16612\ \mu m$). Subsequently, we applied the barycentric correction to the measured velocity and expressed it in the local standard of rest of the reference frame. We obtained consistent values for the velocities of these two MYSs, M2 with $v_r \approx$ -40 Km/s, and M3 with $v_r \approx$ -50 Km/s

Finally, we estimated the stellar types for Can1 members by comparing the extracted spectra with the near-infrared spectral atlas provided by Hanson et al. (2005). The estimated

classes are presented in the first column of Table 5.2.2. For star M1, previous studies by Dong et al. (2011) classified it as an O4-6I (star ID P114 in the reference paper), while Clark et al. (2021) classified it as O4-5Ia^{+}. Both classifications align with the one derived in this study, O4If. For the remaining stars, the estimated types range from O6V to B0-1. The classification of the two faintest stars in the group is challenging due to the limited S/R and the constraint of having only Ks-band data.

We can constrain the age of Can1 by considering the lifespan of its more massive members, the O-type stars. For an O-type star, the maximum age range is approximately 5-6 Myr (Weidner and Vink, 2010), which imposes an upper limit for the age of the cluster. This age limit falls within the maximum age of $\lesssim$10 Myr that a cluster can survive in the GC before complete dissolution (Kim et al., 1999; Portegies Zwart et al., 2001; Kruijssen et al., 2014).

It is worth mentioning that most of the stars in Can1 presented here have counterparts in a recently identified comoving group by Martínez-Arranz et al. (2024a) (Fig. 5.C.1), and it partially overlaps with the one reported by Shahzamanian et al. (2019). Notably, these two comoving groups were identified using different catalogs and methods.

5.4 Discussion and conclusion

Shahzamanian et al. (2019) reported on a group of seven comoving stars that might be associated with the GC H1 HII region, which is located at a projected distance of only about 11 pc from Sagittarius A* (see, e.g., Dong et al., 2017; Hankins et al., 2019), and with a strong Paschen-α emitting star, the O super-/hyperrgiant P114 (Dong et al., 2011; Clark et al., 2021). Subsequently, Martínez-Arranz et al. (2024a) exploited the HST WFC3 proper motion catalog of Libralato et al. (2021b) and found a group of 110 comoving stars associated with P114 (ID14966 in Libralato et al., 2021b), which may indicate the presence of a young cluster of a few thousand solar masses. The comoving group identified in Shahzamanian et al. (2019) has elements in common with the group reported by Martínez-Arranz et al. (2024a).

We presented spectroscopic observations of an area associated with this potential cluster or stellar association. We assigned proper motions and magnitudes to approximately 300 stars, about one-third of which had a sufficiently high S/R to classify them as late-type giants or early-type massive young stars. We found seven young massive stars, including P114. Five of these stars lie within a radius of $\sim$ 5" at a projected distance (about 0.20 pc at the distance of the GC) of P114, and the sixth star lies at $\sim$ 15" (0.60 pc) (Fig. 5.2.1). The massive young stars lie very close to each other in the proper motion diagram (left panel in Fig. 5.2.3). We called this group Candela 1 (Can1). Furthermore, all star in Can1 have the same HKs colors

within the uncertainties, which supports the idea that they also lie close to each other along the line of sight (central panel in Fig. 5.2.3). It is worth noting that Can1 is situated very closely to the more probable orbit for the Arches cluster as derived by Hosek et al. (2022). (see also Fig. 1 in Martínez-Arranz et al., 2024a). Additionally, the projected distance from the Arches, approximately 20 pc, aligns well with the tidal tail simulation presented in Habibi et al. (2014). Considering these coincidences, the possibility that Can1 may represent traces of a tidal tail associated with the Arches cluster cannot be ruled out. Deeper and more comprehensive observations of the area are necessary to cover the unobserved areas around the main group and acquire spectra with higher S/R, enabling us to classify fainter sources.

Based on these results and on the coexistence with an HII region in the plane of the sky, the evidence is now sufficiently strong to consider Can1 as a newly discovered young cluster at the GC. While we have for several decades known only three young clusters in the GC (Arches, Quintuplet, and the central parsec) plus a few hundred known massive stars distributed throughout the field (Clark et al., 2021), proper motion studies of the GC are now sufficiently precise and complete that we can determine potential clusters via kinematics and then confirm them spectroscopically. This opens a new window into studying star formation in this unique astrophysical environment. Only $\lesssim 5\%$ of the area of the NSD has been exploited with this method, and only one candidate cluster was confirmed spectroscopically so far. This suggests that we may still be able to discover a dozen or more new clusters. All of of them will probably be younger than $\sim$10 Myr because significantly older clusters are expected to have dissolved (Kim et al., 1999; Kruijssen et al., 2014). After having found these new clusters, we will be able to study them in more detail. The perhaps most important question to address will be whether the IMF at the GC is indeed different from the Galactic disk, as indicated by the observations of the three known clusters and as also motivated by theoretical considerations (e.g. Morris, 1993; Bartko et al., 2010; Hußmann et al., 2012; Hosek et al., 2019)?

Acknowledgments

Author Á. Martínez-Arranz and R. Schödel acknowledge financial support from the Severo Ochoa grant CEX2021-001131-S funded by MCIN/AEI/ 10.13039/501100011033 and support from the State Agency for Research of the Spanish MCIU through the "Center of Excellence Severo Ochoa" award for the Instituto de Astrofísica de Andalucía (SEV-2017-0709). Á. Martínez-Arranz and R. Schödel acknowledge support from grant EUR2022-134031 funded by MCIN/AEI/10.13039/501100011033 and by the European Union NextGenerationEU/PRTR. and by grant PID2022-136640NB-C21 funded by MCIN/AEI 10.13039/501100011033 and by the European Union. R.F. acknowledges support from the grants Juan de la Cierva FJC2021-046802-I, PID2020-114461GB-I00 and CEX2021-001131-S funded by MCIN/AEI/10.13039/501100011033 and by "European Union NextGenerationEU/PRTR" and grant P20-00880 from the Consejería de Transformación Económica, Industria, Conocimiento y Universidades of the Junta de Andalucía. We express our gratitude to the referees for their valuable comments and suggestions, which have improved the readability and quality of this manuscript. We would like to thank the staff of the Candela bar in Granada.

Appendix

Appendix 5.A Data reduction

In Fig. 5.A.1, we present a Brγ emission map constructed from the current KMOS dataset. It is evident that most of the Can1 members are situated near the region of stronger emission. This intense Brγ emission is associated with active star formation.

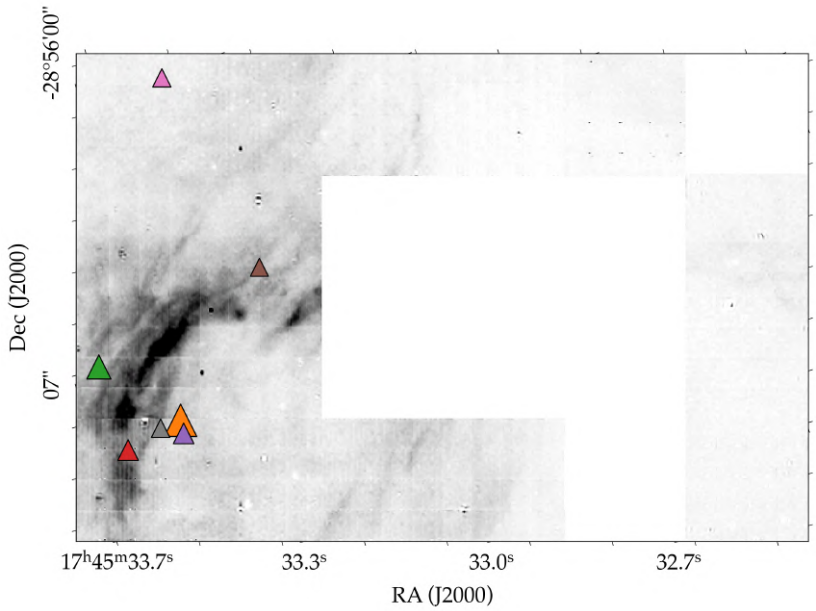

Fig. 5.A.1 Brγ map obtained after continuum subtraction of the same area of Fig. 5.2.1. The colored triangles depict identified MYSs with a K magnitude brighter than 14.5. The size of each point is proportional to its magnitude.

Appendix 5.B Simulations

We conducted a permutation test to assess the likelihood of randomly finding a group of seven stars classified as MYSs with a velocity dispersion as low as that of Can1. The statistical test we used was the difference in the values of the velocity dispersion between the members of Can1 and the remaining field stars classified as late type, considering only stars with Ks magnitudes brighter than Ks = 14.5. The observed difference in the velocity dispersion for the real data is $|\sigma\mu_{Can1} - \sigma\mu_{late}|$ = 1.98 mas/yr (dashed line in Fig.5.B.1). We then randomly shuffled the velocities between all the stars and compared the differences in the velocity dispersions. This process was repeated 20,000 times, and the results are shown in Fig. 5.B.1. Only about 0.4% of the 20,000 simulated MYS groups had a $|\sigma\mu_{MYS} - \sigma\mu_{late}|$ equal to or higher than the real data (blue histogram to the right of the dashed line in Fig. 5.B.1), indicating that the observed association of stars that formed Can1 is highly unlikely to have occurred by chance.

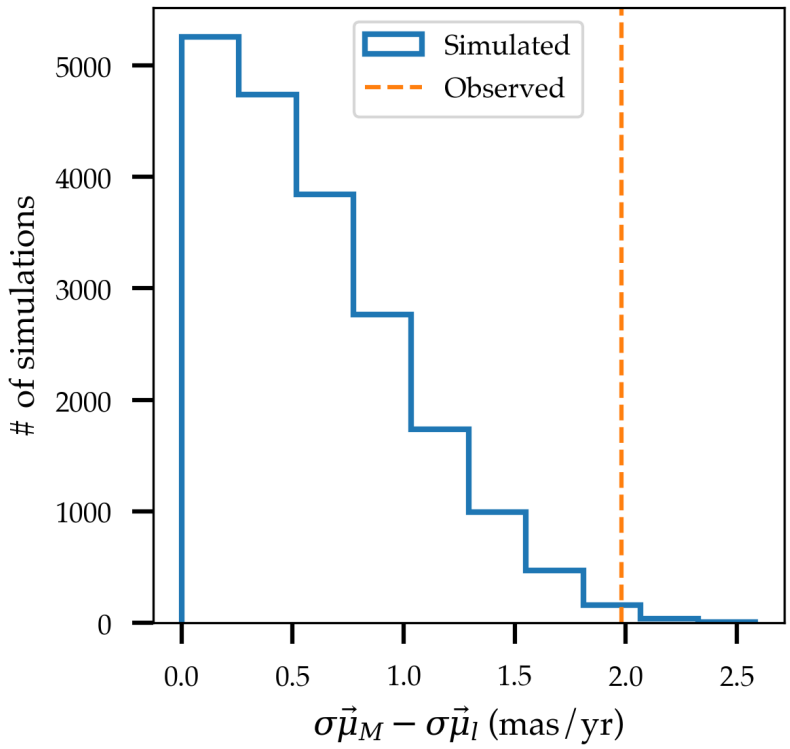

Fig. 5.B.1 Velocity dispersion simulations. The blue histogram represent the difference in velocity dispersion between simulated populations of MYSs and late-type stars that where created by shuffling the velocities among the observed sample of stars. The dashed orange line represents the value between Can1 and the late-type stars.

Appendix 5.C Results

In Fig. 5.C.1, we depict the members of the comoving group found by Martínez-Arranz et al. (2024a) in blue and Can1 in orange. We mark in green the members of Can1 with a counterpart in the comoving group (Mar23). Can1 appears to be part of a larger comoving group whose members extend beyond the KMOS field we analyzed here. Further KMOS data will be acquired in an adjacent area (dashed gray square in the image) to confirm this observation.

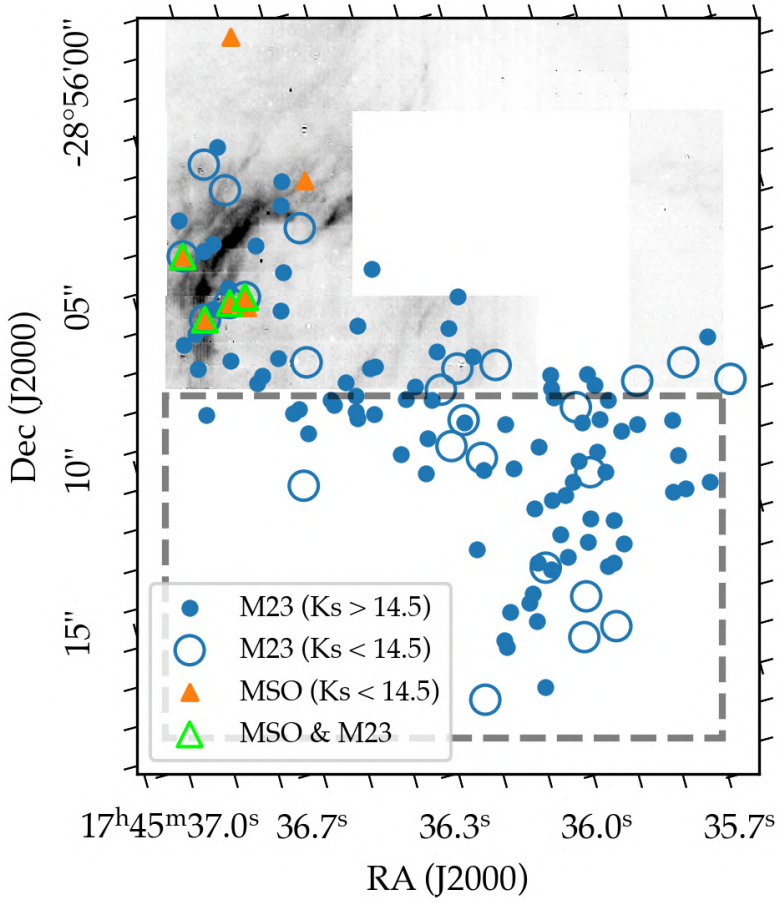

Fig. 5.C.1 Comoving group and MYSs on a the Brγ emission map. The orange triangle represents Can1 members. The blue points and circles represent the comoving group presented in Martínez-Arranz et al. (2024a) (Mar23). The green triangles represent the elements in common between Can1 and Mar23. The dashed square outlines the region scheduled for observations using the KMOS instrument during ESO period P113.

Chapter 6

Future work

During the course of this research, we have developed a methodology to constrain the distance to the dense molecular cloud, the Brick, and demonstrated that it is located at the GC, approximately 8.2 kpc away from Earth. This methodology can be extended to other dense molecular clouds. By combining extinction measurements with proper motions, we can also constrain the line-of-sight distance of co-moving groups of stars in the NSD (Nogueras-Lara et al., 2021b; Nogueras-Lara, 2022). We have also developed tools to scrutinize proper motion and astrophotometry catalogs in search of comoving groups of stars, which have the potential to pinpoint the location of stellar clusters or associations in the NSD.

In both cases, we are limited by the same factors. Firstly, the extent of the proper motion catalogs that we have at our disposal. Of the approximately 16,000 pc^2 spanned by the NSD (Nogueras-Lara et al., 2020), the catalog by Libralato et al. (2021b) covers only about 6%, or approximately 920 pc^2 (marked by orange solid rectangles in Fig. 6.0.1). The second limiting factor is the precision of the proper motions. In order to achieve reliable proper motion measurements, we have established a quality cut of 1 mas/yr in the uncertainty of the proper motion we use in the search for co-moving groups (see Fig. 4.2), resulting in a significant loss of information. The catalog by Hosek et al. (2022), with better precision, covers only the area around the Arches and the Quintuplet cluster, totaling approximately 55 pc^2 (marked by orange dashed squares in Fig. 6.0.1). To conduct a systematic search for clusters or stellar associations in the NSD, we need an extensive catalog that covers a significant portion of the NSD and with sufficient precision to allow the use of fainter sources.

We have confirmed that one of the co-moving groups identified in Martínez-Arranz et al. (2024a) is probably a young cluster or stellar association (Martínez-Arranz et al., 2024b). Based on the expected star formation in the NSD (Matsunaga et al., 2011; Nogueras-Lara et al., 2020), we anticipate finding more such clusters or associations. The recent discoveries of several 10^5 $M_\odot$ of young stars in the Sgr C and Sgr B1 areas (Nogueras-Lara et al.,

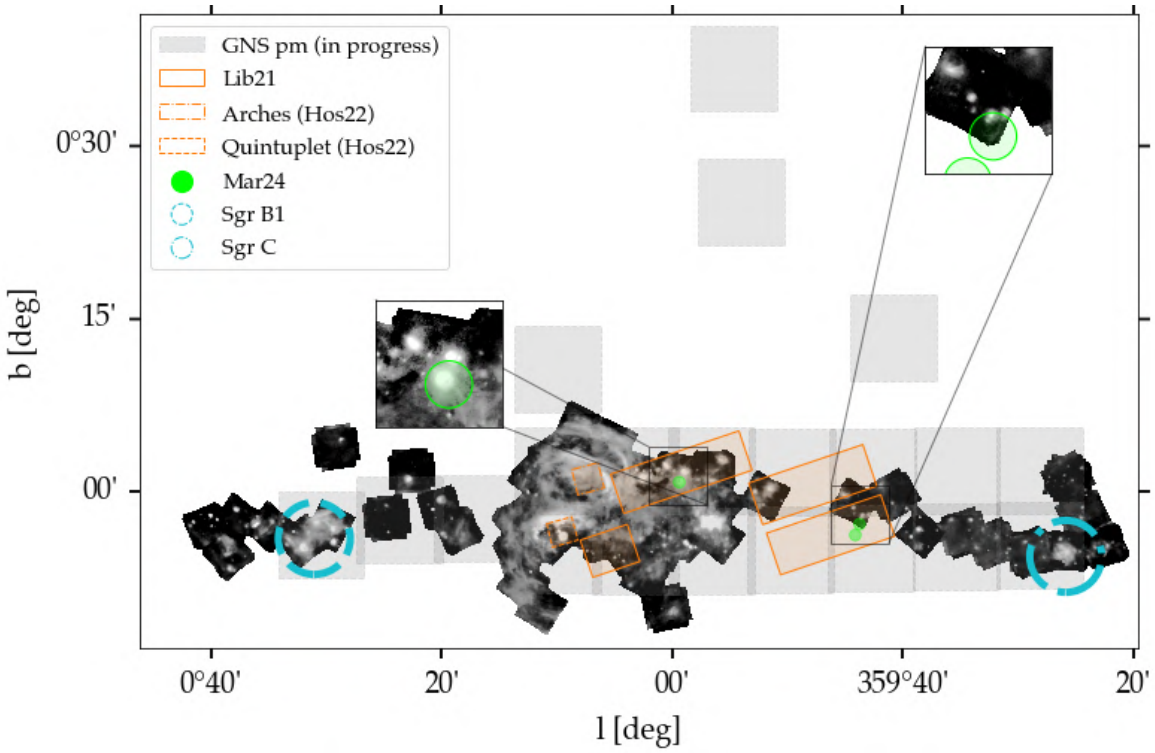

Fig. 6.0.1 Mid-infrared (37 μm) map of the GC form the SOFIA/FORCAST legacy survey (Hankins et al., 2020). We have overploted the area covered by the proper motions catalogs by (Libralato et al., 2021b) and (Hosek et al., 2022) in orange. The area covered by the future proper motion catalog derived from the two epochs of GNS is marked in gray (Matínez-Arranz et al. in prep.). In green we marked the positions of the comoving groups found by (Martínez-Arranz et al., 2024a). The blue circles mark the positions of the star forming regions of Sgr B1 and Sgr C.

2022b; Nogueras-Lara, 2024) further support this hypothesis. Thus, we need a high quality astrophotometric catalog to analyze the proper motions, positions, and colors of the stars in a significant area of the NSD. This catalog should, in particular, cover regions characterized by ionized gas and mid-infrared dust emission, such as Sgr B1 and Sgr C, that are tracers of star formation and for the presence of young massive stars.

In Fig. 6.0.1, we present a 37 μm emission map of the central few hundred parsecs of the GC. Superposed on this image are the areas covered by the catalog of Libralato et al. (2021a) and by the forthcoming GALACTICNUCLEUS proper motion survey, depicted by the shaded areas. The circles denote the approximate locations of Sgr B1 and Sgr C. We can appreciate that the clusters or stellar associations found by Martínez-Arranz et al. (2024a), represented by green circles, are closely aligned with or in proximity to areas of strong emission. The GNS proper motion catalog will encompass a vast area of the NSD,

including the Sgr B1 and Sgr C regions and many other strong HII and dust emission spots. These intense emission areas will be the first targets for our cluster searching algorithm.

Finding young clusters or stellar associations will enable us to study their IMF and gain a better understanding of the star formation process in the extreme environment of the GC. First, we need to identify co-moving groups that are reliable candidates for pinpointing the positions of young clusters or stellar associations. Follow-up spectroscopic observations will be necessary to confirm the cluster nature of these groups. Observations with the KMOS/VLT field spectrograph of the co-moving groups presented in Martínez-Arranz et al. (2024a) have already been scheduled (ID: 113.26CB.001, PI: Martínez-Arranz Á). If these clusters are confirmed, high-precision astrometry with JWST/HST or ground-based instruments such as ERIS/VLT will be required to obtain accurate information on the cluster membership of each star. This will be followed by an analysis of the present-day mass function, allowing us to constrain the IMF.

6.1 The GALATICNUCLEUS proper motion catalog

The GNS catalog (Nogueras-Lara et al., 2019a, hereafter GNS I) had a significant impact on astrophotometric studies of the GC. It was acquired with the wide-field near-infrared camera HAWK-I/VLT, with fast photometry mode and reduced with the speckle holography algorithm (Schödel et al., 2013) to provide a high homogeneous angular resolution of 0.2". The survey covered an area of about $\sim$6000 pc^2 and provide accurate photometry for about $\sim 3.3 \times 10^6$ stars in the J, H and Ks bands, with an uncertainty of $\lesssim 0.05$ mag in all three bands.

In the left panel of Fig.6.1.1, we show a comparison of the GNS I catalog with the leading catalogs at the time: the Simultaneous Infrared Imager for Unbiased Survey (SIRIUS, Nishiyama et al., 2006) and the VISTA Variables in the Vía Láctea (VVV, Minniti et al., 2010). GNS I reaches more than 1 magnitude deeper in the J band and over 2 magnitudes deeper in the H and Ks bands than SIRUS or VVV.

In 2022, seven years after GNS I, a second epoch of imaging data was acquired,hereafter termed GNS II. It covers the area depicted as grey squares in Fig. 6.0.1. The general observing strategy and the reduction pipeline were similar for both surveys, although GNS II used only the H band. The left panel of Fig. 6.1.2 shows the flowchart for the pipeline used for the reduction of GNS Iand GNS II.

There are two main differences between the two epochs: One is the detector size. In GNS I, the fast photometry mode was used, with a DIT of 1.26 seconds, which required using only a third of the detector, i.e. 2048$\times$768 pixels. In GNS II we set a DIT of 3.3 seconds,

which allowed us to use the whole chip, 2048×2048 pixels. In the top right panel of Fig. 6.1.1 we show the chip sizes of GNS I and GNS II on the same area of the sky. The second difference is the used of Ground-layer adaptive optics assisted by Laser (GRAAL, Paufique et al., 2010) in GNS II. The combination of a longer DIT with adaptive optics resulted in deeper and sharper images. In the bottom right panel of Fig. 6.1.1, we show the H luminosity function for stars in the overlapping of the same two chips for the two different epochs. We can see that number of sources detected in GNS II is more than double that in GNS I, reaching over half a magnitude deeper.

The reduction of the whole GNS II survey and the publication of the GNS proper motion catalog is work in progress. However we have reduced a test field from GNS II and combining it with GNS I to compute proper motions. For the proper motion computation we followed two different approaches to produce two different catalogs: One linked to the International Celestial Reference System (ICRS) using the Gaia stars present in the field, which we called the *absolute* proper motion catalog; and another, which we called the *relative* proper motion catalog, where we adopted the stellar positions of the GNS II epoch as the reference frame.

6.1.1 Absolute proper motion catalog

Due to the high extinction in the visual regime the Gaia mission (Gaia Collaboration et al., 2016) is blind to the GC. However, there are stars in the foreground of the GC whose astrometry has been precisely measured by Gaia and that can be used to link the GNS catalog to the ICRS reference frame (see e.g. Hosek et al., 2022; Libralato et al., 2021b). The Gaia reference frame is aligned with the ICRS with a precision of about ∼0.01 mas, so we considered both reference frames equivalent since this is well below the the absolute astrometric precision of GNS I.

Here we summarize the pipeline we followed for the creation of the proper motion catalog. We show a flowchart of the pipeline in the right panel of Fig. 6.1.2. First, we identified the Gaia stars present in the field of view. We used the stars from the Gaia data release 3 (GDR3 Gaia Collaboration et al., 2023), which presents a significant improvement in astrometric precision compared to GDR2 (Gaia Collaboration et al., 2018), reducing the proper motion uncertainty by a factor of 0.5 (Lindegren et al., 2021). For this preliminary group of stars, we performed a quality cut: i) We avoided Gaia stars with magnitudes brighter than G = 13 to prevent high astrometric uncertainties due to saturation; ii) We discarded Gaia stars with a close Gaia companion to avoid mismatching; iii) We selected only sources with a 5-parameter astrometric solution (position, parallax, and proper motion); and iv) We eliminated Gaia sources with negative parallax, which is unphysical. We refer to the remaining Gaia stars after this quality cut as the reference stars.

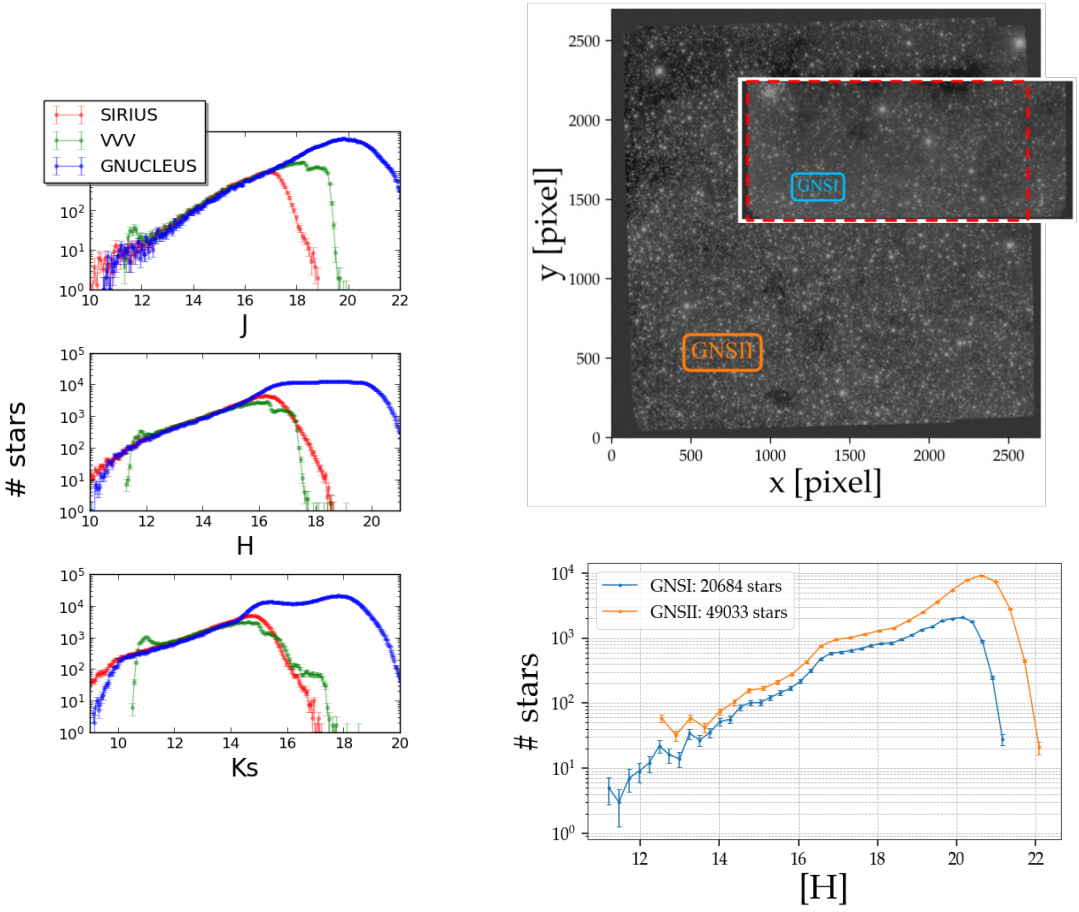

Fig. 6.1.1 Comparison of GNS I with other surveys. Left: Plot and caption from Fig. 12 in Nogueras-Lara et al. (2019a): *Luminosity functions obtained with the SIRIUS survey (in red), the VVV survey (in green), and the GALACTICNUCLEUS survey (in blue). The uncertainties are Poisson errors (square root of the number of stars in each bin).* Right top: Comparison of the effectively used detector area for a single chip, GNS I (blue) and GNS2 (orange). Right bottom: H luminosity functions from on the overlapping area (red-dashed box).

Next, we adjusted the position of the Gaia reference stars to the corresponding epoch of each GNS data set and cross-matched the Gaia stars to their counterparts in the GNS catalogs using the routine `match_to_catalog_sky` from *Astropy* (Astropy Collaboration et al., 2022). We considered two sources separated by less than 80 mas as positive match. We projected the Gaia reference stars to the tangential plane to compare GNS xy coordinates. Then, we applied a first-order transformation (rotation and translation) to move the GNS xy coordinates to the Gaia reference frame. We used the Python module *Astroalign* (Beroiz et al., 2020) to find the transformation matrix. We applied the transformation matrix to the whole GNS list.

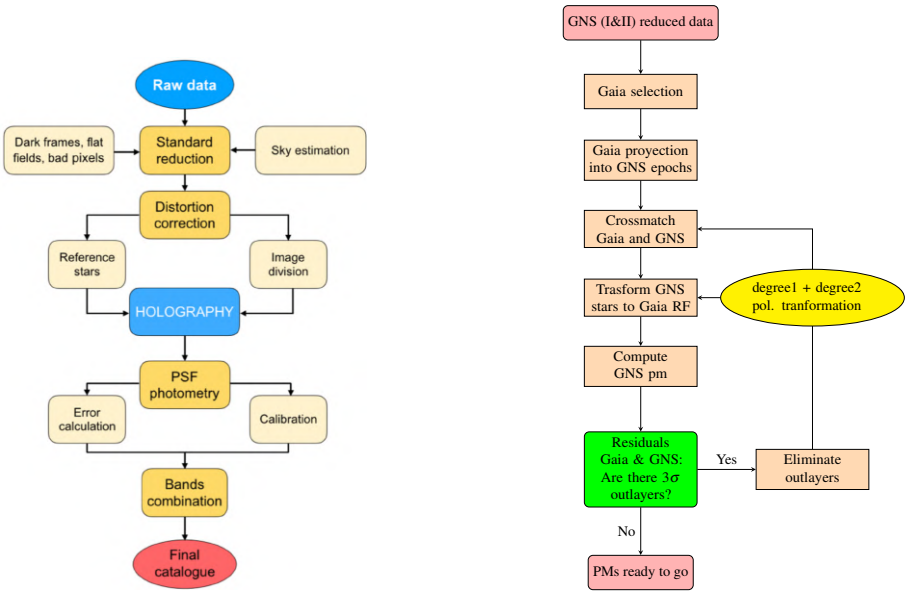

Fig. 6.1.2 Left: Schematic flowchart for the pipeline of the astrophotometric reduction of GNS as it appears in Fig.3 of Nogueras-Lara et al. (2019a). Right: Schematic flowchart for the GNS absolute proper motion pipeline

Once we aligned both data sets, Gaia and GNS, to the Gaia reference frame, we cross-matched the Gaia reference stars again with the two GNS epochs using a dedicated algorithm for cross-matching coordinates lists [1]. Subsequently, we applied a polynomial transform of degree 2 to align the matching reference stars from the two epochs of GNS stars using the IDL module `POLYWARP`. Then, we applied the transformation to the whole list of GNS stars and iterated this process until the number of matching stars remained stable. Next, we computed the proper motion residuals with the Gaia catalog. Reference Gaia stars with residual values $>3\sigma$ were iteratively discarded.

We reduced the data of GNS II and computed proper motions on a test field of GNS II close to the Arches cluster. In the right panel of Fig. 6.1.3, we show the proper motion residuals with respect to Gaia for this test field. The red-dotted lines represent the mean of the RA and Dec residuals, both very close to zero. The blue box indicates the dispersion of the residuals, which is $\sigma = 0.51$ mas/yr.

Hosek et al. (2022) calculated proper motions in the areas around the Arches and Quintuplet clusters (orange squares in Fig. 6.0.1). They used multi-epoch HST WFC3-IR observations from 2010, 2011, 2012, and 2016, with the F153M, F139M, and F127M filters. They linked their catalog to the ICRS using the Gaia Early Data Release 3 (Gaia Collabora-

[1] https://github.com/Almarranz/compare_lists/blob/main/compar_lists.py

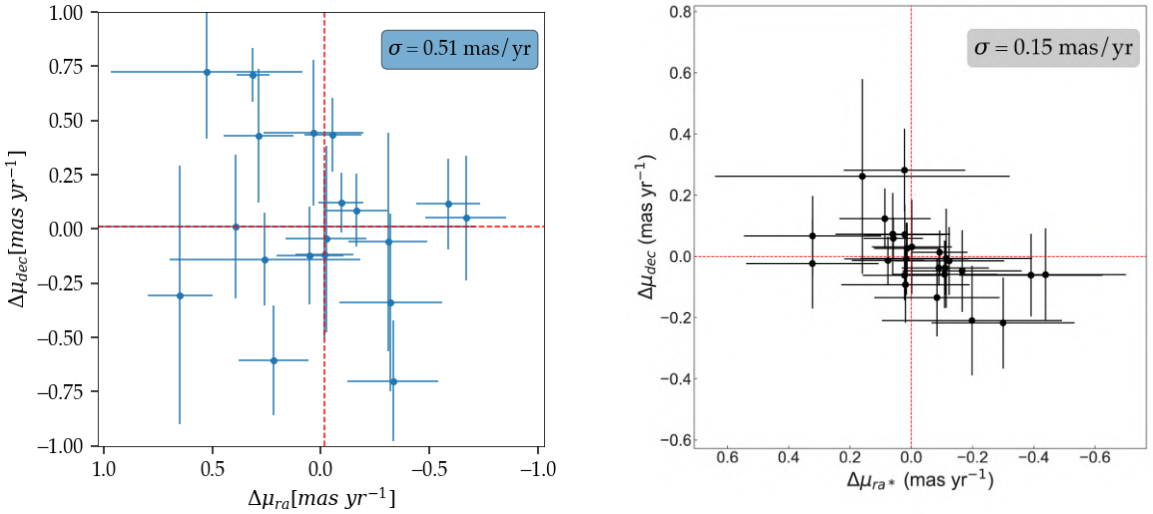

Fig. 6.1.3 Proper motion residuals of Gaia reference stars as measured by using GNS I and II. Red doted lines represent the mean for the residual for the RA and Dec components. Left: Proper motion residuals between GNS and Gaia. Right: Hosek et al. (2022) proper motions residuals in the same field. Credit: Fig.3 in Hosek et al. (2022).

tion et al., 2021). In the right panel of Fig.6.1.3, we show the residuals of their catalog with Gaia. Their residuals exhibited a dispersion of $\sigma = 0.15$ mas/yr.

The higher dispersion of our proper motion residuals with respect to those of Hosek et al. (2022) is fundamentally due to two factors: First, they used four different epochs to compute the proper motions, while we used only two, increasing our uncertainties. Second, they used HST observations, while we used ground-based observations from the VLT. However, this demonstrates that we are able to compute accurate absolute proper motions using ground-based data.

To determine alignment uncertainties for all stars, we used the Jackknife method by systematically removing one Gaia reference star at a time and repeating the alignment procedure 1000 times. We considered the alignment uncertainty as the jackknife standard error (McIntosh, 2016). In Fig. 6.1.4 we show the Gaia referent stars we used for the alignment (left panel) and the corresponding alignment uncertainties (right panel). The strong dependence of the alignment quality on the position and spatial density of the reference stars is noticeable .

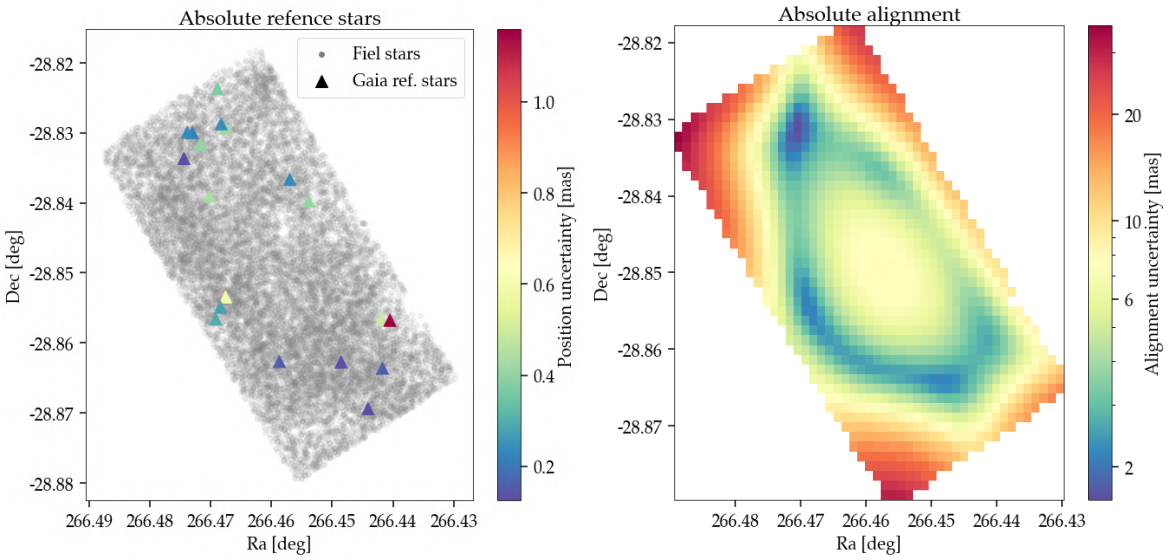

Fig. 6.1.4 Absolute alignment. Left: Astrometric uncertainties of Gaia reference stars. Right: Absolute alignment uncertainty for all stars. Color indicates the mean alignment uncertainty of each bin for all the stars.

6.1.2 Relative proper motion catalog

In this catalog, we adopted the stellar positions in GNS II as the reference frame. We identified common stars between the two epochs using the *Astropy* (Astropy Collaboration et al., 2022) routine `match_to_catalog_sky`. Then, we estimated the rotation and translation between the xy coordinates from both epochs with the Python package *Astroalign* (Beroiz et al., 2020).

Next, we selected the reference stars from the GNS II data set. We applied the following criteria to choose the reference stars: i) Magnitudes had to be $12 < H < 18$ to avoid saturation problems and large uncertainties; ii) The stars had to be isolated within a radius of 0.5" or if they had companions, the companions had to be at least 5 magnitudes dimmer; iii) The statistical relative astrometric uncertainty of the reference stars had to be lower than 0.1 pixel[2]. To obtain a uniform set of reference stars across the field and avoid areas with different densities of reference stars, which would affect the subsequent transformations, we divided the field into cells and applied the quality cut to each one of them, selecting one star per cell. If several stars in a cell met all the selection criteria, the one with the lowest position uncertainty is selected. On the other hand, if none of the stars in a cell met all the criteria, the cell remained empty. In the right panel of Fig. 6.1.5 we show the position of the resulting reference stars of 1800 cells of $\sim 6.5” \times 6.5”$.

[2]The HAWK-I pixel scale is 0.106”/pix

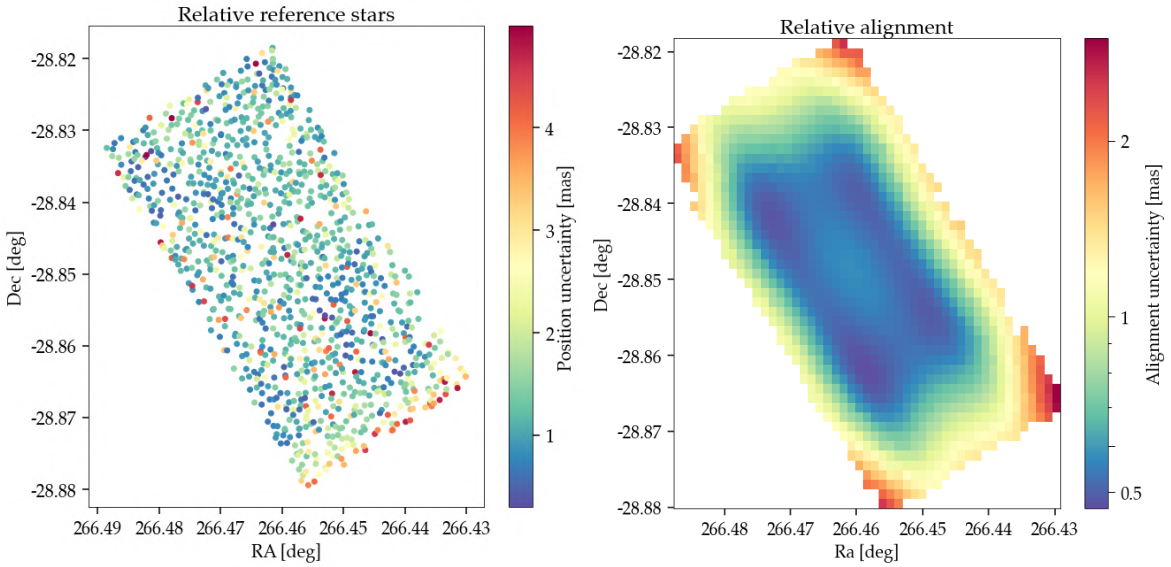

Fig. 6.1.5 Relative alignment. Left: Astrometric uncertainties for the GNS reference stars. Right: Relative alignment uncertainty. Color indicates the mean alignment uncertainty of each bin for all the stars

We cross-matched the reference stars of GNS II with GNS I and applied a polynomial transform of degree 2 to align the positions of the matching stars using the IDL module `POLYWARP`. We tried other degrees for the polynomial transformation but obtained the lowest uncertainties with degree 2. We iteratively repeated the process until the number of matched stars remained stable. Then, we applied the transformation parameters to the whole list of GNS I stars and computed the proper motion dividing the displacement of the stars by the time difference between the two epochs.

We used a bootstrapping method to estimate the uncertainty of the alignment by randomly withdrawing and replacing the set of relative reference stars 1000 times. We used as estimates of the alignment uncertainties the mean and standard deviation of the different outcomes of the Monte Carlo runs. We show in Fig. 6.1.5 the positions of the reference stars (left panel) and the alignment uncertainty (right panel). In contrast to the absolute alignment, the uncertainties here remain constant over a large part of the field of view.

To determine the uncertainties in the proper motion measurements, we applied standard error propagation by taking into account the individual position uncertainties for each star in the directions parallel and perpendicular to the Galactic plane at two epochs. These uncertainties were then added quadratically to the alignment uncertainties. In Fig. 6.1.6 we show the uncertainty for proper motions components parallel (right panel) and perpendicular (left panel) to the Galactic plane. The dashed line indicates the mean proper motion uncertainty. This low uncertainty will allow us to make a conservative quality cut in the proper motion

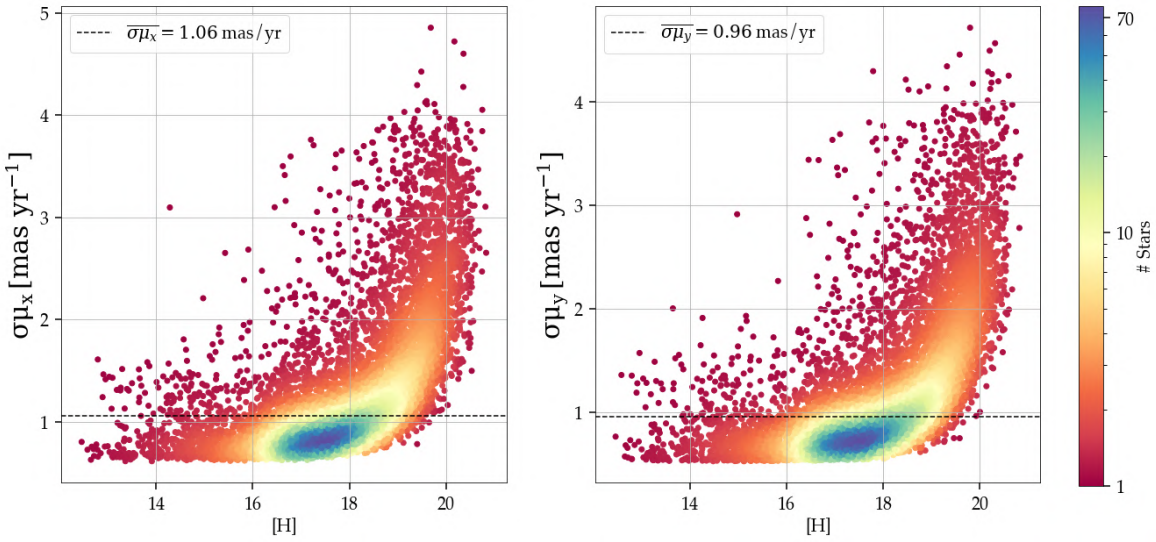

Fig. 6.1.6 Relative proper motion uncertainties. Left: Parallel to the Galactic plane. Right: Perpendicular to the Galactic plane

error of $\sigma\mu < 1$ mas/yr as we did in Martínez-Arranz et al. (2024a) with the catalog of (Libralato et al., 2021a) (see Fig. 4.2) and still retain a significant portion of the data.

6.2 Preliminary results

We followed the procedure described in Sec. 6.1.1 to compute absolute proper motions for the GNS fields covering the Quintuplet cluster. Then, we applied our cluster search algorithm (see Chapter. 4) to the dataset. We successfully identified the Quintuplet cluster, with an average proper motion values of $\mu_{RA} = -0.91 \pm 0.57$ mas/yr and $\mu_{Dec} = -2.77 \pm 0.65$ mas/yr (Fig. 6.2.1). These values are in good agreement with those derived for the Quintuplet by Hosek et al. (2022): $\mu_{RA}^{Hos} = -0.96 \pm 0.13$ mas/yr and $\mu_{Dec}^{Hos} = -2.29 \pm 0.13$ mas/yr. This demonstrates the feasibility of our method, indicating that we can already derive precise proper motions and identify clusters in the GC using ground-based observations.

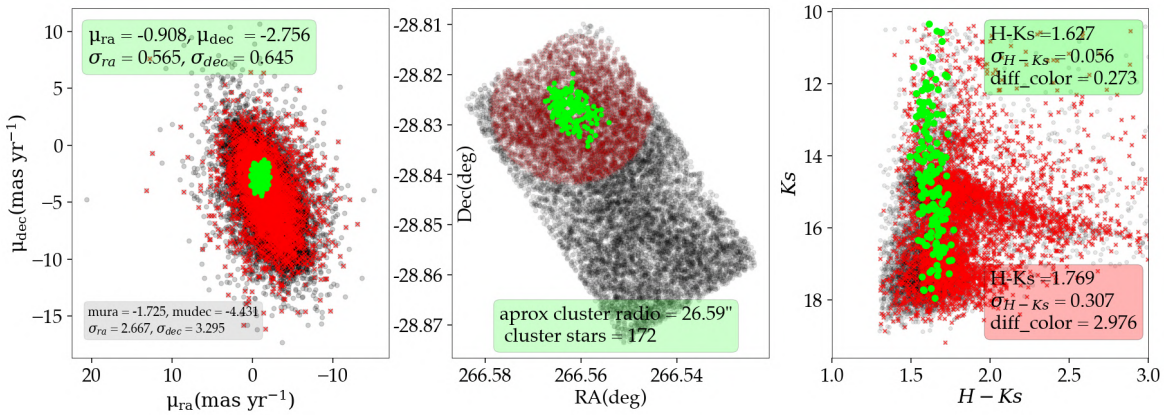

Fig. 6.2.1 Quintuplet cluster extracted from the GNS pm catalog (in progress). Green dots represent the stars selected by the algorithm as cluster members. Red represent the stars around the cluster member that we show for comparison. Black represent the rest of the field stars. Lef: Proper motion vector-point diagram. Center: RA and Dec coordinates. Right: CMD

6.3 Conclusion

The forthcoming GNS proper motion catalog will facilitate a kinematic study of the NSD. While the precise limits and structure of the NSD remain unclear, analyzing the variation of proper motion will shed light on its extension and delineate its boundaries. Furthermore, examining the velocity distribution of the NSD will help confirm the proposed inside-out forming scenario for nuclear rings (Sanders and Binney, 2015; Bittner et al., 2020; Nogueras-Lara et al., 2023). Recently, even the very existence of the NSD has been called into question(Zoccali et al., 2024). The analysis of proper motions in an extended region of the GC will help to clarify the true nature of the NSD. With the new GNS catalog, we will be able to identify the outer edge of the NSD, observe the differential rotation and its lower velocity dispersion compared to that of the Bar, as we see in the nuclear rings of other galaxies (see e.g. Gadotti et al., 2019).

With the GNS catalog we will be able to analyze stellar movements in regions with strong HII emissions, which are indicative of star formation and are prime targets for discovering young stellar clusters. Moreover, the catalog's low uncertainties will allow us to include the proper motions of fainter stars, increasing the likelihood of identifying additional cluster members.

We developed two different methodologies to compute proper motions in the GC: absolute proper motions, anchored to the ICRS using Gaia stars present in the field of view, and relative proper motions, using one of the two epochs as the reference frame. The quality of the proper motions highly depends on the astrometric precision and the spatial distribution of the

reference stars used for the transformations (see Fig. 6.1.4). Although the Gaia reference stars used for the absolute alignment have high astrometric precision, their heterogeneous distribution across the different fields of the GNS pointings makes the relative catalog more suitable for performing large scale kinematic analysis of the NSD. Nonetheless, the absolute catalog has proven useful in relatively small areas with a sufficient density of Gaia reference stars. This will be beneficial for comparing with other catalogs or for studying future young stellar clusters we expect to detect in the GNS catalog, such as the one reported in Martínez-Arranz et al. (2024b), which spans just 20-30 arcseconds on the plane of the sky. We can also align the relative catalog to the ICRS by using the proper motion of Gaia stars.

References

Astropy Collaboration, Adrian M. Price-Whelan, Pey Lian Lim, Nicholas Earl, Nathaniel Starkman, Larry Bradley, David L. Shupe, Aarya A. Patil, Lia Corrales, C. E. Brasseur, and et al. The Astropy Project: Sustaining and Growing a Community-oriented Open-source Project and the Latest Major Release (v5.0) of the Core Package. *ApJ*, 935(2):167, August 2022. doi:10.3847/1538-4357/ac7c74.

Junichi Baba and Daisuke Kawata. Age dating the Galactic bar with the nuclear stellar disc. *MNRAS*, 492(3):4500–4511, March 2020. doi:10.1093/mnras/staa140.

A. T. Barnes, S. N. Longmore, C. Battersby, J. Bally, J. M. D. Kruijssen, J. D. Henshaw, and D. L. Walker. Star formation rates and efficiencies in the Galactic Centre. *MNRAS*, 469 (2):2263–2285, August 2017. doi:10.1093/mnras/stx941.

H. Bartko, F. Martins, S. Trippe, T. K. Fritz, R. Genzel, T. Ott, F. Eisenhauer, S. Gillessen, T. Paumard, T. Alexander, K. Dodds-Eden, O. Gerhard, Y. Levin, L. Mascetti, S. Nayakshin, H. B. Perets, G. Perrin, O. Pfuhl, M. J. Reid, D. Rouan, M. Zilka, and A. Sternberg. An Extremely Top-Heavy Initial Mass Function in the Galactic Center Stellar Disks. *ApJ*, 708(1):834–840, January 2010. doi:10.1088/0004-637X/708/1/834.

M. Beroiz, J. B. Cabral, and B. Sanchez. Astroalign: A Python module for astronomical image registration. *Astronomy and Computing*, 32:100384, July 2020. doi:10.1016/j.ascom.2020.100384.

Adrian Bittner, Patricia Sánchez-Blázquez, Dimitri A. Gadotti, Justus Neumann, Francesca Fragkoudi, Paula Coelho, Adriana de Lorenzo-Cáceres, Jesús Falcón-Barroso, Taehyun Kim, Ryan Leaman, and et al. Inside-out formation of nuclear discs and the absence of old central spheroids in barred galaxies of the TIMER survey. *A&A*, 643:A65, November 2020. doi:10.1051/0004-6361/202038450.

M. Cano-González, R. Schödel, and F. Nogueras-Lara. Detecting hot stars in the Galactic centre with combined near- and mid-infrared photometry. *A&A*, 653:A37, September 2021. doi:10.1051/0004-6361/202140982.

A. Castro-Ginard, C. Jordi, X. Luri, F. Julbe, M. Morvan, L. Balaguer-Núñez, and T. Cantat-Gaudin. A new method for unveiling open clusters in Gaia. New nearby open clusters confirmed by DR2. *A&A*, 618:A59, October 2018. doi:10.1051/0004-6361/201833390.

J. S. Clark, M. E. Lohr, F. Najarro, H. Dong, and F. Martins. The Arches cluster revisited. I. Data presentation and stellar census. *A&A*, 617:A65, September 2018a. doi:10.1051/0004-6361/201832826.

J. S. Clark, M. E. Lohr, L. R. Patrick, F. Najarro, H. Dong, and D. F. Figer. An updated stellar census of the Quintuplet cluster. *A&A*, 618:A2, October 2018b. doi:10.1051/0004-6361/201833041.

J. S. Clark, L. R. Patrick, F. Najarro, C. J. Evans, and M. Lohr. Constraining the population of isolated massive stars within the Central Molecular Zone. *A&A*, 649:A43, May 2021. doi:10.1051/0004-6361/202039205.

J. S. Clark, M. E. Lohr, F. Najarro, L. R. Patrick, and B. W. Ritchie. The Arches cluster revisited - IV. Observational constraints on the binary properties of very massive stars. *MNRAS*, 521(3):4473–4489, May 2023. doi:10.1093/mnras/stad449.

W. I. Clarkson, A. M. Ghez, M. R. Morris, J. R. Lu, A. Stolte, N. McCrady, T. Do, and S. Yelda. Proper Motions of the Arches Cluster with Keck Laser Guide Star Adaptive Optics: The First Kinematic Mass Measurement of the Arches. *ApJ*, 751(2):132, June 2012. doi:10.1088/0004-637X/751/2/132.

S. Comerón, J. H. Knapen, J. E. Beckman, E. Laurikainen, H. Salo, I. Martínez-Valpuesta, and R. J. Buta. AINUR: Atlas of Images of NUclear Rings. *MNRAS*, 402(4):2462–2490, March 2010. doi:10.1111/j.1365-2966.2009.16057.x.

G. Dahmen, S. Huttemeister, T. L. Wilson, and R. Mauersberger. Molecular gas in the Galactic center region. II. Gas mass and N_, = H_2/I_(12)CO conversion based on a C(18)O(J = 1 -> 0) survey. *A&A*, 331:959–976, March 1998. doi:10.48550/arXiv.astro-ph/9711117.

Emiliano Diolaiti, Orazio Bendinelli, Domenico Bonaccini, Laird M. Close, Douglas G. Currie, and Gianluigi Parmeggiani. StarFinder: an IDL GUI-based code to analyze crowded fields with isoplanatic correcting PSF fitting. In Peter L. Wizinowich, editor, *Adaptive Optical Systems Technology*, volume 4007 of *Society of Photo-Optical Instrumentation Engineers (SPIE) Conference Series*, pages 879–888, July 2000. doi:10.1117/12.390377.

H. Dong, Q. D. Wang, A. Cotera, S. Stolovy, M. R. Morris, J. Mauerhan, E. A. Mills, G. Schneider, D. Calzetti, and C. Lang. Hubble Space Telescope Paschen α survey of the Galactic Centre: data reduction and products. *MNRAS*, 417(1):114–135, October 2011. doi:10.1111/j.1365-2966.2011.19013.x.

Hui Dong, Jon Mauerhan, Mark R. Morris, Q. Daniel Wang, and Angela Cotera. Origins of massive field stars in the Galactic Centre: a spectroscopic study. *MNRAS*, 446(1):842–856, January 2015. doi:10.1093/mnras/stu2116.

Hui Dong, John H. Lacy, Rainer Schödel, Francisco Nogueras-Lara, Teresa Gallego-Calvente, Jon Mauerhan, Q. Daniel Wang, Angela Cotera, and Eulalia Gallego-Cano. IRTF/TEXES observations of the H II regions H1 and H2 in the Galactic Centre. *MNRAS*, 470(1): 561–575, May 2017. doi:10.1093/mnras/stx1266.

Bruce G. Elmegreen, Emmanuel Galliano, and Danielle Alloin. Massive Clusters in the Inner Regions of NGC 1365: Cluster Formation and Gas Dynamics in Galactic Bars. *ApJ*, 703 (2):1297–1307, October 2009. doi:10.1088/0004-637X/703/2/1297.

P. Espinoza, F. J. Selman, and J. Melnick. The massive star initial mass function of the Arches cluster. *A&A*, 501(2):563–583, July 2009. doi:10.1051/0004-6361/20078597.

Martin Ester, Hans-Peter Kriegel, Jörg Sander, and Xiaowei Xu. A density-based algorithm for discovering clusters in large spatial databases with noise. In *Proceedings of the Second International Conference on Knowledge Discovery and Data Mining*, KDD'96, pages 226–231. AAAI Press, 1996.

A. Feldmeier-Krause. Stellar populations in the transition region of nuclear star cluster and nuclear stellar disc. *MNRAS*, 513(4):5920–5934, July 2022. doi:10.1093/mnras/stac1227.

K. Ferrière, W. Gillard, and P. Jean. Spatial distribution of interstellar gas in the innermost 3 kpc of our galaxy. *A&A*, 467(2):611–627, May 2007. doi:10.1051/0004-6361:20066992.

Donald F. Figer, Sungsoo S. Kim, Mark Morris, Eugene Serabyn, R. Michael Rich, and Ian S. McLean. Hubble Space Telescope/NICMOS Observations of Massive Stellar Clusters near the Galactic Center. *ApJ*, 525(2):750–758, November 1999a. doi:10.1086/307937.

Donald F. Figer, Ian S. McLean, and Mark Morris. Massive Stars in the Quintuplet Cluster. *ApJ*, 514(1):202–220, March 1999b. doi:10.1086/306931.

Donald F. Figer, R. Michael Rich, Sungsoo S. Kim, Mark Morris, and Eugene Serabyn. An Extended Star Formation History for the Galactic Center from Hubble Space Telescope NICMOS Observations. *ApJ*, 601(1):319–339, January 2004. doi:10.1086/380392.

W. Freudling, M. Romaniello, D. M. Bramich, P. Ballester, V. Forchi, C. E. García-Dabló, S. Moehler, and M. J. Neeser. Automated data reduction workflows for astronomy. The ESO Reflex environment. *A&A*, 559:A96, November 2013. doi:10.1051/0004-6361/201322494.

T. K. Fritz, L. R. Patrick, A. Feldmeier-Krause, R. Schödel, M. Schultheis, O. Gerhard, G. Nandakumar, N. Neumayer, F. Nogueras-Lara, M. A. Prieto, and et al. A KMOS survey of the nuclear disk of the Milky Way. I. Survey design and metallicities. *A&A*, 649:A83, May 2021. doi:10.1051/0004-6361/202040026.

Dimitri A. Gadotti, Patricia Sánchez-Blázquez, Jesús Falcón-Barroso, Bernd Husemann, Marja K. Seidel, Isabel Pérez, Adriana de Lorenzo-Cáceres, Inma Martinez-Valpuesta, Francesca Fragkoudi, Gigi Leung, and et al. Time Inference with MUSE in Extragalactic Rings (TIMER): properties of the survey and high-level data products. *MNRAS*, 482(1): 506–529, January 2019. doi:10.1093/mnras/sty2666.

Dimitri A. Gadotti, Adrian Bittner, Jesús Falcón-Barroso, Jairo Méndez-Abreu, Taehyun Kim, Francesca Fragkoudi, Adriana de Lorenzo-Cáceres, Ryan Leaman, Justus Neumann, Miguel Querejeta, and et al. Kinematic signatures of nuclear discs and bar-driven secular evolution in nearby galaxies of the MUSE TIMER project. *A&A*, 643:A14, November 2020. doi:10.1051/0004-6361/202038448.

Gaia Collaboration, T. Prusti, J. H. J. de Bruijne, A. G. A. Brown, A. Vallenari, C. Babusiaux, C. A. L. Bailer-Jones, U. Bastian, M. Biermann, D. W. Evans, and et al. The Gaia mission. *A&A*, 595:A1, November 2016. doi:10.1051/0004-6361/201629272.

Gaia Collaboration, A. G. A. Brown, A. Vallenari, T. Prusti, J. H. J. de Bruijne, C. Babusiaux, C. A. L. Bailer-Jones, M. Biermann, D. W. Evans, L. Eyer, and et al. Gaia Data Release 2. Summary of the contents and survey properties. *A&A*, 616:A1, August 2018. doi:10.1051/0004-6361/201833051.

Gaia Collaboration, A. G. A. Brown, A. Vallenari, T. Prusti, J. H. J. de Bruijne, C. Babusiaux, M. Biermann, O. L. Creevey, D. W. Evans, L. Eyer, and et al. Gaia Early Data Release 3. Summary of the contents and survey properties. *A&A*, 649:A1, May 2021. doi:10.1051/0004-6361/202039657.

Gaia Collaboration, A. Vallenari, A. G. A. Brown, T. Prusti, J. H. J. de Bruijne, F. Arenou, C. Babusiaux, M. Biermann, O. L. Creevey, C. Ducourant, and et al. Gaia Data Release 3. Summary of the content and survey properties. *A&A*, 674:A1, June 2023. doi:10.1051/0004-6361/202243940.

A. T. Gallego-Calvente, R. Schödel, A. Alberdi, R. Herrero-Illana, F. Najarro, F. Yusef-Zadeh, H. Dong, J. Sanchez-Bermudez, B. Shahzamanian, F. Nogueras-Lara, and et al. Radio observations of massive stars in the Galactic centre: The Arches Cluster. *A&A*, 647:A110, March 2021. doi:10.1051/0004-6361/202039172.

A. T. Gallego-Calvente, R. Schödel, A. Alberdi, F. Najarro, F. Yusef-Zadeh, B. Shahzamanian, and F. Nogueras-Lara. Radio observations of massive stars in the Galactic centre: The Quintuplet cluster. *A&A*, 664:A49, August 2022. doi:10.1051/0004-6361/202141895.

E. Gallego-Cano, R. Schödel, F. Nogueras-Lara, H. Dong, B. Shahzamanian, T. K. Fritz, A. T. Gallego-Calvente, and N. Neumayer. New constraints on the structure of the nuclear stellar cluster of the Milky Way from star counts and MIR imaging. *A&A*, 634:A71, February 2020. doi:10.1051/0004-6361/201935303.

Reinhard Genzel, Frank Eisenhauer, and Stefan Gillessen. The galactic center massive black hole and nuclear star cluster. *Rev. Mod. Phys.*, 82:3121–3195, Dec 2010. doi:10.1103/RevModPhys.82.3121. URL https://link.aps.org/doi/10.1103/RevModPhys.82.3121.

A. M. Ghez, S. Salim, N. N. Weinberg, J. R. Lu, T. Do, J. K. Dunn, K. Matthews, M. R. Morris, S. Yelda, E. E. Becklin, T. Kremenek, M. Milosavljevic, and J. Naiman. Measuring distance and properties of the milky way's central supermassive black hole with stellar orbits. 689 (2):1044–1062, dec 2008. doi:10.1086/592738. URL https://doi.org/10.1086/592738.

Adam Ginsburg and J. M. Diederik Kruijssen. A High Cluster Formation Efficiency in the Sagittarius B2 Complex. *ApJ*, 864(1):L17, September 2018. doi:10.3847/2041-8213/aada89.

Adam Ginsburg, Christian Henkel, Yiping Ao, Denise Riquelme, Jens Kauffmann, Thushara Pillai, Elisabeth A. C. Mills, Miguel A. Requena-Torres, Katharina Immer, Leonardo Testi, and et al. Dense gas in the Galactic central molecular zone is warm and heated by turbulence. *A&A*, 586:A50, February 2016. doi:10.1051/0004-6361/201526100.

Léo Girardi. Red Clump Stars. *ARA&A*, 54:95–133, September 2016. doi:10.1146/annurev-astro-081915-023354.

David Gordon, Aletha de Witt, and Christopher S. Jacobs. Position and Proper Motion of Sagittarius A* in the ICRF3 Frame from VLBI Absolute Astrometry. *AJ*, 165(2):49, February 2023. doi:10.3847/1538-3881/aca65b.

Andrew J. Gosling, Katherine M. Blundell, and Reba Bandyopadhyay. Complex Small-Scale Structure in the Infrared Extinction toward the Galactic Center. *ApJ*, 640(2):L171–L174, April 2006. doi:10.1086/503545.

GRAVITY Collaboration, R. Abuter, A. Amorim, M. Bauböck, J. P. Berger, H. Bonnet, W. Brandner, V. Cardoso, Y. Clénet, P. T. de Zeeuw, J. Dexter, A. Eckart, F. Eisenhauer, N. M. Förster Schreiber, P. Garcia, F. Gao, E. Gendron, R. Genzel, S. Gillessen, M. Habibi, X. Haubois, T. Henning, S. Hippler, M. Horrobin, A. Jiménez-Rosales, L. Jochum, L. Jocou, A. Kaufer, P. Kervella, S. Lacour, V. Lapeyrère, J. B. Le Bouquin, P. Léna, M. Nowak, T. Ott, T. Paumard, K. Perraut, G. Perrin, O. Pfuhl, G. Rodríguez-Coira, J. Shangguan, S. Scheithauer, J. Stadler, O. Straub, C. Straubmeier, E. Sturm, L. J. Tacconi, F. Vincent, S. von Fellenberg, I. Waisberg, F. Widmann, E. Wieprecht, E. Wiezorrek, J. Woillez, S. Yazici, and G. Zins. Detection of the Schwarzschild precession in the orbit of the star S2 near the Galactic centre massive black hole. *A&A*, 636:L5, April 2020. doi:10.1051/0004-6361/202037813.

M. Habibi, S. Gillessen, O. Pfuhl, F. Eisenhauer, P. M. Plewa, S. von Fellenberg, F. Widmann, T. Ott, F. Gao, I. Waisberg, M. Bauböck, A. Jimenez-Rosales, J. Dexter, P. T. de Zeeuw, and R. Genzel. Spectroscopic Detection of a Cusp of Late-type Stars around the Central Black Hole in the Milky Way. *ApJ*, 872(1):L15, February 2019. doi:10.3847/2041-8213/ab03cf.

Maryam Habibi, Andrea Stolte, and Stefan Harfst. Isolated massive stars in the Galactic center: The dynamic contribution from the Arches and Quintuplet star clusters. *A&A*, 566: A6, June 2014. doi:10.1051/0004-6361/201323030.

M. Hankins, R. Lau, M. Morris, A. Cotera, J. Simpson, J. Radomski, E. Mills, D. Walker, A. Barnes, S. Longmore, and et al. SOFIA/FORCAST Galactic Center Legacy Survey: Investigating Warm Dust in the Sagittarius A Complex. In *American Astronomical Society Meeting Abstracts #236*, volume 236 of *American Astronomical Society Meeting Abstracts*, page 332.02, June 2020.

M. J. Hankins, R. M. Lau, E. A. C. Mills, M. R. Morris, and T. L. Herter. SOFIA/FORCAST Observations of the Sgr A-H H II Regions: Using Dust Emission to Elucidate the Heating Sources. *ApJ*, 877(1):22, May 2019. doi:10.3847/1538-4357/ab174e.

M. M. Hanson, R. P. Kudritzki, M. A. Kenworthy, J. Puls, and A. T. Tokunaga. A Medium Resolution Near-Infrared Spectral Atlas of O and Early-B Stars. *ApJSS*, 161(1):154–170, November 2005. doi:10.1086/444363.

S. Harfst, S. Portegies Zwart, and A. Stolte. Reconstructing the Arches cluster - I. Constraining the initial conditions. *MNRAS*, 409(2):628–638, December 2010. doi:10.1111/j.1365-2966.2010.17326.x.

Charles R. Harris, K. Jarrod Millman, Stéfan J. van der Walt, Ralf Gommers, Pauli Virtanen, David Cournapeau, Eric Wieser, Julian Taylor, Sebastian Berg, Nathaniel J. Smith, Robert Kern, Matti Picus, Stephan Hoyer, Marten H. van Kerkwijk, Matthew Brett, Allan Haldane, Jaime Fernández del Río, Mark Wiebe, Pearu Peterson, Pierre Gérard-Marchant, Kevin

Sheppard, Tyler Reddy, Warren Weckesser, Hameer Abbasi, Christoph Gohlke, and Travis E. Oliphant. Array programming with NumPy. *Nature*, 585(7825):357–362, sep 2020. doi:10.1038/s41586-020-2649-2.

T. G. Hawarden, C. M. Mountain, S. K. Leggett, and P. J. Puxley. Enhanced star formation - the importance of bars in spiral galaxies. *MNRAS*, 221:41P–45, August 1986. doi:10.1093/mnras/221.1.41P.

J. D. Henshaw, S. N. Longmore, J. M. D. Kruijssen, B. Davies, J. Bally, A. Barnes, C. Battersby, M. Burton, M. R. Cunningham, J. E. Dale, and et al. Molecular gas kinematics within the central 250 pc of the Milky Way. *MNRAS*, 457(3):2675–2702, April 2016. doi:10.1093/mnras/stw121.

J. D. Henshaw, A. Ginsburg, T. J. Haworth, S. N. Longmore, J. M. D. Kruijssen, E. A. C. Mills, V. Sokolov, D. L. Walker, A. T. Barnes, Y. Contreras, and et al. 'The Brick' is not a brick: a comprehensive study of the structure and dynamics of the central molecular zone cloud G0.253+0.016. *MNRAS*, 485(2):2457–2485, May 2019. doi:10.1093/mnras/stz471.

J. D. Henshaw, A. T. Barnes, C. Battersby, A. Ginsburg, M. C. Sormani, and D. L. Walker. Star Formation in the Central Molecular Zone of the Milky Way. In S. Inutsuka, Y. Aikawa, T. Muto, K. Tomida, and M. Tamura, editors, *Protostars and Planets VII*, volume 534 of *Astronomical Society of the Pacific Conference Series*, page 83, July 2023. doi:10.48550/arXiv.2203.11223.

Jr. Hosek, Matthew W., Jessica R. Lu, Jay Anderson, Andrea M. Ghez, Mark R. Morris, and William I. Clarkson. The Arches Cluster: Extended Structure and Tidal Radius. *ApJ*, 813 (1):27, November 2015. doi:10.1088/0004-637X/813/1/27.

Jr. Hosek, Matthew W., Jessica R. Lu, Jay Anderson, Francisco Najarro, Andrea M. Ghez, Mark R. Morris, William I. Clarkson, and Saundra M. Albers. The Unusual Initial Mass Function of the Arches Cluster. *ApJ*, 870(1):44, January 2019. doi:10.3847/1538-4357/aaef90.

Jr. Hosek, Matthew W., Jessica R. Lu, Casey Y. Lam, Abhimat K. Gautam, Kelly E. Lockhart, Dongwon Kim, and Siyao Jia. SPISEA: A Python-based Simple Stellar Population Synthesis Code for Star Clusters. *AJ*, 160(3):143, September 2020. doi:10.3847/1538-3881/aba533.

Matthew W. Hosek, Tuan Do, Jessica R. Lu, Mark R. Morris, Andrea M. Ghez, Gregory D. Martinez, and Jay Anderson. Measuring the Orbits of the Arches and Quintuplet Clusters Using HST and Gaia: Exploring Scenarios for Star Formation near the Galactic Center. *ApJ*, 939(2):68, November 2022. doi:10.3847/1538-4357/ac8bd6.

Matthew W. Hosek, Tuan Do, Jessica R. Lu, Mark R. Morris, Andrea M. Ghez, Gregory D. Martinez, and Jay Anderson. Measuring the orbits of the arches and quintuplet clusters using hst and gaia: Exploring scenarios for star formation near the galactic center, 2022. URL https://arxiv.org/abs/2208.08508.

B. Hußmann, A. Stolte, W. Brandner, M. Gennaro, and A. Liermann. The present-day mass function of the Quintuplet cluster based on proper motion membership. *A&A*, 540:A57, April 2012. doi:10.1051/0004-6361/201117637.

K. G. Johnston, H. Beuther, H. Linz, A. Schmiedeke, S. E. Ragan, and Th. Henning. The dynamics and star-forming potential of the massive Galactic centre cloud G0.253+0.016. *A&A*, 568:A56, August 2014. doi:10.1051/0004-6361/201423943.

Jens Kauffmann, Thushara Pillai, and Qizhou Zhang. The Galactic Center Cloud G0.253+0.016: A Massive Dense Cloud with low Star Formation Potential. *ApJ*, 765(2): L35, March 2013. doi:10.1088/2041-8205/765/2/L35.

Jr. Kennicutt, Robert C. The Global Schmidt Law in Star-forming Galaxies. *ApJ*, 498(2): 541–552, May 1998. doi:10.1086/305588.

Robert C. Kennicutt, Janice C. Lee, Sanae Akiyama, José G. Funes, and Shoko Sakai. The Demographics of Starburst Galaxies. In Susanne Hüttmeister, Eva Manthey, Dominik Bomans, and Kerstin Weis, editors, *The Evolution of Starbursts*, volume 783 of *American Institute of Physics Conference Series*, pages 3–16. AIP, August 2005. doi:10.1063/1.2034960.

Sungsoo S. Kim, Mark Morris, and Hyung Mok Lee. Evaporation of Compact Young Clusters near the Galactic Center. *ApJ*, 525(1):228–239, November 1999. doi:10.1086/307892.

Woong-Tae Kim, Woo-Young Seo, James M. Stone, Doosoo Yoon, and Peter J. Teuben. Central Regions of Barred Galaxies: Two-dimensional Non-self-gravitating Hydrodynamic Simulations. *ApJ*, 747(1):60, March 2012. doi:10.1088/0004-637X/747/1/60.

J. H. Knapen. Structure and star formation in disk galaxies. III. Nuclear and circumnuclear Hα emission. *A&A*, 429:141–151, January 2005. doi:10.1051/0004-6361:20041909.

J. H. Knapen, J. E. Beckman, C. H. Heller, I. Shlosman, and R. S. de Jong. The Central Region in M100: Observations and Modeling. *ApJ*, 454:623, December 1995. doi:10.1086/176516.

Pavel Kroupa. On the variation of the initial mass function. *MNRAS*, 322(2):231–246, April 2001. doi:10.1046/j.1365-8711.2001.04022.x.

J. M. Diederik Kruijssen and Steven N. Longmore. Comparing molecular gas across cosmic time-scales: the Milky Way as both a typical spiral galaxy and a high-redshift galaxy analogue. *MNRAS*, 435(3):2598–2603, November 2013. doi:10.1093/mnras/stt1634.

J. M. Diederik Kruijssen, Steven N. Longmore, Bruce G. Elmegreen, Norman Murray, John Bally, Leonardo Testi, and Robert C. Kennicutt. What controls star formation in the central 500 pc of the Galaxy? *MNRAS*, 440(4):3370–3391, June 2014. doi:10.1093/mnras/stu494.

J. M. Diederik Kruijssen, James E. Dale, and Steven N. Longmore. The dynamical evolution of molecular clouds near the Galactic Centre - I. Orbital structure and evolutionary timeline. *MNRAS*, 447(2):1059–1079, February 2015. doi:10.1093/mnras/stu2526.

Andrea Kunder, Andreas Koch, R. Michael Rich, Roberto de Propris, Christian D. Howard, Scott A. Stubbs, Christian I. Johnson, Juntai Shen, Yougang Wang, Annie C. Robin, John Kormendy, Mario Soto, Peter Frinchaboy, David B. Reitzel, HongSheng Zhao, and Livia Origlia. THE BULGE RADIAL VELOCITY ASSAY (BRAVA). II. COMPLETE SAMPLE AND DATA RELEASE. *The Astronomical Journal*, 143(3):57, feb 2012. doi:10.1088/0004-6256/143/3/57. URL https://doi.org/10.1088/0004-6256/143/3/57.

Chervin F. P. Laporte, Sergey E. Koposov, and Vasily Belokurov. Kinematics beats dust: unveiling nested substructure in the perturbed outer disc of the Milky Way. *MNRAS*, 510 (1):L13–L17, February 2022. doi:10.1093/mnrasl/slab109.

R. Launhardt, R. Zylka, and P. G. Mezger. The nuclear bulge of the galaxy. 384(1):112–139, mar 2002. doi:10.1051/0004-6361:20020017.

R. Launhardt, R. Zylka, and P. G. Mezger. The nuclear bulge of the Galaxy. III. Large-scale physical characteristics of stars and interstellar matter. *A&A*, 384:112–139, March 2002. doi:10.1051/0004-6361:20020017.

H. R. Ledo, M. Sarzi, M. Dotti, S. Khochfar, and L. Morelli. A census of nuclear stellar discs in early-type galaxies. *MNRAS*, 407(2):969–985, September 2010. doi:10.1111/j.1365-2966.2010.16990.x.

Mattia Libralato, Mark Fardal, Daniel Lennon, Roeland P. van der Marel, and Andrea Bellini. The absolute proper motions of the Arches and Quintuplet clusters. *MNRAS*, 497(4): 4733–4741, October 2020. doi:10.1093/mnras/staa2327.

Mattia Libralato, Daniel J. Lennon, Andrea Bellini, Roeland van der Marel, Simon J. Clark, Francisco Najarro, Lee R. Patrick, Jay Anderson, Luigi R. Bedin, Paul A. Crowther, Selma E. de Mink, Christopher J. Evans, Imants Platais, Elena Sabbi, and Sangmo Tony Sohn. 2D kinematics of massive stars near the Galactic Centre. *MNRAS*, 500(3):3213–3239, January 2021a. doi:10.1093/mnras/staa3329.

Mattia Libralato, Daniel J. Lennon, Andrea Bellini, Roeland van der Marel, Simon J. Clark, Francisco Najarro, Lee R. Patrick, Jay Anderson, Luigi R. Bedin, Paul A. Crowther, Selma E. de Mink, Christopher J. Evans, Imants Platais, Elena Sabbi, and Sangmo Tony Sohn. 2D kinematics of massive stars near the Galactic Centre. *MNRAS*, 500(3):3213–3239, January 2021b. doi:10.1093/mnras/staa3329.

A. Liermann, W. R. Hamann, and L. M. Oskinova. The Quintuplet cluster. III. Hertzsprung-Russell diagram and cluster age. *A&A*, 540:A14, April 2012. doi:10.1051/0004-6361/201117534.

L. Lindegren, S. A. Klioner, J. Hernández, A. Bombrun, M. Ramos-Lerate, H. Steidelmüller, U. Bastian, M. Biermann, A. de Torres, E. Gerlach, and et al. Gaia Early Data Release 3. The astrometric solution. *A&A*, 649:A2, May 2021. doi:10.1051/0004-6361/202039709.

M. Lindqvist, H. J. Habing, and A. Winnberg. OH/IR stars close to the galactic centre. II. Their spatial and kinematics properties and the mass distribution within 5-100 PC from the galactic centre. *A&A*, 259:118–127, June 1992.

D. C. Lis, K. M. Menten, E. Serabyn, and R. Zylka. Star Formation in the Galactic Center Dust Ridge. *ApJ*, 423:L39, March 1994. doi:10.1086/187230.

S. N. Longmore, J. Bally, L. Testi, C. R. Purcell, A. J. Walsh, E. Bressert, M. Pestalozzi, S. Molinari, J. Ott, L. Cortese, and et al. Variations in the Galactic star formation rate and density thresholds for star formation. *MNRAS*, 429(2):987–1000, February 2013a. doi:10.1093/mnras/sts376.

S. N. Longmore, J. M. D. Kruijssen, J. Bally, J. Ott, L. Testi, J. Rathborne, N. Bastian, E. Bressert, S. Molinari, C. Battersby, and et al. Candidate super star cluster progenitor gas clouds possibly triggered by close passage to Sgr a*. *MNRAS*, 433:L15–L19, June 2013b. doi:10.1093/mnrasl/slt048.

S. N. Longmore, J. Bally, L. Testi, C. R. Purcell, A. J. Walsh, E. Bressert, M. Pestalozzi, S. Molinari, J. Ott, L. Cortese, C. Battersby, N. Murray, E. Lee, J. M. D. Kruijssen, E. Schisano, and D. Elia. Variations in the Galactic star formation rate and density thresholds for star formation. *Monthly Notices of the Royal Astronomical Society*, 429 (2):987–1000, 12 2013a. ISSN 0035-8711. doi:10.1093/mnras/sts376. URL https://doi.org/10.1093/mnras/sts376.

S. N. Longmore, A. J. Walsh, C. R. Purcell, D. J. Burke, J. Henshaw, D. Walker, J. Urquhart, A. T. Barnes, M. Whiting, M. G. Burton, and et al. H_2O Southern Galactic Plane Survey (HOPS): Paper III - properties of dense molecular gas across the inner Milky Way. *MNRAS*, 470(2):1462–1490, September 2017. doi:10.1093/mnras/stx1226.

Steven N. Longmore, Jill Rathborne, Nate Bastian, Joao Alves, Joana Ascenso, John Bally, Leonardo Testi, Andy Longmore, Cara Battersby, Eli Bressert, and et al. G0.253 + 0.016: A Molecular Cloud Progenitor of an Arches-like Cluster. *ApJ*, 746(2):117, February 2012. doi:10.1088/0004-637X/746/2/117.

J. R. Lu, T. Do, A. M. Ghez, M. R. Morris, S. Yelda, and K. Matthews. Stellar Populations in the Central 0.5 pc of the Galaxy. II. The Initial Mass Function. *ApJ*, 764(2):155, February 2013. doi:10.1088/0004-637X/764/2/155.

Steven R. Majewski, Ricardo P. Schiavon, Peter M. Frinchaboy, Carlos Allende Prieto, Robert Barkhouser, Dmitry Bizyaev, Basil Blank, Sophia Brunner, Adam Burton, Ricardo Carrera, and et al. The Apache Point Observatory Galactic Evolution Experiment (APOGEE). *AJ*, 154(3):94, September 2017. doi:10.3847/1538-3881/aa784d.

Á. Martínez-Arranz, R. Schödel, F. Nogueras-Lara, and B. Shahzamanian. Distance to the Brick cloud using stellar kinematics. *A&A*, 660:L3, April 2022. doi:10.1051/0004-6361/202243263.

Á. Martínez-Arranz, R. Schödel, F. Nogueras-Lara, M. W. Hosek, and F. Najarro. Co-moving groups around massive stars in the nuclear stellar disk. *A&A*, 683:A3, March 2024a. doi:10.1051/0004-6361/202347937.

A. Martínez-Arranz, R. Schödel, F. Nogueras-Lara, F. Najarro, R. Castellanos, and R. Fedriani. Spectroscopic evidence of a possible young stellar cluster at the Galactic Center. *A&A*, 685:L7, May 2024b. doi:10.1051/0004-6361/202449877.

Noriyuki Matsunaga, Takahiro Kawadu, Shogo Nishiyama, Takahiro Nagayama, Naoto Kobayashi, Motohide Tamura, Giuseppe Bono, Michael W. Feast, and Tetsuya Nagata. Three classical Cepheid variable stars in the nuclear bulge of the Milky Way. *Nat. Astron.*, 477(7363):188–190, September 2011. doi:10.1038/nature10359.

J. C. Mauerhan, A. Cotera, H. Dong, M. R. Morris, Q. D. Wang, S. R. Stolovy, and C. Lang. Isolated Wolf-Rayet Stars and O Supergiants in the Galactic Center Region Identified Via Paschen-α Excess. *ApJ*, 725(1):188–199, December 2010. doi:10.1088/0004-637X/725/1/188.

Avery McIntosh. The Jackknife Estimation Method. *arXiv e-prints*, art. arXiv:1606.00497, June 2016. doi:10.48550/arXiv.1606.00497.

D. H. McNamara, J. B. Madsen, J. Barnes, and B. F. Ericksen. The distance to the galactic center. 112(768):202–216, feb 2000. doi:10.1086/316512. URL https://doi.org/10.1086/316512.

Thomas Melvin, Karen Masters, Chris Lintott, Robert C. Nichol, Brooke Simmons, Steven P. Bamford, Kevin R. V. Casteels, Edmond Cheung, Edward M. Edmondson, Lucy Fortson, and et al. Galaxy Zoo: an independent look at the evolution of the bar fraction over the last eight billion years from HST-COSMOS. *MNRAS*, 438(4):2882–2897, March 2014. doi:10.1093/mnras/stt2397.

E. A. C. Mills, N. Butterfield, D. A. Ludovici, C. C. Lang, J. Ott, M. R. Morris, and S. Schmitz. Abundant CH_3OH Masers but no New Evidence for Star Formation in GCM0.253+0.016. *ApJ*, 805(1):72, May 2015. doi:10.1088/0004-637X/805/1/72.

D. Minniti, P. W. Lucas, J. P. Emerson, R. K. Saito, M. Hempel, P. Pietrukowicz, A. V. Ahumada, M. V. Alonso, J. Alonso-Garcia, J. I. Arias, and et al. VISTA Variables in the Via Lactea (VVV): The public ESO near-IR variability survey of the Milky Way. *NA*, 15 (5):433–443, July 2010. doi:10.1016/j.newast.2009.12.002.

S. Molinari, J. Bally, A. Noriega-Crespo, M. Compiègne, J. P. Bernard, D. Paradis, P. Martin, L. Testi, M. Barlow, T. Moore, and et al. A 100 pc Elliptical and Twisted Ring of Cold and Dense Molecular Clouds Revealed by Herschel Around the Galactic Center. *ApJ*, 735 (2):L33, July 2011. doi:10.1088/2041-8205/735/2/L33.

Esteban F. E. Morales, Friedrich Wyrowski, Frederic Schuller, and Karl M. Menten. Stellar clusters in the inner Galaxy and their correlation with cold dust emission. *A&A*, 560:A76, December 2013. doi:10.1051/0004-6361/201321626.

Mark Morris. Massive Star Formation near the Galactic Center and the Fate of the Stellar Remnants. *ApJ*, 408:496, May 1993. doi:10.1086/172607.

Mark Morris and Eugene Serabyn. The Galactic Center Environment. *ARA&A*, 34:645–702, January 1996. doi:10.1146/annurev.astro.34.1.645.

Francisco Najarro, Donald F. Figer, D. John Hillier, and Rolf P. Kudritzki. Metallicity in the Galactic Center: The Arches Cluster. *ApJ*, 611(2):L105–L108, April 2004. doi:10.1086/423955.

G. Nandakumar, M. Schultheis, A. Feldmeier-Krause, R. Schödel, N. Neumayer, F. Matteucci, N. Ryde, A. Rojas-Arriagada, and A. Tej. Near-infrared spectroscopic observations of massive young stellar object candidates in the central molecular zone. *A&A*, 609:A109, January 2018. doi:10.1051/0004-6361/201731918.

Shogo Nishiyama, Tetsuya Nagata, Nobuhiko Kusakabe, Noriyuki Matsunaga, Takahiro Naoi, Daisuke Kato, Chie Nagashima, Koji Sugitani, Motohide Tamura, Toshihiko Tanabé, and Shuji Sato. Interstellar extinction law in the j, h, and k_s bands toward the galactic center. *ApJ*, 638(2):839–846, February 2006. doi:10.1086/499038. URL https://ui.adsabs.harvard.edu/abs/2006ApJ...638..839N.

Shogo Nishiyama, Tetsuya Nagata, Motohide Tamura, Ryo Kandori, Hirofumi Hatano, Shuji Sato, and Koji Sugitani. The Interstellar Extinction Law toward the Galactic Center. II. V, J, H, and K_s Bands. *ApJ*, 680(2):1174–1179, June 2008. doi:10.1086/587791.

Shogo Nishiyama, Motohide Tamura, Hirofumi Hatano, Daisuke Kato, Toshihiko Tanabé, Koji Sugitani, and Tetsuya Nagata. Interstellar Extinction Law Toward the Galactic Center III: J, H, K_S Bands in the 2MASS and the MKO Systems, and 3.6, 4.5, 5.8, 8.0 μm in the Spitzer/IRAC System. *ApJ*, 696(2):1407–1417, May 2009. doi:10.1088/0004-637X/696/2/1407.

Shogo Nishiyama, Kazuki Yasui, Tetsuya Nagata, Tatsuhito Yoshikawa, Hideki Uchiyama, Rainer Schödel, Hirofumi Hatano, Shuji Sato, Koji Sugitani, Takuya Suenaga, and et al. Magnetically Confined Interstellar Hot Plasma in the Nuclear Bulge of Our Galaxy. *ApJ*, 769(2):L28, June 2013. doi:10.1088/2041-8205/769/2/L28.

Nogueras-Lara, Schödel, R., Neumayer, N., and Schultheis, M. Distance to three molecular clouds in the central molecular zone. *A&A*, 647:L6, Jul 2021a. doi:10.1051/0004-6361/202140554. URL https://doi.org/10.1051/0004-6361/202140554.

F. Nogueras-Lara. A first glimpse at the line-of-sight structure of the Milky Way's nuclear stellar disc. *A&A*, 668:L8, December 2022. doi:10.1051/0004-6361/202244934.

F. Nogueras-Lara, A. T. Gallego-Calvente, H. Dong, E. Gallego-Cano, J. H. V. Girard, M. Hilker, P. T. de Zeeuw, A. Feldmeier-Krause, S. Nishiyama, F. Najarro, N. Neumayer, and R. Schödel. GALACTICNUCLEUS: A high angular resolution JHK_s imaging survey of the Galactic centre. I. Methodology, performance, and near-infrared extinction towards the Galactic centre. *A&A*, 610:A83, March 2018. doi:10.1051/0004-6361/201732002.

F. Nogueras-Lara, R. Schödel, A. T. Gallego-Calvente, H. Dong, E. Gallego-Cano, B. Shahzamanian, J. H. V. Girard, S. Nishiyama, F. Najarro, and N. Neumayer. GALACTICNUCLEUS: A high-angular-resolution JHK_s imaging survey of the Galactic centre. II. First data release of the catalogue and the most detailed CMDs of the GC. *A&A*, 631:A20, November 2019a. doi:10.1051/0004-6361/201936263.

F. Nogueras-Lara, R. Schödel, F. Najarro, A. T. Gallego-Calvente, E. Gallego-Cano, B. Shahzamanian, and N. Neumayer. Variability of the near-infrared extinction curve towards the Galactic centre. *A&A*, 630:L3, October 2019b. doi:10.1051/0004-6361/201936322.

F. Nogueras-Lara, R. Schödel, and N. Neumayer. GALACTICNUCLEUS: A high-angular-resolution JHK_s imaging survey of the Galactic centre. IV. Extinction maps and de-reddened photometry. *A&A*, 653:A133, September 2021a. doi:10.1051/0004-6361/202140996.

F. Nogueras-Lara, R. Schödel, and N. Neumayer. Distance and extinction to the Milky Way spiral arms along the Galactic centre line of sight. *A&A*, 653:A33, September 2021b. doi:10.1051/0004-6361/202040073.

F. Nogueras-Lara, M. Schultheis, F. Najarro, M. C. Sormani, D. A. Gadotti, and R. M. Rich. Evidence of an age gradient along the line of sight in the nuclear stellar disc of the Milky Way. *A&A*, 671:L10, March 2023. doi:10.1051/0004-6361/202345941.

Francisco Nogueras-Lara. Hunting young stars in the Galactic centre. Hundreds of thousands of solar masses of young stars in the Sagittarius C region. *arXiv e-prints*, art. arXiv:2401.07900, January 2024. doi:10.48550/arXiv.2401.07900.

Francisco Nogueras-Lara, Rainer Schödel, Aurelia Teresa Gallego-Calvente, Eulalia Gallego-Cano, Banafsheh Shahzamanian, Hui Dong, Nadine Neumayer, Michael Hilker, Francisco Najarro, Shogo Nishiyama, Anja Feldmeier-Krause, Julien H. V. Girard, and Santi Cassisi. Early formation and recent starburst activity in the nuclear disk of the Milky Way. *Nature Astronomy*, 4:377–381, January 2020. doi:10.1038/s41550-019-0967-9.

Francisco Nogueras-Lara, Rainer Schödel, and Nadine Neumayer. Detection of an excess of young stars in the Galactic Centre Sagittarius B1 region. *Nature Astronomy*, 6:1178–1184, August 2022a. doi:10.1038/s41550-022-01755-3.

Francisco Nogueras-Lara, Rainer Schödel, and Nadine Neumayer. Detection of an excess of young stars in the Galactic Centre Sagittarius B1 region. *Nature Astronomy*, 6:1178–1184, August 2022b. doi:10.1038/s41550-022-01755-3.

J. Paufique, A. Bruton, A. Glindemann, A. Jost, J. Kolb, L. Jochum, M. Le Louarn, M. Kiekebusch, N. Hubin, P. Y. Madec, and et al. GRAAL: a seeing enhancer for the NIR wide-field imager Hawk-I. In Brent L. Ellerbroek, Michael Hart, Norbert Hubin, and Peter L. Wizinowich, editors, *Adaptive Optics Systems II*, volume 7736 of *Society of Photo-Optical Instrumentation Engineers (SPIE) Conference Series*, page 77361P, July 2010. doi:10.1117/12.858261.

T. Paumard, R. Genzel, F. Martins, S. Nayakshin, A. M. Beloborodov, Y. Levin, S. Trippe, F. Eisenhauer, T. Ott, S. Gillessen, R. Abuter, J. Cuadra, T. Alexander, and A. Sternberg. The Two Young Star Disks in the Central Parsec of the Galaxy: Properties, Dynamics, and Formation. *ApJ*, 643(2):1011–1035, June 2006. doi:10.1086/503273.

I. Pérez, I. Martínez-Valpuesta, T. Ruiz-Lara, A. de Lorenzo-Caceres, J. Falcón-Barroso, E. Florido, R. M. González Delgado, M. Lyubenova, R. A. Marino, S. F. Sánchez, and et al. Observational constraints to boxy/peanut bulge formation time. *MNRAS*, 470(1): L122–L126, June 2017. doi:10.1093/mnrasl/slx087.

Simon Portegies Zwart, Jun Makino, Stephen McMillan, and Piet Hut. The lives and deaths of star clusters near the galactic center. *The Astrophysical Journal*, 565, 02 2001. doi:10.1086/324141.

A. B. A. Queiroz, C. Chiappini, A. Perez-Villegas, A. Khalatyan, F. Anders, B. Barbuy, B. X. Santiago, M. Steinmetz, K. Cunha, M. Schultheis, and et al. The Milky Way bar and bulge revealed by APOGEE and Gaia EDR3. *A&A*, 656:A156, December 2021. doi:10.1051/0004-6361/202039030.

J. M. Rathborne, S. N. Longmore, J. M. Jackson, J. F. Alves, J. Bally, N. Bastian, Y. Contreras, J. B. Foster, G. Garay, J. M. D. Kruijssen, and et al. A Cluster in the Making: ALMA Reveals the Initial Conditions for High-mass Cluster Formation. *ApJ*, 802(2):125, April 2015. doi:10.1088/0004-637X/802/2/125.

R. Michael Rich, David B. Reitzel, Christian D. Howard, and HongSheng Zhao. The Bulge Radial Velocity Assay: Techniques and a Rotation Curve. *ApJ*, 658(1):L29–L32, March 2007. doi:10.1086/513509.

Matthew G. L. Ridley, Mattia C. Sormani, Robin G. Treß, John Magorrian, and Ralf S. Klessen. Nuclear spirals in the inner Milky Way. *MNRAS*, 469(2):2251–2262, August 2017. doi:10.1093/mnras/stx944.

Nicholas Z. Rui, Jr. Hosek, Matthew W., Jessica R. Lu, William I. Clarkson, Jay Anderson, Mark R. Morris, and Andrea M. Ghez. The Quintuplet Cluster: Extended Structure and Tidal Radius. *ApJ*, 877(1):37, May 2019. doi:10.3847/1538-4357/ab17e0.

Jörg Sander, Martin Ester, Hans-Peter Kriegel, and Xiaowei Xu. Density-Based Clustering in Spatial Databases: The Algorithm GDBSCAN and Its Applications. *Data Mining and Knowledge Discovery*, 2(2):169, June 1998. doi:10.1023/A:1009745219419.

Jason L. Sanders and James Binney. Extended distribution functions for our Galaxy. *MNRAS*, 449(4):3479–3502, June 2015. doi:10.1093/mnras/stv578.

Maarten Schmidt. The Rate of Star Formation. *ApJ*, 129:243, March 1959. doi:10.1086/146614.

R. Schödel, A. Eckart, T. Alexander, D. Merritt, R. Genzel, A. Sternberg, L. Meyer, F. Kul, J. Moultaka, T. Ott, and et al. The structure of the nuclear stellar cluster of the Milky Way. *A&A*, 469(1):125–146, July 2007. doi:10.1051/0004-6361:20065089.

R. Schödel, F. Najarro, K. Muzic, and A. Eckart. Peering through the veil: near-infrared photometry and extinction for the Galactic nuclear star cluster. Accurate near infrared H, Ks, and L' photometry and the near-infrared extinction-law toward the central parsec of the Galaxy. *A&A*, 511:A18, February 2010. doi:10.1051/0004-6361/200913183.

R. Schödel, S. Yelda, A. Ghez, J. H. Girard, L. Labadie, R. Rebolo, A. Pérez-Garrido, and M. R. Morris. Holographic imaging of crowded fields: high angular resolution imaging with excellent quality at very low cost. *MNRAS*, 429(2):1367–1375, February 2013. doi:10.1093/mnras/sts420.

R. Schödel, A. Feldmeier, D. Kunneriath, S. Stolovy, N. Neumayer, P. Amaro-Seoane, and S. Nishiyama. Surface brightness profile of the milky way's nuclear star cluster. *Astronomy & Astrophysics*, 566:A47, jun 2014. doi:10.1051/0004-6361/201423481.

R. Schödel, E. Gallego-Cano, H. Dong, F. Nogueras-Lara, A. T. Gallego-Calvente, P. Amaro-Seoane, and H. Baumgardt. The distribution of stars around the Milky Way's central black hole. II. Diffuse light from sub-giants and dwarfs. *A&A*, 609:A27, January 2018. doi:10.1051/0004-6361/201730452.

R. Schoedel, A. Feldmeier, D. Kunneriath, S. Stolovy, and N. Neumauer. VizieR Online Data Catalog: Milky Way nuclear star cluster extinction map (Schoedel+, 2014). *VizieR Online Data Catalog*, art. J/A+A/566/A47, March 2014.

Ralph Schonrich, Michael Aumer, and Stuart E. Sale. KINEMATIC DETECTION OF THE GALACTIC NUCLEAR DISK. *The Astrophysical Journal*, 812(2):L21, oct 2015. doi:10.1088/2041-8205/812/2/l21. URL https://doi.org/10.1088/2041-8205/812/2/l21.

Erich Schubert, Jörg Sander, Martin Ester, Hans Peter Kriegel, and Xiaowei Xu. Dbscan revisited, revisited: Why and how you should (still) use dbscan. *ACM Trans. Database Syst.*, 42(3), jul 2017. ISSN 0362-5915. doi:10.1145/3068335. URL https://doi.org/10.1145/3068335.

M. Schultheis, A. Lançon, A. Omont, F. Schuller, and D. K. Ojha. Near-IR spectra of ISOGAL sources in the inner Galactic Bulge. *A&A*, 405:531–550, July 2003. doi:10.1051/0004-6361:20030459.

M. Schultheis, T. K. Fritz, G. Nandakumar, A. Rojas-Arriagada, F. Nogueras-Lara, A. Feldmeier-Krause, O. Gerhard, N. Neumayer, L. R. Patrick, M. A. Prieto, R. Schödel, A. Mastrobuono-Battisti, and M. C. Sormani. The nuclear stellar disc of the Milky Way: A dynamically cool and metal-rich component possibly formed from the central molecular zone. *A&A*, 650:A191, June 2021. doi:10.1051/0004-6361/202140499.

N. Z. Scoville, S. R. Stolovy, M. Rieke, M. Christopher, and F. Yusef-Zadeh. Hubble Space Telescope Paα and 1.9 Micron Imaging of Sagittarius A West. *ApJ*, 594(1):294–311, September 2003. doi:10.1086/376790.

Woo-Young Seo, Woong-Tae Kim, SungWon Kwak, Pei-Ying Hsieh, Cheongho Han, and Phil F. Hopkins. Effects of Gas on Formation and Evolution of Stellar Bars and Nuclear Rings in Disk Galaxies. *ApJ*, 872(1):5, February 2019. doi:10.3847/1538-4357/aafc5f.

B. Shahzamanian, R. Schödel, F. Nogueras-Lara, H. Dong, E. Gallego-Cano, A. T. Gallego-Calvente, and A. Gardini. First results from a large-scale proper motion study of the Galactic centre. *A&A*, 632:A116, December 2019. doi:10.1051/0004-6361/201936579.

B. Shahzamanian, R. Schödel, F. Nogueras-Lara, A. Martínez-Arranz, M. C. Sormani, A. T. Gallego-Calvente, E. Gallego-Cano, and A. Alburai. A proper motion catalogue for the Milky Way's nuclear stellar disc. *A&A*, 662:A11, June 2022. doi:10.1051/0004-6361/202142687.

R. Sharples, R. Bender, A. Agudo Berbel, N. Bezawada, R. Castillo, M. Cirasuolo, G. Davidson, R. Davies, M. Dubbeldam, A. Fairley, G. Finger, N. Förster Schreiber, F. Gonte, A. Hess, I. Jung, I. Lewis, J. L. Lizon, B. Muschielok, L. Pasquini, J. Pirard, D. Popovic, S. Ramsay, P. Rees, J. Richter, M. Riquelme, M. Rodrigues, I. Saviane, J. Schlichter, L. Schmidtobreick, A. Segovia, A. Smette, T. Szeifert, A. van Kesteren, M. Wegner, and E. Wiezorrek. First Light for the KMOS Multi-Object Integral-Field Spectrometer. *The Messenger*, 151:21–23, March 2013.

Kartik Sheth, Stuart N. Vogel, Michael W. Regan, Michele D. Thornley, and Peter J. Teuben. Secular Evolution via Bar-driven Gas Inflow: Results from BIMA SONG. *ApJ*, 632(1): 217–226, October 2005. doi:10.1086/432409.

Rahul Shetty, Christopher N. Beaumont, Michael G. Burton, Brandon C. Kelly, and Ralf S. Klessen. The linewidth-size relationship in the dense interstellar medium of the Central Molecular Zone. *MNRAS*, 425(1):720–729, September 2012. doi:10.1111/j.1365-2966.2012.21588.x.

T. Taro Shimizu, R. I. Davies, D. Lutz, L. Burtscher, M. Lin, D. Baron, R. L. Davies, R. Genzel, E. K. S. Hicks, M. Koss, and et al. The multiphase gas structure and kinematics in the circumnuclear region of NGC 5728. *MNRAS*, 490(4):5860–5887, December 2019. doi:10.1093/mnras/stz2802.

B. D. Simmons, Thomas Melvin, Chris Lintott, Karen L. Masters, Kyle W. Willett, William C. Keel, R. J. Smethurst, Edmond Cheung, Robert C. Nichol, Kevin Schawinski, and et al. Galaxy Zoo: CANDELS barred discs and bar fractions. *MNRAS*, 445(4):3466–3474, December 2014. doi:10.1093/mnras/stu1817.

A. Smette, H. Sana, S. Noll, H. Horst, W. Kausch, S. Kimeswenger, M. Barden, C. Szyszka, A. M. Jones, A. Gallenne, J. Vinther, P. Ballester, and J. Taylor. Molecfit: A general tool for telluric absorption correction. I. Method and application to ESO instruments. *A&A*, 576:A77, April 2015. doi:10.1051/0004-6361/201423932.

Mattia C. Sormani and Ashley T. Barnes. Mass inflow rate into the Central Molecular Zone: observational determination and evidence of episodic accretion. *MNRAS*, 484(1): 1213–1219, March 2019. doi:10.1093/mnras/stz046.

Mattia C. Sormani, Emanuele Sobacchi, Francesca Fragkoudi, Matthew Ridley, Robin G. Treß, Simon C. O. Glover, and Ralf S. Klessen. A dynamical mechanism for the origin of nuclear rings. *MNRAS*, 481(1):2–19, November 2018a. doi:10.1093/mnras/sty2246.

Mattia C. Sormani, Robin G. Treß, Matthew Ridley, Simon C. O. Glover, Ralf S. Klessen, James Binney, John Magorrian, and Rowan Smith. A theoretical explanation for the Central Molecular Zone asymmetry. *MNRAS*, 475(2):2383–2402, April 2018b. doi:10.1093/mnras/stx3258.

Mattia C. Sormani, John Magorrian, Francisco Nogueras-Lara, Nadine Neumayer, Ralph Schönrich, Ralf S. Klessen, and Alessandra Mastrobuono-Battisti. Jeans modelling of the Milky Way's nuclear stellar disc. *MNRAS*, 499(1):7–24, November 2020. doi:10.1093/mnras/staa2785.

Mattia C. Sormani, Jason L. Sanders, Tobias K. Fritz, Leigh C. Smith, Ortwin Gerhard, Rainer Schödel, John Magorrian, Nadine Neumayer, Francisco Nogueras-Lara, Anja Feldmeier-Krause, and et al. Self-consistent modelling of the Milky Way's nuclear stellar disc. *MNRAS*, 512(2):1857–1884, May 2022. doi:10.1093/mnras/stac639.

Mattia C. Sormani, Ashley T. Barnes, Jiayi Sun, Sophia K. Stuber, Eva Schinnerer, Eric Emsellem, Adam K. Leroy, Simon C. O. Glover, Jonathan D. Henshaw, Sharon E. Meidt, and et al. Fuelling the nuclear ring of NGC 1097. *MNRAS*, 523(2):2918–2927, August 2023. doi:10.1093/mnras/stad1554.

Soto, M., Kuijken, K., and Rich, R. M. 3-dimensional kinematics in low foreground extinction windows of the galactic bulge - radial velocities for six bulge fields: procedures and results. *A&A*, 540:A48, 2012. doi:10.1051/0004-6361/201116522. URL https://doi.org/10.1051/0004-6361/201116522.

Joshua S Speagle. dynesty: a dynamic nested sampling package for estimating bayesian posteriors and evidences. 493(3):3132–3158, feb 2020. doi:10.1093/mnras/staa278.

Joshua S. Speagle. DYNESTY: a dynamic nested sampling package for estimating Bayesian posteriors and evidences. *MNRAS*, 493(3):3132–3158, April 2020. doi:10.1093/mnras/staa278.

T. Stolker, S. P. Quanz, K. O. Todorov, J. Kühn, P. Mollière, M. R. Meyer, T. Currie, S. Daemgen, and B. Lavie. MIRACLES: atmospheric characterization of directly imaged planets and substellar companions at 4-5 μm. I. Photometric analysis of β Pic b, HIP 65426 b, PZ Tel B, and HD 206893 B. *A&A*, 635:A182, March 2020. doi:10.1051/0004-6361/201937159.

S. Stolovy, S. Ramirez, R. G. Arendt, A. Cotera, F. Yusef-Zadeh, C. Law, D. Gezari, K. Sellgren, J. Karr, H. Moseley, and H. A. Smith. A mid-infrared survey of the inner 2 × 1.5 degrees of the Galaxy with Spitzer/IRAC. In *Journal of Physics Conference Series*, volume 54 of *Journal of Physics Conference Series*, pages 176–182, December 2006. doi:10.1088/1742-6596/54/1/030.

A. Stolte, A. M. Ghez, M. Morris, J. R. Lu, W. Brandner, and K. Matthews. The Proper Motion of the Arches Cluster with Keck Laser-Guide Star Adaptive Optics. *ApJ*, 675(2): 1278–1292, March 2008. doi:10.1086/527027.

A. Stolte, B. Hußmann, M. R. Morris, A. M. Ghez, W. Brandner, J. R. Lu, W. I. Clarkson, M. Habibi, and K. Matthews. The Orbital Motion of the Quintuplet Cluster—A Common Origin for the Arches and Quintuplet Clusters? *ApJ*, 789(2):115, July 2014. doi:10.1088/0004-637X/789/2/115.

Robin G. Tress, Mattia C. Sormani, Simon C. O. Glover, Ralf S. Klessen, Cara D. Battersby, Paul C. Clark, H. Perry Hatchfield, and Rowan J. Smith. Simulations of the Milky Way's central molecular zone - I. Gas dynamics. *MNRAS*, 499(3):4455–4478, December 2020. doi:10.1093/mnras/staa3120.

E. Valenti, M. Zoccali, O. A. Gonzalez, D. Minniti, J. Alonso-García, E. Marchetti, M. Hempel, A. Renzini, and M. Rejkuba. Stellar density profile and mass of the Milky Way bulge from VVV data. *A&A*, 587:L6, March 2016. doi:10.1051/0004-6361/201527500.

Frank C. van den Bosch, Laura Ferrarese, Walter Jaffe, Holland C. Ford, and Robert W. O'Connell. Hubble Space Telescope Photometry of the Central Regions of Virgo Cluster Elliptical Galaxies. II. Isophote Shapes. *AJ*, 108:1579, November 1994. doi:10.1086/117179.

Pauli Virtanen, Ralf Gommers, Travis E. Oliphant, Matt Haberland, Tyler Reddy, David Cournapeau, Evgeni Burovski, Pearu Peterson, Warren Weckesser, Jonathan Bright, Stéfan J. van der Walt, Matthew Brett, Joshua Wilson, K. Jarrod Millman, Nikolay Mayorov, Andrew R. J. Nelson, Eric Jones, Robert Kern, Eric Larson, C. J. Carey, İlhan Polat, Yu Feng, Eric W. Moore, Jake VanderPlas, Denis Laxalde, Josef Perktold, Robert Cimrman, Ian Henriksen, E. A. Quintero, Charles R. Harris, Anne M. Archibald, Antônio H. Ribeiro, Fabian Pedregosa, Paul van Mulbregt, and SciPy 1. 0 Contributors. SciPy 1.0: fundamental algorithms for scientific computing in Python. *Nature Methods*, 17:261–272, February 2020. doi:10.1038/s41592-019-0686-2.

Q. D. Wang, H. Dong, A. Cotera, S. Stolovy, M. Morris, C. C. Lang, M. P. Muno, G. Schneider, and D. Calzetti. HST/NICMOS Paschen-α Survey of the Galactic Centre: Overview. *MNRAS*, 402(2):895–902, February 2010. doi:10.1111/j.1365-2966.2009.15973.x.

C. Weidner and J. S. Vink. The masses, and the mass discrepancy of O-type stars. *A&A*, 524: A98, December 2010. doi:10.1051/0004-6361/201014491.

M. Zoccali, E. Valenti, F. Surot, O. A. Gonzalez, A. Renzini, and A. Valenzuela Navarro. A new distance to the Brick, the dense molecular cloud G0.253+0.016. *MNRAS*, 502(1): 1246–1252, March 2021. doi:10.1093/mnras/stab089.

M. Zoccali, A. Rojas-Arriagada, E. Valenti, R. Contreras Ramos, A. Valenzuela-Navarro, and C. Salvo-Guajardo. Observed kinematics of the Milky Way nuclear stellar disk region. *A&A*, 684:A214, April 2024. doi:10.1051/0004-6361/202347923.